Sulfide differentiation in slow-spreading ridge magmas

Von der Naturwissenschaftlichen Fakultät der
Gottfried Wilhelm Leibniz Universität Hannover

zur Erlangung des Grades
Doktor der Naturwissenschaften (Dr. rer. nat.)

genehmigte Dissertation
von
Jakub Ciążela, M.Sc.

[2018]

Referent: apl. Prof. Dr. rer. nat. Jürgen Koepke
Koreferent: Prof. zw. dr hab. Andrzej Muszyński

Tag der Promotion: 28.02.2018

ABSTRACT

Slow-spread oceanic crust is thinner and more heterogeneous than fast-spread oceanic crust. These features of the slow-spread oceanic crust affect how sulfides differentiate during magmatic processes and how metals are transported between the mantle and the ocean floor. In order to better understand sulfide differentiation in slow-spreading ridges we investigated igneous rocks from oceanic core complexes (OCC). There, not only volcanic but also plutonic rocks are exposed on the ocean floor. We selected two of the most extensively sampled OCCs to compare between settings with relatively high (Atlantis Bank OCC located at 57°E along the Southwest Indian Ridge) and relatively low (Kane Megamullion OCC located at 23°N along the Mid-Atlantic Ridge) magma supply. Due to high magma supply in Atlantis Bank, large gabbroic bodies can develop and sulfides differentiate mostly through fractional crystallization. Sulfides fractionate early and thus tend to accumulate at the lower part of gabbroic bodies. The lower parts of gabbroic bodies are by ~50% enriched in Cu and by ~100% enriched in S with respect to the upper parts. In addition, gabbro bodies located deeper in the crust are enriched in chalcophile elements with respect to shallower gabbro bodies. Both the facts are consistent with MORBs having sulfur concentrations above sulfide saturation during their ascent through the slow-spread lower crust with high magma supply. In contrast where magma supply is low as is the case for Kane Megamullion, sulfides typically differentiate through melt-mantle reaction. This process may be global, but it becomes increasingly significant at ridge segments with low magma supply and thin crust, where the melt-mantle reaction can proceed to very shallow depths. Melt-mantle reaction leads to high sulfide enrichment at the contacts of gabbro and peridotite. The crust-mantle transition zone exposed in the Kane Megamullion OCC is highly enriched in chalcophile elements. Most seafloor massive sulfides, especially with the highest Cu-grades, occur along slow-spread oceanic lithosphere with relatively low magma supply. The peculiar distribution of the seafloor massive sulfide seems to reflect the style of magmatic differentiation determined by magma supply.

Keywords: Sulfides, chalcophile metals, slow-spreading ridges

ZUSAMMENFASSUNG

Langsam spreizende ozeanische Kruste ist dünner und heterogener als schnell spreizende ozeanische Kruste. Die besonderen Eigenschaften der langsam spreizenden ozeanischen Kruste beeinflussen die Differentiation von Sulfiden während der magmatischen Prozesse sowie den Transport von Metallen vom Mantel zum Meeresboden. Um die Differentiation von Sulfiden in langsam spreizenden Rücken besser zu verstehen, wurden Gesteine der ozeanischen Lithosphäre von ozeanischen Kernkomplexen (OCC) mit verschiedenen petrographischen und analytischen Methoden untersucht. Wir haben zwei von den am meisten beprobten OCCs ausgewählt, um OCCs aus verschiedenen tektonischen Settings zu vergleichen: Die Atlantis Bank (57°E am Südwestindischen Rücken) mit relativ hoher magmatischer Aktivität und den Kane Megamullion (23°N am Mittelatlantischen Rücken) mit relativ geringer magmatischer Aktivität. Aufgrund der hohen magmatischen Förderung in der Atlantis Bank können sich großräumige Gabbro-Intrusionen entwickeln, in denen sich Sulfide meist durch fraktionierte Kristallisation differenzieren können. Sulfide fraktionieren früh und neigen deshalb dazu, sich im basalen Bereich von Gabbro-Intrusionen anzusammeln. So ist der untere Teil von Gabbro-Intrusionen im Vergleich zum oberen Bereich um ~50% Cu und ~100% S angereichert. Darüber hinaus sind individuelle Gabbro-Intrusionen im tieferen Teil der Kruste gegenüber jenen aus der höheren Kruste mit chalkophilen Elementen angereichert. Diese Phänomene entsprechen in jenen MORB Schmelzen (mid-ocean ridge basalts), die sich in langsam spreizender ozeanischer Kruste mit hoher magmatischer Aktivität beim Aufstieg entwickeln, dem Zustand der Übersättigung an Schwefelkonzentration.

Im Gegensatz dazu, differenzieren Sulfide an langsam spreizenden Rückensystem mit geringer magmatischer Aktivität typischerweise durch Reaktionen zwischen Schmelze und Mantelgestein, wie Untersuchungen am Kane Megamullion zeigen. Dieser Prozess hat eine besondere Bedeutung in Rückensegmenten mit dünner Kruste und geringer magmatischer Aktivität, wo die Interaktionen zwischen Schmelze und Mantelgestein bis in sehr geringe Tiefen vorkommen kann. Diese können zu diskreten Sulfid-Anreicherungen im Kontaktbereich zwischen Gabbro und Mantel-Peridotit führen. Die

analytischen Ergebnisse zeigen, dass die Kruste-Mantel Übergangszone vom Kane Megamullion stark durch chalkophile Elemente angereichert ist. Die meisten ozeanischen Massiv-Sulfidlagerstätten, vor allem solche mit den höchsten Cu-Gehalten, treten entlang langsam spreizender ozeanischer Lithosphäre mit relativ niedriger magmatischer Aktivität auf. Diese Häufung reflektiert den besonderen Stil der magmatischen Differentiation in Ridge-Settings mit geringer magmatischer Aktivität.

Schlagwörter: Sulfide, chalkophile Metalle, langsam spreizender Rücken

ACKNOWLEDGEMENTS

I have no doubt this work could never be realized without my supervisors Jürgen Koepke, Andrzej Muszyński, Thomas Kuhn, and my advisor Henry Dick, as well as other co-authors and supportive colleagues listed in the acknowledgement sections of the four included papers. I could repeat all these names at this place but I have chosen not to do so. This place as my heart belongs to my dedicated wife who has been supporting me from the very first line of the first paper until the final paragraph of Conclusions. She believes in me!

TABLE OF CONTENTS

INTRODUCTION

Sulfide ore deposits on land are being depleted due to the high industrial demand for copper, zinc, gold, and other metals. Shrinking on-shore resources have led to exploring the ocean floor (Boschen et al., 2013; Hoagland et al., 2010). The average copper grade of seafloor massive sulfide (SMS) deposits is from 2 to 25 times higher than the average grade of active land-based mines (Hein et al., 2013). The SMS deposits with the highest metal grades occur on top of oceanic core complexes (OCC) (Hannington et al., 2010). OCCs are exposures of the lower crust and mantle moved to the seafloor along detachment faults, which occur along the ultraslow-to-intermediate spreading ridges. The plutonic rocks, as the source for the metals in SMS deposits located on core complexes, are thus crucial to understanding the link between OCCs and metal-rich SMS deposits.

The commonly accepted Penrose model of the oceanic crust (Conference participants, 1972) based on the Oman ophiolite and seismic waves velocities predicts a uniform thickness of the oceanic crust oscillating around 6-7 km. In this model the crystalline part of the oceanic crust is assumed to be well stratified into three main layers: pillow basalts, sheeted dikes and gabbro which overlies the peridotites of the upper mantle. However, the basic research of the last decades showed that this model can only be applied to the fast-spreading ridges. Interestingly, the Penrose model has so far not been proven by a vessel-based research. Instead, many studies on the slow-spreading ridges indicate a general heterogeneity of the oceanic crust (Blackman et al., 2011; Blackman and Collins, 2010; Cannat, 1996; Cannat et al., 1997; Dick et al., 2010, 2008). The strong attenuation of the oceanic crust was observed in many locations, especially in the vicinity of slow-spreading ridges (**Chapter 1**).

Two deep holes had been previously drilled in oceanic core complexes providing possibility to investigate the cycle of sulfur and chalcophile elements in a heterogeneous slow-spread oceanic lower crust. The first hole, 735B, is 1508 m deep (Figure 1). It has also been drilled in the Atlantis Bank OCC located at 57°E along the Southwest Indian Ridge (SWIR) during the IODP expeditions 118 and 176 in 1989 and 1997. Natland et al. (1991) investigated the upper 500 m of the hole (all in gabbro). They found pyrite-pyrrhotite-chalcopyrite aggregates associated with iron-titanium oxides which they interpreted as being formed from iron-rich late-stage melt.

In the longer section, including the rocks from the second expedition, troilite and pentlandite have also been observed. Troilite was interpreted as formed by low-temperature re-equilibration of pyrrhotite (Miller and Cervantes, 2002), an effect that can also explain the presence of pyrite. The Cu and Ni whole-rock concentrations analyzed by Inductively Coupled Plasma-Mass Spectrometry (ICP-MS) are provided by these authors. The Cu concentrations in the lower part of the hole is likely fully controlled by magmatic processes. The Cu and Ni trends are stable and clear in this part of the hole (Miller and Cervantes, 2002) which is typical for fresh rocks. In addition, the major magmatic boundary at a depth of 960 meters below seafloor (mbsf) is clearly visible in the downhole Cu and Ni profiles. In contrast to that, a hydrothermal overprint probably occurred in the upper part of the hole. There, the least altered rocks contain 610 ppm S, whereas the most altered ones contain less than 100 ppm (Alt and Anderson, 1991).

A similar pattern has been observed in the second deep hole, 1415 m-long U1309D, drilled into the Atlantis Massif OCC along Mid-Atlantic Ridge (MAR) in 2004. While high $\delta^{34}S$ signatures (6 to 13‰) in the upper section indicate strong hydrothermal overprint, moderate signatures (-1 to 1‰ in 9 of 10 samples) from the lower part of the hole are in return linked to

magmatic processes (Delacour et al., 2008). Whole-rock and in situ concentrations of chalcophile elements have not been provided.

In the Oman ophiolite, magmatic $\delta^{34}S$ signatures are prevalent not only in the lower part but also in the upper part of the lower crustal section (Oeser et al., 2012). The Oman ophiolite, however, represents a fast-spread ocean crust with a thick carapace of basalts and sheeted dikes on top of the lower crust. Hydrothermal circulation in the lower crust was thus likely less extensive due to the larger depth of the lower crust under the seafloor.

The state of art presented above shows that only sulfur and not chalcophile elements have been fully investigated in the lower oceanic crust. Chalcophile elements have been more extensively studied in the easier accessible upper oceanic crust, for example in two deepest IODP holes drilled into the upper oceanic crust. The deepest IODP hole, 504B at the East Pacific Rise, is a prime example. Here, both sulfur and chalcophile metals have been investigated. The $\delta^{34}S$ values between -2 and +2‰ (Alt et al., 1989) indicating magmatic sulfides correspond to the clear Cu concentration trends in basalts and to some extent also in dikes (Bach et al., 2003). In contrast, high $\delta^{34}S$ values (>+2‰) correspond to the strongly scattered Cu concentrations across the basalt-dike transition zone, indicating a strong hydrothermal activity at that depth level. A similar pattern is shown by Zn and Pb (Bach et al., 2003) and could be expected for other chalcophile elements.

Chalcophile metals have also been studied in the second deepest hole in the fast-spread ocean crust, IODP Hole 1256D in the equatorial Pacific (Alt et al., 2010). Similarly to 504B, Zn and Cu exhibit clear magmatic trends in the basalt section of 1256D. In the dike and gabbro section below, magmatic trends have been overprinted by hydrothermal circulation at high temperatures. Highly altered have lost most of chalcophile metals, and some of them contain

only 7 ppm Cu. However, few relatively fresh gabbro likely representing frozen melts contain igneous sulfides and more than 150 ppm Cu.

Discovery of the heterogeneous and thinner oceanic slow-spreading oceanic crust implies that what was thought about the geochemical cycle of many elements, including Cu and other chalcophile elements, in the ocean lithosphere needs to be revised. For instance, heterogeneous crust implies a more important role of melt-rock reaction with respect to fractional crystallization during magma differentiation (Dick et al., 2010; Lissenberg and Dick, 2008). Hannington et al. (2011) observed that SMSs preferentially occur along the slow-spreading ridges (86%) with respect to intermediate spreading ridges (12%) and fast-spreading ridges (2%). This implies that magmatic processes and lithosphere structure in some way control the SMS formation, and is reflected in the distribution of International Seabed Authority (ISA) sulfide exploration areas. Among seven ISA contractors, China, Russia, France, and Poland operate on ultra-slow and slow-spreading ridge sections with Korea, Germany, and India operating on slow-to-intermediate-spreading ridge sections.

However, the reasons for the peculiar distribution of SMS deposits and the variations in their metal content have been little explored. As a result, the magmatic pre-enrichment processes in the metal source zone needed for the subsequent formation of metal-rich SMS deposits are poorly understood. We are thus still forced to random exploration combing the ocean floor for these deposits, rather than of trying to predict where the highest grade and tonnage SMS deposits are most likely to occur. This thesis makes a first step to remedy this gap. We study how sulfides get pre-enriched due to differentiation processes in slow-spreading ridge magmas. We hypothesize that the style and location of this pre-enrichment are mostly related to the rate of local magma supply.

We collected 232 samples from two sites representing high and low magma supply at slow-spread oceanic lithosphere, which are Atlantis Bank (101 samples) and Kane Megamullion (131 samples) OCCs, respectively. Kane Megamullion OCC is located at 23°N along the MAR. We determined major element, chalcophile element (Cu, Zn, Pb, As, Ga, Tl, Sb, Bi, Au, Ag, Ni, Ge, Se, Te) and S concentrations of all collected samples, as well as S and strontium Sr compositions of selected samples. In addition, we analyzed sulfide and other relevant phases *in situ* for their major and chalcophile element concentrations, and Cu isotopic compositions. The obtained distribution of chalcophile elements and S, along with their isotopes was completed with a thorough petrographic description. Altogether, this allowed us to show two important facts. Firstly, where magma supply is high sulfides differentiate mostly through fractional crystallization. Secondly, where magma supply is low, sulfides differentiate mainly through melt-mantle reaction. These two facts determine the structure of the thesis with its introductory Chapter I followed by Chapter II dedicated to fractional crystallization, and Chapters III and IV dedicated to melt-mantle reaction.

In **Chapter I**, published in *Geologos* (Ciazela et al., 2015), we make a general review of lower crust and mantle exposures at OCCs along mid-ocean ridges. Thirty-two of the thirty-nine OCCs that have been sampled to date contain peridotites. Moreover, peridotites dominate in the plutonic footwall of 77% of OCCs. Massive OCC peridotites come from the very top of the melting column beneath ocean ridges. They are typically spinel harzburgites and show 11.3–18.3% partial melting, generally representing a maximum degree of melting along a segment. Finally, we show that lithosphere structure revealed at OCCs depends on the rate of magma supply, and we highlight an important role of mantle-rock reaction in OCC with low magma

supply. Melt-rock reaction can be traced by the presence of plagioclase is usually linked to impregnation with trapped or transient melt (Dick et al., 2010)

In Chapter II, we study Atlantis Bank OCC characterized by high magma supply. In 2016, International Ocean Discovery Program (IODP) Expedition 360 drilled the 810-m-deep U1473A hole into the gabbroic lower crust of Atlantis Bank (Ciazela et al., 2016; Dick et al., 2016; MacLeod et al., 2017). We selected 101 evenly distributed samples representing the range of rocks in the drill hole to analyze their metal and S contents along with the S and Sr isotopes. Sulfides throughout the hole are almost exclusively pyrrhotite-chalcopyrite-pentlandite grains. This paragenesis along with a consistent trace element composition throughout the hole as well as the mantle-derived S and Sr isotope signatures indicate the predominant role of magmatic processes in the transport of chalcophile metals. Downhole Cu, S, Fe_2O_3, MnO, Co and P_2O_5 upward-decreasing trends matching Mg-number trends and shipboard-defined magmatic units suggest dominant role of fractional crystallization. Sulfide are closely associated with oxides and we observe high correlation coefficients between S, MnO, TiO_2, and Fe_2O_3. As sulfides and oxides fractionate early they tend to accumulate at the lower part of gabbroic bodies, which are by ~50% enriched in Cu and by ~100% enriched in S with respect to the upper parts. This is consistent with MORBs having S concentrations above sulfide saturation during their ascent through the slow-spread lower crust with high magma supply.

In **Chapter III**, published in *Geology* (Ciazela et al., 2017), we suggest that MORBs at slow and ultraslow spreading ridges with lower rates of magma supply can become sulfide-undersaturated due to extensive subcrustal sulfide crystallization following melt reaction with the mantle. This process is significant at ridge segments with a thin crust, where the melt-mantle reaction can proceed to very shallow depths. In addition, conductive cooling related to

hydrothermal circulation and high water content of the serpentinized peridotite boost the intensity of the melt-rock reaction.

In **Chapter IV** published in *Geochimica et Cosmochimica Acta* (Ciazela et al., 2018), we show that the crust-mantle transition zone exposed in the Kane Megamullion OCC are by one order of magnitude enriched in several chalcophile elements with respect to the spinel harzburgites of the mantle beneath. Whereas the range of Cu concentrations in spinel harzburgites is 7-69 ppm, the Cu concentrations are highly elevated in plagioclase harzburgites with a range of 90-209 ppm. The zones of the peridotite-gabbro contacts are even more enriched, exhibiting up to 305 ppm Cu and highly elevated concentrations of As, Zn, Ga, Sb and Tl. High Cu concentrations show pronounced correlation with bulk S concentrations at the crust-mantle transition zone implying an enrichment process in this horizon of the oceanic lithosphere. We interpret this enrichment as related to melt-mantle reaction, which is extensive in crust-mantle transition zones. In spite of the ubiquitous serpentinization of primary rocks, we found magmatic chalcopyrites as inclusions in plagioclase as well as associated with pentlandite and pyrrhotite in polysulfide grains. These chalcopyrites show a primary magmatic δ^{65}Cu signature ranging from -0.04 to +0.29 ‰. Other chalcopyrites have been dissolved during serpentinization. Due to the low temperature (<300 °C) of circulating fluids chalcophile metals from primary sulfides have not been mobilized and transported away but have been trapped in smaller secondary sulfides and hydroxides. Combined with the Cu deposits documented in the crust-mantle transition zones of various ophiolite complexes (Akinci, 2009; Begemann et al., 2010; Panayiotou, 1978; Saalmann and Laine, 2014), our results indicate that the metal enrichment, increased sulfide modes, and potentially formation of small sulfide deposits could be expected globally along the petrological Moho.

References:

Akinci, Ö.T., 2009. Ophiolite-hosted copper and gold deposits of southeastern Turkey: Formation and relationship with seafloor hydrothermal processes. Turkish J. Earth Sci. 18, 475–509. doi:10.3906/yer-0803-8

Alt, J.C., Anderson, T.F., 1991. Mineralogy and Isotopic Composition of Sulfur in Layer 3 Gabbros From the Indian Ocean, Hole 735B. Proc. Ocean Drill. Program, Sci. Results 118, 113–125.

Alt, J.C., Anderson, T.F., Bonnell, L., 1989. The geochemistry of sulfur in a 1.3 km section of hydrothermally altered oceanic crust, DSDP Hole 504B. Geochim. Cosmochim. Acta 53, 1011–1023. doi:10.1016/0016-7037(89)90206-8

Alt, J.C., Laverne, C., Coggon, R.M., Teagle, D.A.H., Banerjee, N.R., Morgan, S., 2010. Subsurface structure of a submarine hydrothermal system in ocean crust formed at the East Pacific Rise, ODP/IODP Site 1256. Geochemistry, Geophys. Geosystems 11, Q10010. doi:10.1029/2010GC003144

Bach, W., Bernhard, P.E., Hart, S.R., Blusztajn, J.S., 2003. Geochemistry of hydrothermally altered oceanic crust: DSDP/ODP Hole 504B - Implications for seawater-crust exchange budgets and Sr- and Pb-isotopic evolution of the mantle. Geochemistry, Geophys. Geosystems 4, 40–55. doi:10.1029/2002GC000419

Begemann, F., Hauptmann, A., Schmitt-Strecker, S., Weisgerber, G., 2010. Lead isotope and chemical signature of copper from Oman and its occurrence in Mesopotamia and sites on the Arabian Gulf coast. Arab. Archaeol. Epigr. 21, 135–169. doi:10.1111/j.1600-0471.2010.00327.x

Blackman, D.K., Collins, J., 2010. Lower crustal variability and the crust/mantle transition at the

Atlantis Massif oceanic core complex. Geophys. Res. Lett. 37, 1–5. doi:10.1029/2010GL045165

Blackman, D.K., Ildefonse, B., John, B.E., Ohara, Y., Miller, D.J., Abe, N., Abratis, M., Andal, E.S., Andreani, M., Awaji, S., Beard, J.S., Brunelli, D., Charney, A.B., Christie, D.M., Collins, J., Delacour, A.G., Delius, H., Drouin, M., Einaudi, F., Escartín, J., Frost, B.R., Früh-Green, G., Fryer, P.B., Gee, J.S., Godard, M., Grimes, C.B., Halfpenny, A., Hansen, H.-E., Harris, A.C., Tamura, A., Hayman, N.W., Hellebrand, E., Hirose, T., Hirth, J.G., Ishimaru, S., Johnson, K.T.M., Karner, G.D., Linek, M., MacLeod, C.J., Maeda, J., Mason, O.U., McCaig, A.M., Michibayashi, K., Morris, A., Nakagawa, T., Nozaka, T., Rosner, M., Searle, R.C., Suhr, G., Tominaga, M., von der Handt, A., Yamasaki, T., Zhao, X., 2011. Drilling constraints on lithospheric accretion and evolution at Atlantis Massif, Mid-Atlantic Ridge 30°N. J. Geophys. Res. 116, B07103. doi:10.1029/2010JB007931

Boschen, R.E., Rowden, A.A., Clark, M.R., Gardner, J.P.A., 2013. Mining of deep-sea seafloor massive sulfides: A review of the deposits, their benthic communities, impacts from mining, regulatory frameworks and management strategies. Ocean Coast. Manag. 84, 54–67. doi:10.1016/j.ocecoaman.2013.07.005

Cannat, M., 1996. How thick is the magmatic crust at slow spreading oceanic ridges? J. Geophys. Res. 101, 2847–2857.

Cannat, M., Lagabrielle, Y., Bougault, H., Casey, J., de Coutures, N., Dmitriev, L., Fouquet, Y., 1997. Ultramafic and gabbroic exposures at the Mid-Atlantic Ridge: geological mapping in the 15°N region. Tectonophysics 279, 193–213. doi:10.1016/S0040-1951(97)00113-3

Ciazela, J., Dick, H.J.B., Koepke, J., Pieterek, B., Muszynski, A., Botcharnikov, R., Kuhn, T., 2017. Thin crust and exposed mantle control sulfide differentiation in slow-spreading ridge

magmas. Geology 45, 935–938. doi:10.1130/G39287.1

Ciazela, J., Dick, H.J.B., MacLeod, C.J., Blum, P., the Expedition 360 Scientists, 2016. IODP Expedition 360: first stage of drilling into Earth's Mantle. Przegląd Geol. 64, 889–895.

Ciazela, J., Koepke, J., Dick, H.J.B., Muszynski, A., 2015. Mantle rock exposures at oceanic core complexes along mid-ocean ridges. Geologos 4, 207–231. doi:10.1515/logos-20315-0017

Ciazela, J., Koepke, J., Henry, J.B.D., Botcharnikov, R.E., Muszynski, A., Lazarov, M., Schuth, S., Pieterek, B., Kuhn, T., 2018. Sulfide enrichment at an oceanic crust-mantle transition zone: Kane Megamullion (23°N, MAR). Geochim. Cosmochim. Acta. doi:https://doi.org/10.1016/j.gca.2018.03.027

Conference participants, 1972. Penrose field conference on ophiolites. Geotimes 17, 24–25.

Delacour, A., Früh-Green, G.L., Bernasconi, S.M., 2008. Sulfur mineralogy and geochemistry of serpentinites and gabbros of the Atlantis Massif (IODP Site U1309). Geochim. Cosmochim. Acta 72, 5111–5127. doi:10.1016/j.gca.2008.07.018

Dick, H.J.B., Johan Lissenberg, C., Warren, J.M., 2010. Mantle melting, melt transport, and delivery beneath a slow-spreading ridge: The paleo-MAR from 23??15???N to 23??45???N. J. Petrol. 51, 425–467. doi:10.1093/petrology/egp088

Dick, H.J.B., Macleod, C.J., Blum, P., the Expedition 360 Scientists, 2016. Expedition 360 Preliminary report: Southwest Indian Ridge lower crust and Moho. International Ocean Discovery Program.

Dick, H.J.B., Tivey, M., Tucholke, B.E., 2008. Plutonic foundation of a slow-spreading ridge segment: Oceanic core complex at Kane Megamullion, 23°30′N, 45°20′W. Geochemistry Geophys. Geosystems 9, Q05014. doi:10.1029/2007GC001645

Hannington, M., Jamieson, J., Monecke, T., Petersen, S., 2010. Sea-Floor Massive Sulfides and Base Metal Resources: Toward an Estimate of Global Sea-Floor Massive Sulfide Potential. Soc. Econ. Geol. Inc. 317–338.

Hannington, M., Jamieson, J., Monecke, T., Petersen, S., Beaulieu, S., 2011. The abundance of seafloor massive sulfide deposits. Geology 39, 1155–1158. doi:10.1130/G32468.1

Hein, J.R., Mizell, K., Koschinsky, A., Conrad, T., 2013. Deep-ocean mineral deposits as a source of critical metals for high- and green-technology applications: Comparison with land-based resources. Ore Geol. Rev. 51, 1–14. doi:10.1016/j.oregeorev.2012.12.001

Hoagland, P., Beaulieu, S., Tivey, M.A., Eggert, R.G., German, C., Glowka, L., Lin, J., 2010. Deep-sea mining of seafloor massive sulfides. Mar. Policy 34, 728–732. doi:10.1016/j.marpol.2009.12.001

Lissenberg, C.J., Dick, H.J.B., 2008. Melt-rock reaction in the lower oceanic crust and its implications for the genesis of mid-ocean ridge basalt. Earth Planet. Sci. Lett. 271, 311–325. doi:10.1016/j.epsl.2008.04.023

MacLeod, C.J., Dick, H.J.B., Blum, P., the Expedition 360 Scientists, 2017. Soutwest Indian Ridge Lower Crust and Moho. Proc. Int. Ocean Discov. Progr. 360.

Miller, J., Cervantes, P., 2002. Sulfide mineral chemistry and petrography and platinum group element composition in gabbroic rocks from the Southwest Indian Ridge, in: Proceedings of the Ocean Drilling Program, Scientific Results. pp. 1–29.

Natland, J.H., Meyer, P.S., Dick, H.J.B., Bloomer, S.H., 1991. Magmatic oxides and sulfides in gabbroic rocks from Hole 735B and the later development of the liquid line of descent. Proc. Ocean Drill. Program, Sci. Results 118, 75–111.

Oeser, M., Strauss, H., Wolff, P.E., Koepke, J., Peters, M., Garbe-Schönberg, D., Dietrich, M.,

2012. A profile of multiple sulfur isotopes through the Oman ophiolite. Chem. Geol. 312–313, 27–46. doi:10.1016/j.chemgeo.2012.04.008

Panayiotou, A., 1978. The mineralogy and chemistry of the podiform chromite deposits in the serpentinites of the Limassol Forest, Cyprus. Miner. Depos. 13, 259–274. doi:10.1007/BF00204647

Saalmann, K., Laine, E.L., 2014. Structure of the Outokumpu ore district and ophiolite-hosted Cu-Co-Zn-Ni-Ag-Au sulfide deposits revealed from 3D modeling and 2D high-resolution seismic reflection data. Ore Geol. Rev. 62, 156–180. doi:10.1016/j.oregeorev.2014.03.003

Geologos 21, 4 (2015): 207–231
doi: 10.1515/logos-2015-0017

GEOLOGOS

Mantle rock exposures at oceanic core complexes along mid-ocean ridges

Jakub Ciazela[1,2*], Juergen Koepke[2], Henry J.B. Dick[3] & Andrzej Muszynski[1]

[1]Institute of Geology, Adam Mickiewicz University, Institute of Geology, Maków polnych 16, 61-606 Poznań, Poland
[2]Institut für Mineralogie, Leibniz Universität Hannover, Callinstrasse 3, 30167 Hannover, Germany
[3]Department of Geology and Geophysics, Woods Hole Oceanographic Institution, MS #8, McLean Laboratory, Woods Hole MA 02543-1539, USA
[*] corresponding author, e-mail: ciazela@amu.edu.pl

Abstract

The mantle is the most voluminous part of the Earth. However, mantle petrologists usually have to rely on indirect geophysical methods or on material found ex situ. In this review paper, we point out the in-situ existence of oceanic core complexes (OCCs), which provide large exposures of mantle and lower crustal rocks on the seafloor on detachment fault footwalls at slow-spreading ridges. OCCs are a common structure in oceanic crust architecture of slow-spreading ridges. At least 172 OCCs have been identified so far and we can expect to discover hundreds of new OCCs as more detailed mapping takes place. Thirty-two of the thirty-nine OCCs that have been sampled to date contain peridotites. Moreover, peridotites dominate in the plutonic footwall of 77% of OCCs. Massive OCC peridotites come from the very top of the melting column beneath ocean ridges. They are typically spinel harzburgites and show 11.3–18.3% partial melting, generally representing a maximum degree of melting along a segment. Another key feature is the lower frequency of plagioclase-bearing peridotites in the mantle rocks and the lower abundance of plagioclase in the plagioclase-bearing peridotites in comparison to transform peridotites. The presence of plagioclase is usually linked to impregnation with late-stage melt. Based on the above, OCC peridotites away from segment ends and transforms can be treated as a new class of abyssal peridotites that differ from transform peridotites by a higher degree of partial melting and lower interaction with subsequent transient melt.

Keywords: peridotite, OCC, detachment fault, megamullion, slow-spreading ridge

1. Introduction

The mantle is the most voluminous part of the Earth. Assuming that the Earth's core has a radius of 3,482 km (Dziewonski & Anderson, 1981) and that the average depth to the Moho is 26.4 km (Bagherbandi et al., 2013). It can be concluded that the mantle constitutes 82.4% of the volume of the Earth. Therefore, it is crucial to understand its structure, heterogeneities and bulk composition, in order to infer the composition of the bulk Earth. The composition of the mantle, compared to that of the bulk Earth, can be used to estimate the composition of the Earth's core (Carlson, 2003). Moreover, the mantle plays an important role in our understanding of the mechanisms of plate tectonics (Morris & Ryan, 2003) and the accretion of oceanic and continental crust (e.g., Kelemen et al., 1997; Martinez & Taylor, 2002). Another important aspect is related to the giant mass of water that is contained in the mantle. There are 1.5×10^{24} g of water on the Earth's surface (mainly oceans), which corresponds to 250 ppm of the Earth's bulk composition. At least half of that is thought to be found in the mantle, which is the main deep water reservoir in the Earth system. Some researchers estimate that the mantle might contain even 10 times the quantity of water in the ocean (Marty &Yokochi, 2006). Finally, the

mantle might be an important reservoir of hydrocarbons (Scott et al., 2004), as suspected already by Gold (1999) in his controversial book *The deep hot biosphere*. In fact, the biosphere may exist in suboceanic mantle according to the newest research (Menez et al., 2012; McCollom & Seewald, 2013).

For all these reasons, the great interest in the composition of the Earth's mantle is not surprising. In the present paper, we review the commonest sources of our knowledge of the mantle (Section 2) and provide a new data set for abyssal mantle rocks that is available due to the discovery of oceanic core complexes (OCCs). We describe the typical tectonic settings of OCCs (Section 3), the general mechanism of their emplacement and classify them according to spreading rate and magma flux (Section 4). Subsequently, we list all OCCs discovered so far (Section 5) and focus on those that contain greater amounts of mantle rocks (Section 6). Finally, we discuss their origin and petrological aspects and conclude that they exhibit special characteristics that potentially distinguish them from abyssal peridotites formed in other geotectonic settings.

2. Traditional sources of our knowledge of the mantle

The deepest Earth samples recovered so far are preserved in diamonds; they are possibly derived from the top of the lower mantle. However, although they came from the ultra-deep mantle, they probably represent an anomalous composition, due to the special conditions related to diamond formation. Mantle rocks delivered to the Earth's surface as xenoliths in basaltic magmas are quite common. However, these are also limited in size and do not provide information on field relations. Furthermore, they are often influenced by the infiltrating host magma. Nevertheless, they do represent almost the whole upper mantle, since some xenoliths found in kimberlites come from a depth of 500 km near the transition zone between the upper and lower mantle (Pearson et al., 2003).

Only the uppermost mantle is represented by orogenic, ophiolitic and abyssal peridotites. All three types are often strongly altered. However, those that are sufficiently well preserved, reveal unique information about the structural relationship between different lithologies, the melt extraction from the mantle source, melt flow in lithospheric vein conduits (Bodinier & Godard, 2003) and the mantle flow beneath a ridge (Jousselin et al., 1998). Abyssal peridotites yield the most complete information about the mantle below the oceanic crust, which is sparsely sampled by xenoliths. Most occurrences of abyssal peridotites are found at mid-ocean ridges. The few other locations where they have been recognised include passive margins and supra-subduction zones (Bodinier & Godard, 2003; Parkinson & Pearce, 1998), with the most intensely investigated ones situated in the Parece Vela Basin (Ohara et al., 2003b).

3. Slow-spreading ridges as a suitable tectonic setting for OCC

There is far more potential for mantle rocks to be exposed at slow-spreading ridges compared to fast-spreading ones. In a review paper, Bodinier & Godard (2003) listed only three such localities at fast-spreading ridges: at Hess deep and at Garret and Terevaka Fracture Zones to the south of Hess deep. The scarcity of peridotites at fast-spreading ridges results from the relatively high crustal thickness along fast-spreading ridges (~7 km; White et al., 1992; Canales et al., 1998, 2003) and the regular sequence of basaltic carapace (1–2 km), sheeted dykes (1–2 km) and gabbros (3–5 km) (Klein, 2003); see Fig. 1A. It was believed for a long time that this model of the crust was also valid for slow-spreading ridges, as was proposed by Penrose Conference Participants (1972). However, when we observe the topography of the two kinds of ridges, we notice that the surface of the fast-spreading ridge area is usually smooth compared to slow-spreading ridges, with no median valley, while the surface of the slow-spreading ridges area is rugged with kilometre-scale relief and a deep 1–2 km median valley at the spreading axis (Wilson, 1997). This discrepancy is related to the lower and more episodic flux of magma and thicker lithosphere in slow-spreading ridges (Macdonald et al., 1993). The latter results in considerable heterogeneity of the crust (Dick et al., 2006). Dick (1989) reported a decrease of crustal thickness with distance from the segment centre at slow-spreading ridges (Fig. 1B). Cannat (1996) proposed a model of a very heterogeneous crust similar to a "plum-pudding", in which gabbro bodies are dispersed in peridotite mantle (Fig. 1C), which contrasts strongly with the model of a homogeneous, layered crust from fast-spreading ridges. Gabbro bodies predominate during high magma flux periods, and peridotites do so in magma starvation periods (see Coogan, 2013 for details). Based on the ratio of mafic rocks to mantle rock, which can be interpreted as a proxy for magma flux, Dick

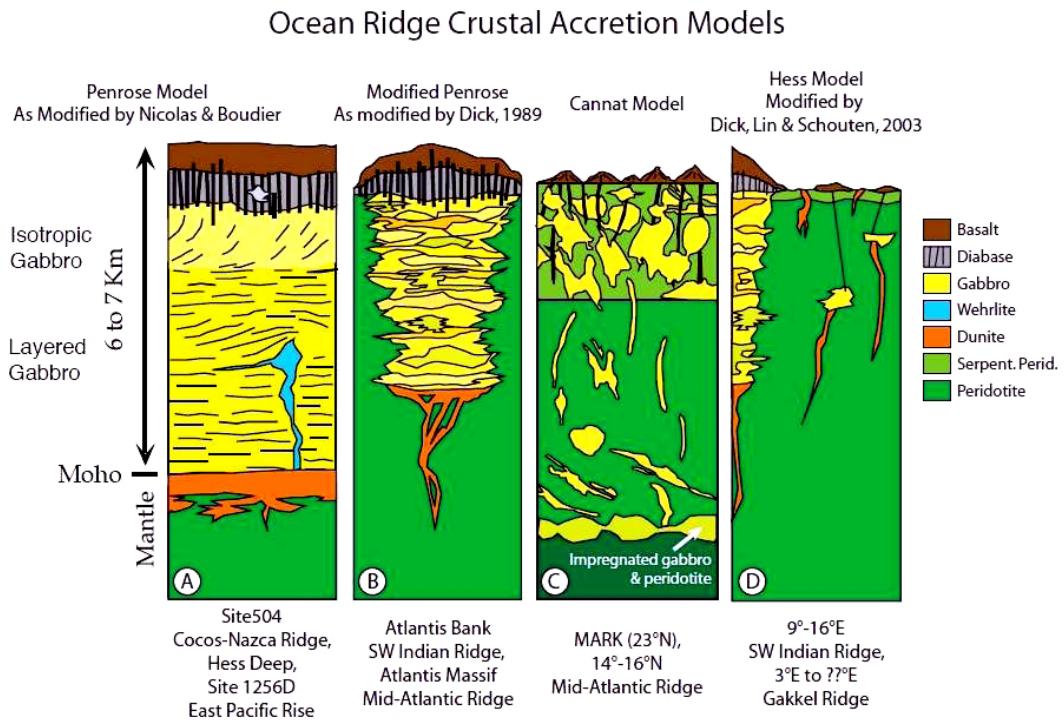

Fig. 1. Models for crustal accretion at ocean ridges. **A –** Classic interpretation of the Penrose Model for a fast-spreading ridge, as based on the Oman Ophiolite; **B –** Penrose model, as modified for slow-spreading ridges based on the abundance of peridotite and frequent absence of gabbro at transforms following focused melt-flow models; **C –** Model of the anomalous 14–16°N area of the Mid-Atlantic Ridge; **D –** Model of the magmatic and amagmatic accretionary segments at ultraslow-spreading ridges (after Dick et al., 2006)

et al. (2003) presented general models for the variety of structural types observed at slow-spreading ridges. As a new type, these authors defined ultraslow-spreading ridges (e.g., Gakkel Ridge, Southwest Indian Ridge (SWIR)), which are characterised by very low magma flux. Here, the scarcity of gabbro bodies in some regions results in the absolute predominance of peridotites just below a thin, irregular basaltic carapace and sedimentary cover (Fig. 1D).

For a long time, abyssal peridotites were recovered only at deep axial valleys, transform faults and fracture zones, where lower crustal and mantle rocks are tectonically exposed on their walls

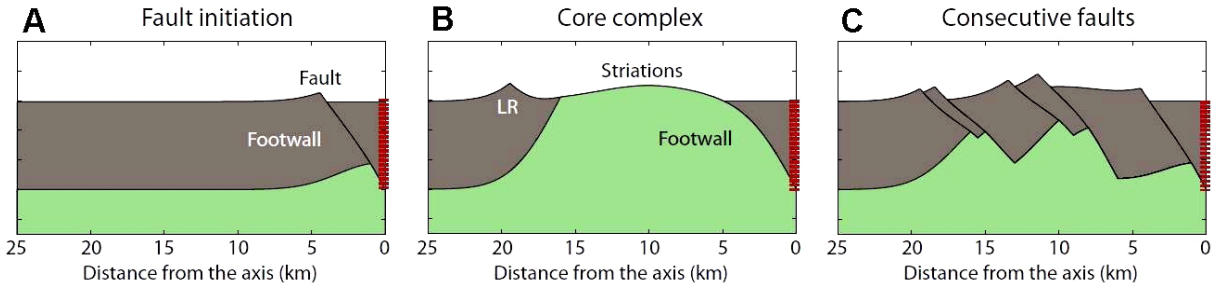

Fig. 2. Two styles of faulting at a slow-spreading ridge. Faults are indicated as subsurface black lines, and the footwall is marked. A normal fault forms, dipping at 60° beneath the axis. **A –** In this panel, fault offset is 1 km, and the fault block has rotated outwardly away from the ridge axis by 18° to form an outward-facing scarp; **B –** Continued faulting and extension brings lower crustal rocks to the sea floor and forms a "core complex". In this panel, the fault offset is 16 km, and outward rotation of the top of the fault has increased to 36° to create a narrow linear ridge (LR) marking the breakaway where the fault initially formed. The exposed footwall may be striated; **C –** In this panel, no long-lived faults have formed. Instead, consecutive short-lived faults cut the lithosphere on the ridge flank to form classic abyssal hill topography.

Red dashed line – spreading axis. Brown shading – crust that predates faulting. Green shading – material below the crust that is brought to the surface during core-complex formation (after Smith et al., 2012).

(Dick, 1989; Cannat et al., 1993). These outcrops are usually limited to a narrow linear zone along the walls. Although larger two-dimensional exposures of mantle and plutonic rocks were first discovered exposed by detachment faulting at ridge-transform intersections over 30 years ago (Dick et al., 1981), the majority of the geological community thought such exposures were anomalies. This changed in the mid-1990s when detachment faults were widely documented along the Mid-Atlantic Ridge (e.g., Tucholke & Lin, 1994; Tucholke et al. 1996; Cann et al., 1997). The lower parts of detachment fault footwalls represent continuous exposure of lower crust and mantle rocks on a single fault for up to millions of years and are called oceanic core complexes (OCC), due to an analogy with land core complexes that similarly exposed lower crustal rocks (Smith et al., 2012).

4. Mechanism of emplacement, features and classification of oceanic core complexes

It was believed for a long time that oceanic crust at slow-spreading ridges accreted symmetrically (e.g., Skinner et al., 2004), and that the divergent transport of the adjacent tectonic plates was mostly accommodated by the delivery of new magma (Solomon et al., 1988). In this model, periods of magma starvation are short and accommodated by short-lived, high-angle normal faults (see Fig. 2C; Thatcher & Hill, 1995; Smith et al., 2012). However, the numerous core complexes discovered on slow-spreading ridges have led to an alternative asymmetric spreading model of crustal accretion (Escartín et al., 2008). Asymmetric spreading has been interpreted as a consequence of the amount of magma flux where the proportion of magmatic extension is limited to ~30–50% relative to tectonic accretion (Tucholke et al., 2008). During periods of magma starvation, the normal fault needs to accommodate the absence of new material. In the case of a permanent starvation, it becomes a long-lived, low-angle fault (Dick et al., 1981; Tucholke et al., 1996). The fault offset represents a load which must be isostatically compensated. The lower part of the exposed footwall has a higher load deficit and moves upwards faster than the higher part. As a consequence, the detachment surface bends and eventually even past horizontal. This horizontal plane continues to move up which leads to doming of the footwall, due to the rigidity of the crust (Fig. 2). As a result, rocks of the lower plate (consisting of the lower crust and upper mantle) can be exposed at the surface (see Fig. 2B; Buck, 1988; Lavier et al., 1999). This part of the detachment fault system creates the oceanic core complex (OCC). Fully developed OCCs occur when a given detachment is active for a sufficiently long period of time (>1 Ma; Blackman et al., 2008).

Two prominent morphological characteristics of OCCs are the domal, turtleback shape of the complex and at many, large 100s of metres-scale corrugations on the exposed surface parallel to the spreading direction (Tucholke et al., 2001; Escartín & Canales, 2011). Those corrugations resemble large-scale mullions observed along detachment faults on land. Therefore OCCs are often called megamullions (Tucholke et al., 1998; Dick et al., 2008). OCCs are delimited up-dip by a breakaway, where the fault initially nucleated and down-dip by a termination which marks the boundary between the OCC and hanging wall (Figs. 3, 4; Tucholke et al., 2001; Escartín & Canales, 2011). OCCs occur most frequently at segment margins, especially at the inside corners of the ridge/transform fault intersections (Tucholke et al., 1997).

The general geophysical features of OCCs are a positive gravity anomaly (Cannat et al., 1995; Blackman et al., 2009), higher induced magnetisation (possibly caused by magnetite production during serpentinisation of peridotite), locally higher seismic velocities and higher seismicity in relation to the crust created on the conjugate plate (Blackman et al., 2009). A very important feature of OCCs is the asymmetry in the spacing of magnetic anomalies across the spreading axis, with a broader spread of magnetic zones on the ridge flank containing the OCC. This shows that OCCs form in the more rapidly accreting plates of asymmetric spreading segments (Dick et al., 1991; Hosford et al., 2003, Baines et al., 2007; Escartín et al., 2008; Blackman et al., 2009; Mallows & Searle, 2012).

The generation of OCCs is related to the spreading rate (see Section 5). Most occur at slow-spreading ridges (full rate 20–55 mm/year; Dick et al., 2003) and, in second place, at ridges with a spreading rate of 12–20 mm/year (transitional between slow- and ultraslow-spreading ridges; Dick et al., 2003). However, the style of formation is controlled more by melt supply than by spreading rate. For example, the common presence of mantle rock at the OCC surface is related to a regime with limited magma supply, where the flux of magma is too low to generate continuous gabbroic plutons. Hence, we distinguish various types of OCC.

The first one is typical of magma-rich conditions (Dick, 2010). The structure of the crust is similar to

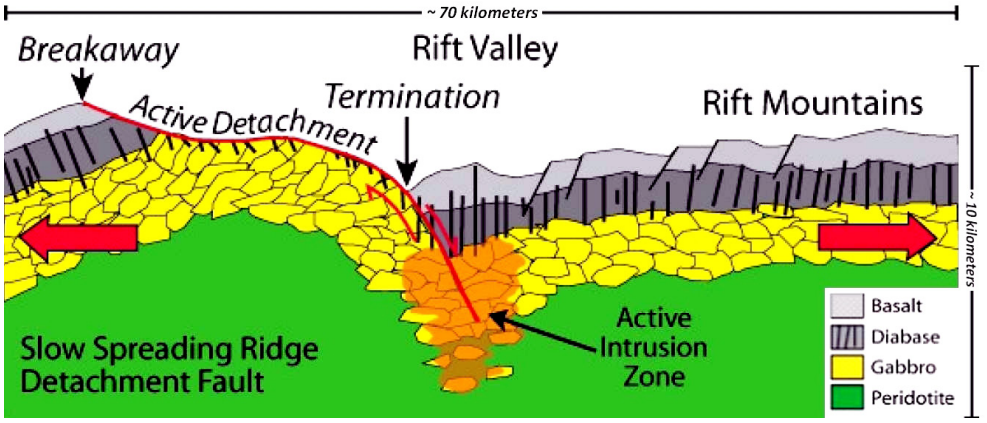

Fig. 3. Style of faulting at slow-spreading ridges with relatively high magma flux. Detachment fault exhumes oceanic core complex with predominance of gabbroic rocks on the sea floor

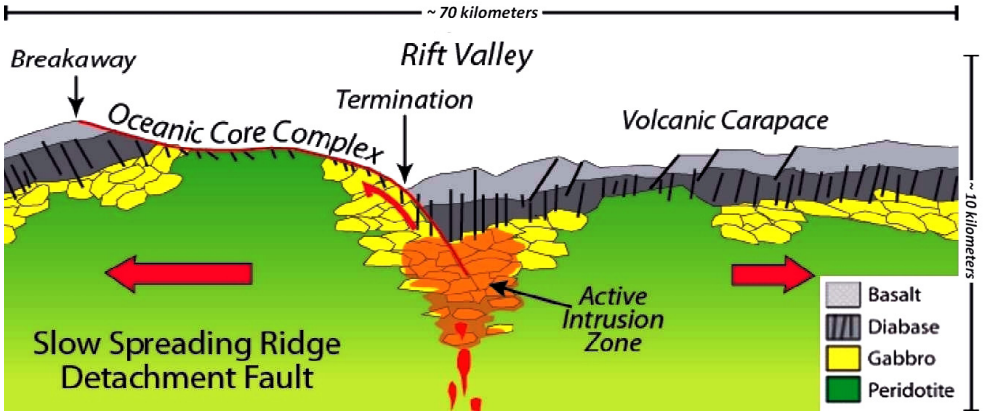

Fig. 4. Style of faulting at slow-spreading ridges with intermediate magma flux. Detachment fault exhumes oceanic core complex with relatively high amount of mantle rocks on the sea floor

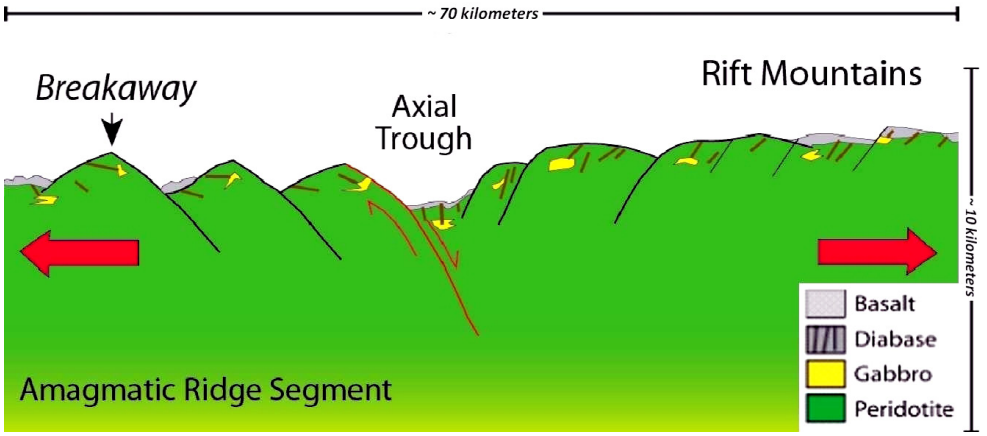

Fig. 5. Style of faulting at slow-spreading ridges with low magma flux. Block faulting exhumes peridotites with a minor amount of gabbroic rocks on the sea floor.

the model proposed by Dick (1989), which means it attenuates far from the segment centre. Gabbros are the commonest rocks observed on the OCC surface of this type (Fig. 3). The most important examples of such complexes are the Atlantis Massif at the Mid-Atlantic Ridge (MAR) and Atlantis Bank at SWIR (Dick, 2010).

The second type of OCC is related to sections of slow-spreading ridges with intermediate magma flux. Here, the structure of the crust can be best described with the Cannat (1996) model (Fig. 1B). Gabbros, as well as peridotites, are exposed at the surface (Fig. 4), reflecting the waning and waxing periods of magmatic activity. The best example

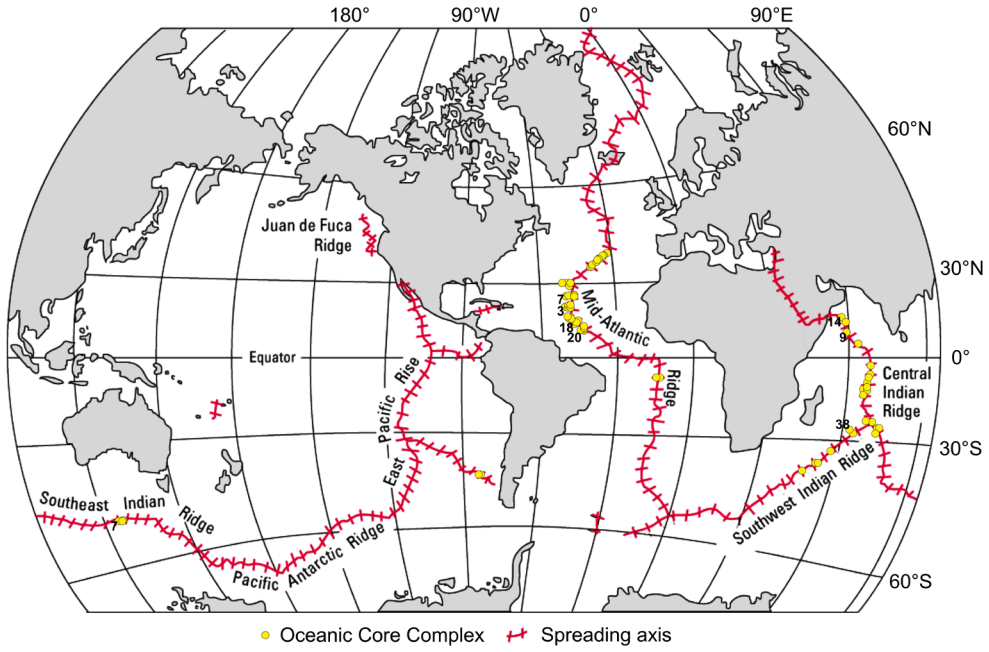

Fig. 6. Global distribution of oceanic core complexes associated with mid-ocean ridges. If more than one OCC was discovered at a given locality, the number of OCCs there is shown in black

of such an OCC is the Kane Megamullion at the Mid-Atlantic Ridge Kane (MARK) area (23°N; Dick, 2010).

When the magma flux is very low, peridotites and scattered basalts, with little or no gabbro appear at the sea floor (Fig. 5). The sea floor is 'smooth' compared to symmetric or asymmetric spreading (Cannat et al., 2006; Whitney et al., 2013), although still much rougher than at fast-spreading ridges, and block faulting is commoner than detachment faults with OCCs (Dick et al., 2003). This type of crustal structure is typical of ultraslow-spreading ridges (full rate < 12 mm/year) with the most pronounced examples found between 9 and 16°E along the Southwest Indian Ridge (SWIR) and in some sections along the Gakkel Ridge (Dick et al., 2003). Its formation is related to the Hess model as modified by Dick et al. (2003; see Fig. 1D).

5. Global distribution of OCCs

The importance of OCCs in crustal accretion is probably much greater than previously believed. Escartín et al. (2008) evaluated the 2,500 km section of the MAR between 12° and 35°N in terms of the symmetry of the spreading structure. Their research revealed an asymmetric accretion along almost half of this portion of the ridge. Baines et al. (2007) examined the eastern section of SWIR (54.75–62°E) in a similar way, and concluded that the individual segments in this section of SWIR spread asymmetrically. These studies trigerred a conclusion that OCCs constitute up to 25% of the crust along slow-spreading ridges (Smith et al., 2012). Here, we present a map of OCCs identified to date (Fig. 6). According to our literature analysis at least 172 OCCs have been discovered along mid-ocean ridges so far. This number does not include OCCs located far away from the active ridges, such as those identified near the Canary basin (Ranero & Reston, 1999; Reston et al., 2004), developed at back-arc basins (e.g., Godzilla Megamullion; Ohara et al., 2001, 2003a) or obducted on the continents as a part of an ophiolite (Nicolas et al., 1999; Nuriel et al., 2009; Tremblay et al., 2009; Manatschal et al., 2011; Maffione et al., 2013; Jousselin et al., 2013; Lagabrielle et al., 2015). Almost half (81) of the OCCs discovered are located at the MAR, with a high disparity in the frequency of occurrence between the northern (79) and southern (2) parts. Most of the others are situated along the other slow-spreading ridges: SWIR (43) and the Central Indian Ridge (35). Only 13 OCCs occur at intermediate spreading ridges: the Southeast Indian Ridge (SEIR; 11) and the Chile Ridge (2). No OCC has yet been found along fast-spreading ridges.

The full list of OCCs, together with spreading rate, is given in Table 1. Two OCCs at 5°05'S are located at the inside and outside corners of the ridge and a transform fault. They originally formed together as one OCC and then split about 0.5 Ma ago (Reston et al., 2002; Planert et al., 2010). The 15°45'N OCC is adjacent to the MAR on the western side and

Table 1. List of Oceanic Core Complexes (OCCs) according to their geographical location. MAR – Mid-Atlantic Ridge, SEIR – Southeast Indian Ridge, SWIR – Southwest Indian Ridge, spl – spinel, ol – olivine, opx – orthopyroxene, cpx – clinopyroxene, pl – plagioclase, PBP – plagioclase-bearing peridotites, SP – spinel peridotites, Cr# – chromium number (the molar Cr/(Al+Cr) ratio), Mg# – magnesium number (the molar Mg/(Mg + Fe) ratio), HF – hydrothermal field. The OCCs, in which peridotites were sampled, are shown in bold. Where serpentinites occur, they were included into the group of peridotites. See Section 6 for a discussion of their origin. Troctolites are included into gabbros. Spreading rates taken either from references specified or from Yu et al. (2013).

Locality	Number of OCC's	Full spreading rate (mm/year)	Main references	General sample description (% = wt.%)	Description of peridotites	Mineral chemistry of peridotites
5°05'S (IC High), MAR	1	32	Reston et al. (2002) Planert et al. (2010)	Mostly gabbros, some peridotites	Serpentinized strongly mylonitized; only fault gouge,	No data
5°05'S (OC High), MAR	1	32	Reston et al. (2002)	Not sampled	–	–
13°02'N, MAR	1	24	McLeod et al. (2009); Wilson (2010); Kostitsyn et al. (2012)	Mostly gabbros, diabases and basalts, 2% of peridotites; Ashadze I & Ashadze II HF's	Serpentinized peridotites	No data
13°19'N, MAR	1	24	McLeod et al. (2009); Wilson (2010)	Mostly basalts, many peridotites (~22%), few gabbros (<2%); active HF	Protogranular massive peridotites subsequently mylonitized; serpentinite schist of the fault gouge	No data
13°30'N, MAR	1	24	Beltenev et al. (2007); McLeod et al. (2009); Wilson (2010)	Mostly basalts, many peridotites, few gabbros (~2–3%); Semyenov HF	Serpentinized peridotites	No data
13°48'N, MAR	1	24	McLeod et al. (2009)	Mostly basalts, many peridotites (~22%)	No data	–
Other between 12°40' to 13°45'N, Segment 13°, MAR	20	24	Smith et al. (2006); Smith et al. (2008)	Not sampled	–	–
Logatchev Massif	1	24	Schroeder et al. (2007); Grevemeyer et al. (2013); Shipboard scientific party (2003)	Mostly peridotites (~70%) and gabbros; active HF	Plastically deformed harzburgites; serpentinized	No data relevant for this paper
14°54'N, MAR	1	24	Fujiwara et al. (2003)	Only peridotites	No data	–
Other between 14°20' and 15°20', Segment 15°, MAR	18	24	Smith et al. (2008)	Not sampled	–	–
15°40'N, MAR	1	25	Fujiwara et al. (2003)	Not sampled	–	–
15°45'N, MAR	1	25	Escartín et al. (2003)	Mostly gabbros, many diabases and peridotites	Serpentinized peridotites, not deformed; dunites impregnated and changed into troctolites	Cr# in spl indicates 14.3–15.3% of partial melting
16°20'N, MAR	1	26	Escartín & Cannat (1999)	Not sampled	–	–

Locality	Number of OCC's	Full spreading rate (mm/year)	Main references	General sample description (% = wt.%)	Description of peridotites	Mineral chemistry of peridotites
South Core Complex at 16°25'N, MAR	1	26	Smith et al. (2014)	Mostly basalt and diabase, many peridotites (~23%), some gabbro (~8%)	Serpentinized peridotites	No data
22°19'N, 10 km west off-axis, MAR	1	25	Dannovski et al. (2010)	Mostly peridotites (~55%), many diabases	100% serpentized harzburgites with relics of plastic mantle flow; ol, opx, probably cpx, no plag	No data
West of the 22°19'N OCC, MAR	1	25	Dannovski et al. (2010)	Not sampled	–	–
23°16'N, 46°31'W; 22°01'N, 45°48'W & 21°18'N, 45°39'W, MAR	3	25	Tucholke et al. (1998)	Not sampled	–	–
Kane Megamullion at 23°30'N, MAR	1	29	Dick et al. (2008); Dick et al. (2010); Tucholke et al. (2013)	Mostly peridotites (~`42%), many gabbros and basalts; active HF	Many harzburgites with relics of plastic mantle flow; 13.6% plagioclase peridotites with <1% of plag mostly	Cr# in spl indicates 11.3–13.8% of partial melting; 0.78–0.82 Mg# in ol within PBP; 0.89–0.92 Mg# in cpx in PBP vs 0.91–0.94 in SP
West of the Kane Megamullion, MAR	1	29	Tucholke et al. (1998)	Not sampled	–	–
TAG at 26°08'N, MAR	1	21	Zonenshain et al. (1989)	Mostly diabases and gabbros, no peridotites; TAG HF	–	–
26°17'E, 46°25'W, MAR	1	21	Tucholke et al. (1997)	Mostly basalt, some peridotites (~17%)	serpentinized	No data
Dante's Domes at 26°35'N, MAR	1	18	Tucholke et al. (2001)	Mostly basalt, much diabase, some peridotites	Serpentinites, higly altered	No data
Other between 25°34 and 26°58'N, MAR	7	18	Tucholke et al. (1998)	Not sampled	–	–
Atlantis Massif at 30°08'N, MAR	1	24	Karson et al. (2006); Tamura et al. (2008); Blackman et al. (1998); Blackman et al. (2002a); Schroeder & John (2004); McCaig (2010)	70% Peridotites/30% Gabbro; Lost City HF	Fault gouge assemblage and massive peridotites, half of them plag-bearing with 0.8–13% of plag	Cr# in spl indicates 15.0–18.3% of partial melting; 0.85–0.90; 0.85–0.91 Mg# in Ol within PBP vs 0.90–0.9in SP; 0.88–0.92 Mg# in cpx in PBP vs 0.90–0.93 in SP
The southern OCC at 29°56'N, MAR	1	24	Cann et al. (1997)	Many peridotites and basalts	Serpentinites of fault gouge assemblage	No data
The western OCC at 30°17'N, 9 km west off-axis, MAR	1	24	Blackman et al. (2002b); Blackman et al. (2008); Baines et al. (2003)	Not sampled	–	–

Locality	Number of OCC's	Full spreading rate (mm/year)	Main references	General sample description (% = wt.%)	Description of peridotites	Mineral chemistry of peridotites
Keystone Block between the western OCC and Atlantis Massif, MAR	1	24	Blackman et al. (2008)	Not sampled	–	–
Rainbow Massif, 36°14'N, north of AMAR segment, MAR	1	22	Andreani et al. (2014); Fouquet et al. (1998); Ildefonse et al. (2007); Gente et al. (2008); Dyment et al. (2009)	Mostly peridotites (~50%) and sediments, some basalts, hydrothermal products and gabbros (up to ~4%), diabase Rainbow, Ghost City and Clamstone HF's	Harzburgites equilibrated with spinels, serpentinized to varying degrees; some dunites	No data
Saldanha Massif at 36°30'N, MAR	1	25	Gràcia et al. (2000); Miranda et al. (2002)	Mostly peridotites and basalts; Saldanha HF	Only serpentinites	No data
Other between 33°30' to 38°30'N	8	23	Gràcia et al. (2000)	4 sampled, **3 with peridotites** and minor gabbros, 1 only with dolerites, HF in 2 of them	Serpentinites (1 site) and serpentinized harzburgites (2 sites)	No data relevant for this paper
Dragon Flag OCC at 49°39'E, SWIR	1	14	Zhao et al. (2013)	Mostly basalts, some peridotites, Dragon Flag HF	Serpentinized	–
53°E, SWIR	2	15	Zhou & Dick (2013)	**Mostly peridotites, many diabases, few gabbros in the western OCC**; Only gabbros in the eastern OCC	Serpentinized harzburgites, granular and mylonitic texture	Cr# in spl indicates 12% of partial melting
Atlantis Bank at 57°23'E, SWIR	1	14	Dick et al. (2000); Baines et al. (2003); Zhou & Dick (2013)	Mostly gabbros, many peridotites (up to 28%)	Partially serpentinized with protogranular and porphyroclastic texture	No data
FUJI dome at 63°45'E, SWIR	1	14	Fujimoto et al. (1999); Searle et al. 2003	3 Gabbros, 1 peridotite	Serpentinized Harzburgite	No data
Other between 61.2° and 65.5°E, SWIR	38	14 (30 ancient)	Cannat et al. 2009	Not sampled	–	–
25°S, Central Indian Ridge	1	64	Mitchell et al. (1998); Sato et al. (2009); Morishita et al. (2009)	Mostly basalts, many gabbros, few peridotites (~8%)	Fault gouge and massive peridotites. The latter are 2 cpx-harzburgites; one of them is plagioclase – bearing	Cr# in spl indicates 13–15% of partial melting; Mg# in ol and opx are similar for SP and PBP (~0.91)
Uraniva Hills at 25°18'S, Central Indian Ridge	1	64	Kumagai et al. (2008); Nakamura et al. (2009)	Mostly gabbros, few peridotites (~4%)	Plagioclase dunite, coming from the lower crust	Mg# in ol ~0.92; ~0.3 Ni wt.% in ol
m3 at 9°35'S, Central Indian Ridge	1	26	Kamesh Raju et al. (2012)	Only basalts	–	–

Locality	Number of OCC's	Full spreading rate (mm/year)	Main references	General sample description (% = wt.%)	Description of peridotites	Mineral chemistry of peridotites
Other between 8° and 17° S, Central Indian Ridge	5	46	Yi et al. (2014)	Mostly peridotites (4 of 5 sites; ~39%), many basalts and diabases, some gabbros (~11%)	Serpentinized harzburgites, some with coarse-grained granular texture; ol, opx, spl, cpx present	No data
m2 at 7°00'S, Central Indian Ridge	1	32	Kamesh Raju et al. (2012)	Only basalts	–	–
Vityaz Megamullion at 5°30'S, Central Indian Ridge	1	31	Drolia & DeMets (2005); Kamesh Raju et al. (2012)	Mostly basalts and peridotites (~50%)	Serpentinized	No data
5°6'N, Central Indian Ridge	1	25	Yu et al. (2013)	Not sampled	–	–
8.8–10.4°N, Carlsberg Ridge - Central Indian Ridge	9	25	Han et al. (2012)	Not sampled	–	–
Varun Bank at 13°22'E, 59°22'N, NW of the Owen fracture zone, Central Indian Ridge, off axis	1	120 (ancient)	Mudholkar et al. (2012)	Mostly peridotites and gabbros	No data	–
12.3–15.6°N, Sheba Ridge, Central Indian Ridge	14	40	Chamot-Rooke et al. (2008)	Not sampled	–	–
26°05'S, 70°30'E; 26°00'S, 70°40'E & 27°28'S, 73°12'E, SEIR	3	56	Bartsch (2014)	Not sampled	–	–
124°10'– 125°20'E, subsegment B3E, AAT, SEIR	7	88	Okino et al. (2004)	Not sampled	–	–
125°45'E, Segment B4, AAT, SEIR	1	88	Christie et al. (1998)	Only basalts	No peridotites	–
84°30'W, Segment V6, Chile Ridge	1	53	Karsten et al. (1999); Tebbens et al. (1997)	Not sampled	–	–
84°50'W, Segment V6, Chile Ridge	1	53	Karsten et al. (1999); Tebbens et al. (1997)	Not sampled	–	–

located to the north of the Fifteen-Twenty fracture zone (Escartín & Cannat, 1999; MacLeod et al., 2002; Escartín et al., 2003; Fujiwara et al., 2003; MacLeod et al., 2011). The 16°20′N detachment fault has never been sampled. However, peridotites were found in the proximity suggesting it may be an OCC (Escartín & Cannat, 1999). The TAG OCC (Tivey et al., 2003; Canales et al., 2007; de Martin et al., 2007; Zhao et al., 2012) is the only one where gabbros make up 100% of the sampled material from the plutonic footwall (Zonenshain et al., 1989; Reves-Sohn & Humphris, 2004). The only serpentinic minerals are embedded in grey-blue clay (Zonenshain et al., 1989). Keyston Block represents a detachment fault, where an OCC has not fully developed yet. The lower crust and the mantle rocks have not yet been unroofed (Cann et al., 1997; Blackman et al., 2008). The western OCC at 30°17′N has not been sampled so far (Blackman et al., 2008), but some corrugation-like structures have been identified on its surface (Blackman et al., 2002b).

Two potential OCCs in the segment 53°E have been identified based on domal shape, corrugations and plutonic rocks found on their surface (Zhou & Dick, 2013). At the eastern OCC, a 250-kg-block of gabbro was taken by TV grab, whereas peridotite predominates in the western OCC. In Atlantis Bank, no past hydrothermal activity has been discovered so far. However, evidence of that could have been removed during erosion, as Atlantis Bank was once an ocean island (Palmiotto et al., 2013). Although Atlantis Bank is the only OCC discovered so far in the region, asymmetric spreading in individual segments between 54.75 and 62°E (Baines et al., 2007) suggests that more OCCs may exist in the proximity. Thirty-eight corrugated surfaces located between 61.2° and 65.5°E and the 30-Ma chronozones identified by Cannat et al. (2009) are related to detachment faulting and potentially OCCs. The total surface of these OCCs constitutes about 4% surface of the area analysed (Cannat et al., 2006). Some of the OCCs located between 63.5 and 64.5°N were also described by Searle & Bralee (2007). Interestingly, the OCCs are more frequent beyond the chronozones older than 10 Ma (Cannat et al., 2009), when full spreading rate was higher (30 mm/year) compared to the present rate. This might suggest that detachment faulting was relatively commoner between 10 and 30 Ma, whereas amagmatic accretion with block faulting, typical of ultraslow spreading, became dominant after 10 Ma.

Among nine OCCs in the northern portion of the Central Indian Ridge –the Carlsberg Ridge between 8.8–10.4 °N, six are located near the rift valley and three are off-axis. Fourteen OCCs located further northeast, northeast of the Sheba Ridge have mainly been identified by their geomorphological features (Chamot-Rooke et al., 2008; Fournier et al., 2008, 2010). Interestingly, there is an asymmetry of the spreading and the crustal thickness in the Gulf of Aden with the thinner crust also in the plate northeast of the Sheba Ridge (d'Acremont et al., 2006). The Varun Bank is situated northwest of the Owen fracture zone at 13°22′ embedded in the 52-Ma-old crust (Exon et al., 2011). The full spreading rate during the generation of the OCC was 120 mm/year (Exon et al., 2011), which would be the fastest spreading rate estimated for OCCs all over the world.

The three OCCs at the westernmost SEIR have recently been discovered based on sea floor bathymetry by the German INDEX expeditions (Bartsch, 2014). The OCCs along the Antarctic-Australian Discordance (AAT) have been identified as OCCs based on prominent corrugations (up to 55 km; Okino et al., 2004) and gravimetric data predicting peridotites in the footwall (Christie et al., 1998). Only basalts were found over segment B4 (see Table 1; Pyle et al., 1992; Palmer et al., 1993; Pyle, 1993; Christie et al., 1998). No sampling occurred in subsegment B3E (Table 1; Okino et al., 2004). Two groups of megamullions resembling OCCs found along the Chile Ridge (segment V5) have not been sampled so far. However, serpentinites and fresh peridotites were recovered in the adjacent segment V5 (Karsten et al., 1999).

6. Peridotites recovered from OCCs

Based on geophysical studies, ultramafic rocks are often assumed to occur at the surface or subsurface of OCCs on account of their geophysical features (Christie et al., 1998; Okino et al., 2004). Among the 172 OCCs listed above, only ~39 were sampled by submersible, dredge or drilling (Table 1). Among these, peridotites were absent in seven OCCs. At least four of the seven were not sampled extensively enough to exclude the presence of peridotites; only basalts were found. Among 32 OCCs where mantle rocks were sampled, 20 are located along the MAR, 4 along the SWIR, and 8 along the Central Indian Ridge (Table 1).

6.1. Mid-Atlantic Ridge

With the exception of Atlantis Bank on the SWIR, the best-known OCCs, including the most extensively sampled 15°45′, Kane Megamullion and

Atlantis Massif OCCs, are located along the MAR. Oceanic expeditions have recovered mantle rocks from 20 OCCs along the ridge, mostly between the Marathon Fracture Zone (12°30′N) and the Azores Islands (38°N).

The only OCC peridotite samples from the southern MAR come from the western (inside-corner) 5°05′S OCC. Three dredges over the OCC recovered mostly gabbro. Some peridotites were found in the upper part of the footwall. They are strongly sheared and mylonitised. They likely constitute detachment fault gouge (Reston et al., 2002).

MacLeod et al. (2009) sampled 4 of the 24 OCCs from Segment 13°. The 13°19′N OCC consists of two structurally different parts. The western portion is rugged, more elevated, and exposes mainly basalt (only 11% peridotites). The eastern portion is enclosed in a smooth dome and exposes serpentinised peridotites (41%). The 13°30′N OCC has a similar structure and composition (MacLeod et al., 2009). Mostly basalts and peridotites have been collected along the OCC (Beltenev et al., 2007; MacLeod et al, 2009). Also in the 13°48′N OCC, most of the peridotites were recovered from a smooth domal surface, constituting 20% of the dredges. Additionally, MacLeod et al. (2009) provided some supplementary data on the OCC located further south, between 12°55′ and 13°12′N. The sole dredge over this OCC contained 2% (0.34 kg) peridotites (MacLeod et al., 2009; Wilson, 2010). Generally, it is difficult to infer the origin of peridotites from these data. However, the textures of the peridotites from the 13°19′N OCC indicate that they make up the footwall and are not only fault gouge (Table 1).

No information is available on peridotite dredged over the 14°54′N OCC (Fujiwara et al., 2003). Three of four boreholes from site 1270 at the Logatchev Massif yielded almost exclusively peridotites. Many gabbroic veins cutting the peridotites suggest the holes are in the vicinity of a larger gabbro body (Shipboard Scientific Party, 2003; Schroeder et al., 2007). Two boreholes (1275B, D) drilled in the OCC located on the opposite inside-corner, north of the Fifteen-Twenty fracture zone, recovered mostly gabbro and some troctolite (Schroeder et al., 2007). The troctolites appear to be impregnated dunites of mantle origin (Shipboard Scientific Party, 2003). More peridotites (~20%) were drilled and dredged on the 15°45′N OCC (Escartín et al., 2003). About 40–45% of them come from the detachment surface, the rest from the footwall. These are serpentinised but revealed no trace of high-temperature deformation. Additionally, we have estimated the degree of partial melting based on the molar Cr/(Al+Cr) ratios (Cr#) in six spinel grains (0.38–0.42; Escartín et al., 2003) using the model of Hellebrand et al. (2001). Our results indicate that the peridotites underwent 14.3 to 15.3% partial melting. Finally, serpentinised peridotites have recently been found by Smith et al. (2014) at South Core Complex at 16°25′N. They appeared in three of six dredges in the area constituting ~23% of the hauls, with ~8% gabbro.

Heavily serpentinised harzburgites predominate in 7 of 13 sampling sites on the southern wall of the 22°19′N OCC. They show relics of high-temperature crystal-plastic deformation, but no lower temperature deformation. Diabase and basalt predominate on the conjugate site of the rift (Dannovski et al., 2010). The best-studied and sampled OCC in terms of peridotite exposures is the Kane Megamullion. The core complex consists of six opposing domes, constituting a southern, central and northern region. About 1,238 kg of peridotites were collected by dredges and ROV dives, making up 42 wt.% of all rocks recovered, and being the most abundant (63 wt.%) in the central region. In the southern part, dunites constituted about half of all peridotites, contrasting to only 1–2% in the central and northern regions. Roughly 75–80% of peridotites were sampled from the detachment surface with their typical mineral phases and lower temperature deformation. The rest of the mantle rocks came from the headwalls and fault scarps that cut down into the OCC footwall. Some exhibit crystal-plastic deformation characteristic of fault surfaces that rooted into crystalline peridotite at high temperatures (Dick et al., 2008). Most of the peridotites are spinel harzburgites (62%). However, plagioclase-bearing peridotites are relatively common (14%), mostly from Adam & Eve domes. They usually contain less than 1% of relict plagioclase and its alteration products (Dick et al., 2010). Dick et al. (2010) used spinel Cr#s to estimate the degree of partial melting with the model of Hellebrand et al. (2001). They found a range 11.3–13.8% of partial melting, with the lowest values near the transform fault.

Five dives were performed in the southern hill of the Dante's domes OCC recovering two serpentinites from the bottom sections. Both were highly altered and subsequently veined by chlorite and amphibole. No primary phases or structures were present (Tucholke et al., 2001). At the 26°17′N OCC, situated in the vicinity, peridotites were found in one of six dredges. Basalt was recovered in the others. The peridotites are serpentinised, but they probably come from the plutonic footwall (Tucholke et al., 1997).

Dives to the southern wall of the Atlantis Massif OCC recovered 70% peridotites with 30% gabbros

and gabbro veins. These peridotites are variably altered (mainly serpentinised) rocks with a harzburgitic protolith. The peridotites have a porphyroclastic texture representing moderately distributed high-temperature crystal-plastic deformation (Karson et al., 2006). The central part of the OCC north of the transform wall was drilled by IODP, penetrating to 1,415 m in massive gabbro (Shipboard Scientific Party, 2005a, b). Few serpentinised peridotites are present in the upper 100 m of Hole 1309B and 1,415m deep Hole 1309D (0.5–3%) and in the following 400 m section of 1309D (4%; Shipboard Scientific Party, 2005a). No peridotites were recovered from the lower section of the latter hole (Shipboard Scientific Party, 2005b). Nevertheless, several olivine-rich troctolite intervals are interpreted as mantle peridotite hybridised by progressive reaction with basaltic melt (Drouin et al., 2007, 2009, 2010; Suhr et al., 2008). The peridotites from Hole D and from the upper sections of Hole B appear to be residual mantle harzburgites. Those from Hole D were subsequently impregnated by basaltic melt and contain interstitial plagioclase, while those from Hole B are variously serpentinised protogranular harzburgites (Tamura et al., 2008). The authors suggested 15.0–18.3% degree of partial melting in the spinel stability field. Additionally, the southern OCC on the opposite side of the Atlantis fracture zone was sampled by Cann et al. (1997). They found serpentinised peridotites in two of five dredges: one on the summit and one on the sloping rift valley wall.

Mantle peridotites (spinel harzburgites and minor dunites) were the predominant rock type recovered from the footwall of the Rainbow Massif (36°14′N). Some of them show evidence of late melt-rock (e.g., enhanced REE concentrations) and fluid-rock (e.g., enhanced Li and U concentrations) interaction. They are variously serpentinised, and some are talc-serpentine schists typical of fault gouge, found where detachment faulting cuts mantle peridotite. However, some show no deformation and are likely a part of the footwall block. Minor gabbros and gabbroic veins were also recovered (Ildefonse et al., 2007; Andreani et al., 2010, 2014). Serpentinites were found in four of five dives over the Saldanha Massif at 36°30′N, being dominant in some of them. Fractured basalt rubble recovered in the dredges is interpreted as hanging wall debris rafted on the detachment fault surface. Thus, the basement below the fault surface is largely serpentinised peridotite (Miranda et al., 2002).

Of the eight other potential OCCs from the region (Gràcia et al., 2000), four have been sampled (ARCYANA, 1975; Gràcia et al., 1997; Ribeiro da Costa et al., 2008). Three of the OCCs sampled contain serpentinised peridotites (Gràcia et al., 1997; Ribeiro da Costa et al., 2008). The two most southerly OCCs have been described by Gràcia et al. (1997). Peridotites, mostly serpentinised harzburgites, make up ~45 and ~85 wt.% of the dredged material, respectively. They usually predominate at the central part of these massifs, whereas equally abundant diabases make up the lower slopes. The diabases likely cross-cut the peridotites. Additionally, microgabbros occur, but very rarely. It is not clear whether peridotites predominate in the footwalls or just at the surface of the detachment faults. Hydrothermal fields were found in two of the four sampled OCCs (Gràcia et al., 2000; Escartín et al. 2014).

6.2. Southwest Indian Ridge

Partially serpentinised peridotites in the OCCs along the SWIR were reported over the Dragon Flag OCC, FUJI dome, Atlantis Bank and the western 53°E OCC. Although two dredges from the Dragon Flag OCC during Edul cruise (Mével et al., 1997) found only basalts, a plutonic footwall was expected based on bathymetry and seismic surveys, and gabbro was proposed (Zhao et al., 2013). However, this interpretation cannot be unique, as density, and P-wave and S-wave seismic velocities for gabbros and partially serpentinised peridotite overlap each other (Miller & Christensen, 1997). In fact, some serpentinised peridotites have been sampled very recently by another Chinese group (Zhou, 2015). More sampling occurred over the Fuji dome, but only one, intensely sheared, serpentinised harzburgite was sampled by submersible from the middle part of the northern slope of the dome. Being 1 of 47 samples collected in three dives, it constitutes 2.1% of the material recovered. More gabbroic rocks were recovered (two gabbros and one troctolite). These rocks imply outcrops of the lower crust and the upper mantle (Searle et al., 2003).

The Atlantis Bank OCC was drilled to 1,508 m on a wave-cut platform at the centre of the palaeo-ridge segment at which it formed. Other than two dykes in the upper few hundred metres, only gabbro was cored (Dick et al., 2000). Forty dredges recovered 1,230 kg of rock, of which 47% was gabbro and gabbro mylonites and 28% partially serpentinised peridotite and talc-serpentine schist. Low on the transform wall, granular peridotites were recovered in abundance, while sheared serpentinites and talc-serpentine schists were found overlying massive gabbro mylonites higher on the wall. The latter are interpreted as representing a discontinu-

ous sheet of fault gouge that lubricated the detachment fault by intrusion along it from where it cut uplifted mantle rock in the vicinity of the transform. The distribution of rock types recovered in dredges and by submersible shows that there is a contact between lower crustal gabbros and massive mantle peridotite that runs for nearly 30 kilometres along the eastern transform wall, progressively shoaling with increasing age to the south.

Ultramafic rocks have been found in four dredges performed over the western OCC at the segment 53°E (Zhou & Dick, 2013). Two dredges (550 kg) contained only peridotites with minor breccia. Two hundred fifty kg of material from another dredge contained mostly peridotites with minor diabase. Diabases predominate in the fourth dredge (17 kg), although gabbroic rocks and peridotites are also present. Zhou & Dick (2013) suggested that the dredged peridotites underwent 12% of partial melting based on Cr# in spinels.

6.3. Central Indian Ridge

Peridotite exposures along the Central Indian Ridge are reported from the Varun Bank, the Vityaz Megamullion and the 25°S OCC, as well as from several newly discovered OCCs between 8 and 17°S. No data are available for the Varun Bank peridotites at this time. Two peridotites were collected from the Vityaz Megamullion. One from the southeastern part of the megamullion adjacent to the Vityaz fracture zone was described by Kamesh Raju et al. (2012) as serpentinised peridotite. Peridotites have been found in four of the five OCCs identified between 8 and 17°S (8°10′, 9°55′, 10°50′,11°20′ and 13°15′S). These serpentinised harzburgites made up from 37 to 60% of the recovered material in these OCCs. Constituting from 66 to 80% of the plutonic material, they were more abundant than gabbros. Some peridotites show coarse-grained granular textures, whereas evidence of crystal-plastic deformation is rare. Gabbroic veins have not been observed within the mantle rocks.

Two types of peridotites were recovered by dives on the 25°S OCC (Morishita et al., 2009). The first type is highly deformed serpentinised peridotite fault gouge associated with the detachment surface. The second type is massive granular peridotite. Two of these were sampled from the top of the dome's west slope adjacent to the rift valley. They constitute roughly 8% of the material recovered from the largely gabbroic megamullion. Both samples are diopside-bearing harzburgites. They underwent 13–15% partial melting, as Morishita et al. (2009) calculated from the spinel Cr#s. One sample was altered due to reaction with granitic veins. Interstitial plagioclase is present (Morishita et al., 2009). A plagioclase dunite recovered from the Uraniva Hills, located further east (70°10′E) along the spreading direction, probably derives from the lower crust rather than from the mantle as its Ni content is relatively low (Nakamura et al., 2009; Table 1).

7. Discussion

7.1. Mantle peridotites and associated basalt

The percentage of peridotites in samples recovered from OCCs varies widely. OCCs with no occurrence of peridotites as well as those predominated by mantle rocks are listed above (Table 1). These data should be interpreted with caution, especially in the case where few plutonic rocks were found. The amount of plutonic rocks in the footwall is generally higher than that estimated from dredges, as basalts and diabases constitute a significant part of the haul. Whereas the peridotites, gabbros and some diabases underwent greenschist facies or higher-temperature alteration, the basalts are generally weathered, but otherwise unaltered, containing fresh plagioclase and olivine phenocrysts. This demonstrates a very different origin and these are best interpreted as hanging wall debris or even products of off-axis volcanism, as may have occurred at the Kane Megamullion (Dick et al., 2008). Diabases are more indeterminate as they could have come from either the hanging wall or the footwall where they may represent inliers of the dyke-gabbro transition in the footwall, or as fragments of the extrusive-dike transition in the overlying hanging wall (e.g., Dick et al., 2008; MacLeod et al., 2009; Wilson, 2010).

7.2. Percentage of peridotites in the footwall

Although minor inliers of the dyke-gabbro have been found in two (Atlantis Bank; Dick et al., 2000; Kane Megamullion; Dick et al., 2008) of three best-sampled OCCs, the available data (see Table 1; Sections 7.1 and 7.4; Escartín & Canales, 2011) show that OCC detachment footwalls are composed largely of plutonic rocks. Therefore, we find it useful to examine the ratio of peridotites to gabbroic rocks. For this reason, we have compiled data on total weight (when provided) or number of peridotites

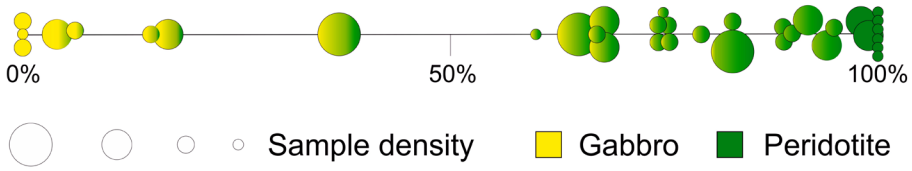

Fig. 7. The axis showing the percentage of peridotites among all plutonic rocks (peridotites + gabbroic rocks) for various OCCs. Peridotites predominate in most OCCs, as indicated also by the green colour. The empty circles show the degree of sampling. The largest circle (left) indicates very extensive sampling (725–1,908 kg). The smaller circles (right) correspond to moderately high sampling (40–68 kg or 24–73 samples), moderately low sampling (5.5–10 kg or 4–15 samples) and very low sampling (single sample or a general description), respectively. The western 53° OCC, with 817 kg of collected rocks, has been moved to the second group as the amounts of gabbro and peridotite within the dredges are not strictly constrained (see text). About 250 kg of plutonic rocks were collected in the eastern 53° OCC along the SWIR and the Rainbow Massif along the MAR. The former was classified in the moderately low-sampled group as one gabbroic block made up the haul. The latter was assigned to the moderately high-sampled group as only pie diagrams have been published to date (Andreani et al., 2014) which lowers the precision of our estimates

and gabbroic rocks in all OCCs sampled. Plutonic rocks were found in 35 of the 39 OCCs sampled. The percentage of peridotites varies from 0 to 100% (Fig. 7). Considering only the well-sampled OCCs (see caption to Fig. 7), the range is not significantly lower, being between 4 and 99%. The broad range we find shows that OCCs represent very different crustal architectures. We can identify at least five of them. At one extreme, crustal rocks are virtually absent (Fig. 1D), similar to those from the western 53° OCC (Zhou & Dick, 2013; Table 1). Three intermediate cases include 1) peridotites overlain by pillow lavas with relatively few associated dykes, as represented by the central domes of the Kane Megamullion (Dick et al., 2008), 2) plum-pudding of small gabbro bodies intruded into peridotite, overlain by dykes and pillow lavas, as to the north and south of the Fifteen-Twenty fracture zone (Cannat & Casey, 1995; see Fig. 1C), 3) small plutons capped by dykes and pillow lavas intruding laterally into massive peridotite, as at the Atlantis Massif (Blackman & Collins, 2010; Blackman et al., 2011; see Fig. 1B). At the other extreme, there are large plutons that extend virtually over the full length of a second-order ridge segment, as at Atlantis Bank. A full cover of sheeted dykes and pillow basalts occurs here, represented by inliers of the dyke-gabbro transition, and abundant pillow basalt in hanging wall debris (Fig. 1B).

Our compilation suggests that the majority of OCCs represent either the plum-pudding model (Fig. 1C) or nearly amagmatic spreading (Fig. 1D). We observe that 77% of all OCCs, and 73% of highly sampled OCCs, contain more peridotites than gabbro (Fig. 7). At 4 of 11 highly sampled OCCs, at least 90% of the plutonic rocks are peridotites (Fig.7). These observations imply that the model of Dick et al. (2003) for magmatic segments on at ultraslow-spreading ridges might even be applied to some ridge segments at slow-spreading ridges. However, this has to be treated with caution. Firstly, strongly oblique segments, characteristic of such spreading on ultraslow-spreading ridges, have not been described at slow-spreading ridges. Secondly, the proportion of gabbroic rock might be higher than calculated from the distribution of lithologies in the dredges. Unless there are large cross-faults or land-slips that cut down into the detachment footwall, serpentinite and talc-serpentinite fault gouge intruded laterally along the active fault plane may mask an underlying gabbro body, as at the Kane Megamullion (Dick et al., 2008; Xu et al., 2009) and the 15°45′ OCC (Escartín et al., 2003). This is related to the common presence of mantle peridotite in detachment fault regions. Furthermore, although it is often assumed that detachment fault root shallowly in the crust (Section 7.4), probably in the gabbro-dike transition zone (Escartín et al., 2003), given the abundance of peridotite mylonites, and crystal-plastically deformed amphibolitic gabbro mylonites in many OCCs (e.g., Kane Megamullion; Dick et al., 2008; Atlantis Bank; Dick et al., 1991, 2000), it would seem evident that detachment fault roots more deeply, passing through the dyke-gabbro transition. In this case, a significant part of gabbros could be cut and moved away with the hanging wall. Last but not least, massive gabbros are notoriously hard to dredge, but this refers to slow- as well as ultraslow-spreading ridges.

7.3. The origin of peridotites (fault gouge *vs* inside of the footwall)

As discovered in some OCCs, peridotites are very common rocks at the surface of detachment faults. However, the proportion of peridotites appears to be smaller under the surface of the footwall

(Dick et al., 2001, 2008; Escartín et al., 2003). We observe such a peculiar distribution of peridotites, because some of them are associated only with the detachment fault, related to the fact that serpentinised peridotites may easily lubricate a fault, relieving stress along the fault zone. Such serpentinised peridotites may originate from where the detachment fault roots into massive peridotite, either vertically where the crust is thin, or laterally, as in mantle peridotite emplaced into a transform zone, and migrate as a fault gouge up or along the fault. They are usually highly deformed and often consist of 100% alteration phases (serpentine plus talc; Dick et al., 2001, 2008; Morishita et al., 2009). Due to the extreme alteration, these peridotites have very limited use for evaluation of igneous petrogenesis. The remaining peridotites, however, are largely massive protogranular and porphyroclastic peridotites similar to those exposed in large peridotite massifs such as Table Mountain in the Bay of Islands Complex in Newfoundland, or in the Josephine Peridotite in the US states of Oregon and Washington. Where these occur in abundance, multiple dredges show that they are exposed over large regions, constituting large massifs exposed by detachment or block faulting onto the sea floor. As our data compilation shows, at least 18 of 32 OCCs in which peridotites were sampled contain massive peridotites (Table 1). We expect that the massive peridotite will be documented, at least locally, in most of the other 16 OCCs in the future.

7.4. What do massive peridotites represent?

When the lower crust is present, it is believed that the detachment faults root in gabbroic crust and not in the mantle (Dick et al., 2000; Escartín et al., 2003; Zhou & Dick, 2013). This is the case for the majority of OCCs, since gabbro plutons and gabbroic veins in peridotites are common throughout them (e.g., Karson et al., 2006; Dick et al., 2008; Morishita et al., 2009; Sections 6 and 7.2). Elsewhere, peridotite mylonites, representing the high temperature (600°C plus; Jaroslow et al., 1996) detachment faults where they rooted into upwelling mantle. Although these have not been found at all peridotite massifs, such fault zones are likely very narrow and easily missed by relatively few scattered dredges. Due to a strong contrast in physical properties with the underlying partially serpentinised peridotite, they are also easily removed by mass wasting. For example, while not previously reported from 14° to 17°N on the Mid-Atlantic Ridge, they have recently been found in the central and northern regions of the 16.5°N detachment fault system by Smith et al. (2014). Thus, the massive peridotite outcrops represent direct emplacement of crystalline peridotite onto the sea floor on faults that rooted up to several kilometres into the mantle beneath the spreading axis or adjacent transform.

The massive peridotites are sampled by drilling, dredging or diving in landslip headwalls or talus ramps, or along high-angle faults that crosscut the detachment fault surface. These scarps and faults, by simple geometry, expose only a few hundred metres depth below the detachment footwall, and thus we can assume that the peridotites represent only the few hundred upper metres of the mantle emplaced along the plate boundary.

7.5. What is the typical degree of partial melting of abyssal peridotites?

The degree of partial melting of peridotites is reflected in spinel composition (Hellebrand et al., 2001). We checked available publications for spinel analyses in massive peridotites, and found five data sets. Assuming that the mantle major element source composition is uniform (this is not always the case, as shown by Dick & Zhou, 2015), the degree of mantle partial melting calculated for these data vary within a range of 11.3–18.3% (Table 1). Melting under ridges is subadiabatic, driven by the difference between the adiabat and the solidus depression with decreasing depth. Therefore, the degree of melting increases during magma upwelling, reaching the highest value at the top of the melting column. In this light, the 11.3–18.3% partial melting range represents the highest degree of partial melting under the ridge where they were sampled.

Considering the decreasing degree of melting from the centre to the ends of segments (Niu & Batiza, 1994) and the fact that only spinels coming from locations far from the segment ends are included in the calculations mentioned above, we might interpret the value ~18% as being at the high end of melting along slow-spreading ridges. For comparison, Dick et al. (2010) suggested 8% partial melting for the Kane Transform and Wang et al. (2013) noted a similar value (~7.9%) for the Gallieni and Gazelle fracture zones, using the same method (Hellebrand et al., 2001). One example, where a higher degree of partial melting is observed at a segment end, is at the Vema Transform (11°N, MAR, full spreading rate 27.2 mm/year) where a successive section of peridotite, gabbro, dykes and overlying basalts occur along the transform wall (Auzende et al., 1989). The peridotites located between 9.5 and

6 Ma isochrones display a range of 9–13.5% partial melting in their upper part, up to 1 km from their boundary with gabbros. However, the degree of partial melting throughout the older intervals oscillated between 5 and 10% (Bonatti et al., 2003). This range in the degree of partial melting is also displayed by peridotites in the Owen fracture zone and the Romanche fracture zone (Choi et al., 2008).

7.6. Plagioclase-bearing peridotites as indicators of interaction with trapped melt

The OCC peridotites are typically spinel harzburgites (Section 6), which can be explained by the relatively high degree of partial melting in the OCC peridotites (Section 7.5). On the other hand, they are relatively rarely plagioclase bearing in comparison to the abyssal peridotites from the transform valleys, where 38% of all peridotites contain plagioclase (Dick, 1989). Plagioclase in abyssal peridotite is usually interpreted to have resulted from interaction with transient trapped melt (Dick 1989; Bonatti et al., 1992; Rampone et al., 1997). Additional evidence for such interaction is a relatively low olivine and pyroxene Mg# (Coogan, 2013). The relatively small amount of plagioclase-bearing peridotites among the OCC peridotites facilitates the investigation on partial melting in the mantle, as original Cr# in spinels can be preserved, whereas reaction with late impregnating melts generally elevates the Cr# as Al goes into the plagioclase (Dick et al., 2010). On the other hand, the percentage of plagioclase in the plagioclase-bearing peridotites allows us to estimate the amount of trapped melt. For example, assuming a normative percentage of plagioclase in MORB as high as 50–55% (Wilkinson, 1986), we can estimate that ~2% of plagioclase indicates ~4% of trapped melt.

Careful mineral mode estimation in the OCC peridotites has revealed that plagioclase-bearing peridotites occur in every OCC where the estimation was made (Table 1). This is the case for the Kane Megamullion (Dick et al., 2010), the Atlantis Massif (Tamura et al., 2008) and the 25°S OCC (Morishita et al., 2009). Only interstitial clinopyroxenes and no plagioclase are reported by Dannovski et al. (2010) for 22°19′N at the MAR. However, the samples were 100% altered. Thus, the presence of plagioclase cannot be excluded even there. Plagioclase only ever occurs in part of the peridotites. This is the case for the Atlantis Massif and 25°S OCC. The plagioclase-bearing peridotites make up ~14% of the mantle rocks in the most representative set of data, which is the Kane Megamullion.

In most specimens from the Kane Megamullion, the Atlantis Massif and the 25°S OCC, plagioclase constitutes less than 1% of plagioclase-bearing peridotite, although only in several samples approaching more than 5%. The average olivine and clinopyroxene Mg# is significantly lower in plagioclase-bearing peridotites than in spinel peridotites in the Kane Megamullion and the Atlantis Massif, while it is similar in the 25°S OCC (Table 1). However, the plagioclase also occurs as an interstitial phase in the latter. To summarise, it seems that many abyssal peridotites interacted with a MORB-like melt. The irregular distribution of plagioclase (see also Section 6) indicates a non-uniform flow of melt.

As mentioned above, plagioclase-bearing peridotites occur more frequently in the transform peridotites than the peridotites originating from OCCs. In addition, they show higher modal amounts of plagioclase, because the average volume of plagioclase exceeds 2% in the most plagioclase-bearing transform peridotites (Dick, 1989). The highly variable plagioclase contents indicate that the flow of transient melt was also non uniform (Dick, 1989). However, the greater abundance of plagioclase and the frequency of plagioclase-bearing peridotites suggest a more intensive late-stage melt impregnation in the transform peridotites than in the peridotites originating from OCCs.

7.7. Peridotite-hosted hydrothermal fields

Analysis of the literature (Table 1) shows that active hydrothermal fields have been found at 12 of 39 sampled OCCs, which suggests these provide exceptionally favourable conditions for their generation. Tivey et al. (2003), McCaig et al. (2007) and Tucholke et al. (2013) recognised the important role of active detachment faults as main conduits for hydrothermal circulation. The root zone of such a circulation can be located up to 11 km below the sea floor (Silantiev et al., 2009a, b). Thus, hydrothermal fluids extensively react with ultramafic rocks during ascent, buffering vent fluid chemistry, as in the case of the Lost City hydrothermal field at the Atlantis Massif (Kelley et al., 2001). It influences the composition of the ore minerals generated to those fluids. For example, massive sulphides hosted in peridotites at the Logatchev Massif display a peculiar composition (Petersen et al., 2009). Other hydrothermal fields hosted in peridotites have to be investigated in order to determine whether or not

they generate a new class of ore deposit, different from basalt-hosted deposits.

8. Conclusions

1. Oceanic core complexes are common features in the oceanic crust architecture of slow-spreading ridges. At least 172 oceanic core complexes have been identified on the basis of bathymetry and geophysical data. Most were discovered during the last decade. They occasionally occur as isolated massifs, but it is usual for them to occur in groups of up to 39 OCCs in one extended segment. Thus, we can expect to discover dozens of new OCCs as more detailed mapping occurs along slow-spreading mid-ocean ridges. Undoubtedly, there are also many hidden beneath the sedimentary cover far from active rifts. Therefore, detachment faulting is a common and not an anomalous mode of crustal accretion at slow-spreading ridges.
2. Only 39 of 172 OCCs have been sampled so far. However, as 32 of them contain peridotites, they are clearly common in their footwall. Moreover, peridotites predominate in the plutonic footwall of the majority of them. The high number of OCCs and their relatively large dimensions compared to other settings of oceanic crust where peridotites are involved allow earth scientists to focus on sampling of a complete section of the upper mantle and lower crust by extensive dredging, diving and drilling in megamullion systems.
3. Massive OCC peridotites represent the very top of the melting column beneath ocean ridges. They are typically spinel harzburgite and show 11.3–18.3% partial melting, assuming a primitive upper mantle source composition, in the segment centres, generally representing the maximum degree of melting along a segment. The degree of melting is lower in the segment ends and presumably in the lower part of the melting column.
4. The OCC peridotites often contain plagioclase, which together with low pyroxene and olivine Mg#s generally indicates a late-stage impregnation with MORB-like melt. The pattern of the plagioclase distribution suggests a non-uniform flow of melt.
5. Based on the above, OCC peridotites away from segment ends and transforms can be treated as a new class of abyssal peridotites. These differ from the transform peridotites by higher degrees of partial melting and lower interactions with subsequent transient melts. At the same time, we are aware that not enough sampling and analysis have been performed on OCC peridotites, and this distinction requires further substantiation. Therefore, we wish to emphasise that OCC peridotite samples represent an opportunity, not yet fully exploited, to investigate partial melting, melt transport, ultramafic-hosted hydrothermal processes and both large- and local-scale mantle heterogeneity.

Acknowledgements

We thank Marta Ciazela, Tobias Gärtner, Fuwu Ji and Joy Reid for dedicating some of their time to help us write this paper. The preparation and research for it was supported by the Polish Ministry of Science and Higher Education within Diamond Grant program DI2012 2057 42. Henry Dick received support from the US National Science Foundation (grant number NSF/OCE 1155650).

References

Andreani, M., Ildefonse, B., Delacour, A., Escartín, J., Godard, M. & Dyment, J., 2010. Tectonic Structure and Internal Composition of the Rainbow Massif, Mid-Atlantic Ridge 36°14'N. Abstract presented at *AGU Chapman Conference*, Agros, Cyprus.

Andreani, M., Escartín, J., Delacour, A., Ildefonse, B., Godard, M., Dyment, J., Fallick, A.E. & Fouquet, Y., 2014. Tectonic structure, lithology, and hydrothermal signature of the Rainbow massif (Mid-Atlantic Ridge 36°14'N). *Geochemistry, Geophysics, Geosystems* 15, 3543–3571.

ARCYANA, 1975. Transform fault and rift valley from bathyscaph and diving saucer. *Science* 190, 108–116.

Auzende, J.-M., Bideau, D., Bonatti, E., Cannat, M., Honnorez, J., Lagabrielle, Y., Malavieille, J., Mamaloukas-Frangoulis, V. & Mével, C., 1989. Direct observation of a section through slow-spreading oceanic crust. *Nature* 337, 726–729.

Baines, A.G., Cheadle, M.J., Dick, H.J.B., Hosford Scheirer, A., John, B.E., Kusznir, N.J. & Matsumoto, T., 2003. A mechanism for generating the anomalous uplift of oceanic core-complexes: Atlantis Bank, SW Indian Ridge. *Geology* 31, 1105–1108.

Baines, A.G., Cheadle, M.J., Dick, H.J.B., Hosford Scheirer, A., John, B.A., Kusznir, N. J. & Matsumoto, T., 2007. Evolution of the Southwest Indian Ridge from 55°45'E to 62°E: Changes in Plate-Boundary Geometry Since 26 Ma. *Geochemistry, Geophysics, Geosystems* 8, Q06022.

Bagherbandi, M., Tenzer, R. Sjöberg, L.E. & Novák, P., 2013. Improved global crustal thickness modeling

based on the VMM isostatic model and non-isostatic gravity correction. *Journal of Geodynamics* 66, 25–37.

Bartsch, C., 2014. *Structural and magnetic investigation of two spreading systems around the Rodriguez Triple Junction with respect to hydrothermal activity*. Naturwissenschaftliche Fakultät, Gottfried Wilhelm Leibniz Universität Hannover, PhD thesis, 237 pp.

Beltenev, V., Ivanov, V., Rozhdestvenskaya, I., Cherkashov, G.,Stepanova, T., Shilov, V., Pertsev, A., Davydov, M., Egorov, I., Melekestseva, I., Narkevsky, E. & Ignatov, V., 2007. A new hydrothermal field at 13°30′N on the Mid-Atlantic Ridge. *InterRidge News* 16, 9–10.

Blackman, D.K. & Collins, J.A., 2010. Lower crustal variability and the crust/mantle transition at the Atlantis Massif oceanic core complex. *Geophysical Research Letters* 37, L24303.

Blackman, D.K., Cann, J.R., Janssen, B. & Smith, D.K., 1998. Origin of extensional core complexes: Evidence from the Mid-Atlantic Ridge at Atlantis Fracture Zone. *Journal of Geophysical Research* 103, 315–333.

Blackman, D.K., Karson, J.A., Kelley, D.S., Cann, J.R., Gretchen L., Früh-Green, G.L., Gee, J.S., Hurst, S.D., John, B.E., Morgan, J., Nooner, S.L., Ross, D.K, Schroeder, T.J. & Williams, E.A., 2002a. Geology of the Atlantis Massif (Mid-Atlantic Ridge, 30°N): Implications for the evolution of an ultramafic oceanic core complex. *Marine Geophysical Research* 23, 443–469.

Blackman, D.K., Lyons, S., Cann, J. & Morgan, J., 2002b. *Morphology of a 9 Myr old oceanic core complex: Mid Atlantic Ridge 30°N, 43°W*. Abstract presented at AGU Fall Meeting, San Francisco, USA.

Blackman, D.K., Karner, G.D. & Searle, R.C., 2008. Three-dimensional structure of oceanic core complexes: Effects on gravity signature and ridge flank morphology, Mid-Atlantic Ridge, 30°N. *Geochemistry,Geophysics,Geosystems* 9, 1–20.

Blackman, D.K., Canales, J.P. & Harding, A., 2009. Geophysical signatures of oceanic core complexes. *Geophysical Journal International* 178, 593–613.

Blackman, D.K., Ildefonse, B., John, B.E., Ohara, Y., Miller, D.J., Abe, N., Abratis, M., Andal, E.S., Andréani,M., Awaji, S., Beard, J.S., Brunelli, D., Charney, A.B., Christie, D.M., Collins, J., Delacour, A.G., Delius, H., Drouin, M., Einaudi, F., Escartín, J., Frost, B.R., Früh-Green, G., Fryer, P.B., Gee, J.S., Godard, M., Grimes, C.B., Halfpenny, A., Hansen, H.-E., Harris, A.C., Tamura, A., Hayman, N.W., Hellebrand, E., Hirose, T., Hirth, J.G., Ishimaru, S., Johnson, K.T.M., Karner, G.D., Linek, M., MacLeod, C.J., Maeda, J., Mason, O.U., McCaig, A.M., Michibayashi, K., Morris, A., Nakagawa, T., Nozaka, T., Rosner, M.,Searle, R.C., Suhr, G., Tominaga, M., von der Handt, A., Yamasaki, T. & Zhao, X., 2011. Drilling constraints on lithospheric accretion and evolution at Atlantis Massif, Mid-Atlantic Ridge 30°N. *Journal of Geophysical Research* 116, B07103.

Bodinier, J.-L. & Godard, M. 2003. *Orogenic, Ophiolitic and Abyssal Peridotites*, [In:] R.W. Carlson (Ed.): Treatise on Geochemistry. Vol. 2: The Mantle and Core. Elsevier, Amsterdam, 103–170.

Bonatti, E., Peyve, A., Kepezhinskas, P., Kurentsova, N., Seyler, M., Skolotnev, S. & Udintsev, G., 1992. Upper mantle heterogeneity below the Mid-Atlantic Ridge, 0°–15°N. *Journal of Geophysical Research* 97, 4461–4476.

Bonatti, E., Ligi, M., Brunelli, D., Cipriani, A., Fabretti, P., Ferrante, V., Gasperini, L. & Ottolini, L., 2003. Mantle thermal pulses below the Mid-Atlantic Ridge and temporal variations in the formation of oceanic lithosphere. *Nature* 423, 499–505.

Buck, R.W., 1988. Flexural rotation of normal faults. *Tectonics* 7, 959–973.

Canales, J.P., Detrick, R.S., Bazin, S., Harding, A.J. & Orcutt, J.A., 1998. Off-axis crustal thickness across and along the East Pacific Rise within the MELT area. *Science* 280, 1218–1221.

Canales, J.P., Detrick, R.S., Toomey, D.R. & Wilcock, W.S.D., 2003. Segment-scale variations in the crustal structure of 150–300 kyr old fast spreading oceanic crust (East Pacific Rise, 8°15′–10°5′N) from wide-angle seismic refraction profiles. *Geophysical Journal International* 152, 766–794.

Canales, J.P., Sohn, R.A. & deMartin, B.J., 2007. Crustal structure of the Trans-Atlantic Geotraverse (TAG) segment (Mid-Atlantic Ridge, 26°10′N): Implications for the nature of hydrothermal circulation and detachment faulting at slow spreading ridges. *Geochemistry, Geophysics, Geosystems* 8, Q08004.

Cann, J.R., Blackman, D.K., Smith, D.K., McAllister, E., Janssen, B., Mello, S., Avgerinos, E., Pascoe, A.R, & Escartín, J., 1997. Corrugated slip surfaces formed at North Atlantic ridge-transform intersections. *Nature* 385, 329–332.

Cannat, M., 1993. Emplacement of mantle rocks in the seafloor at mid-ocean ridges. *Journal of Geophysical Research* 98, 4163–4172.

Cannat, M., 1996. How thick is the magmatic crust at slow spreading oceanic ridges. *Journal of Geophysical Research* 101, 2847–2857.

Cannat, M. & Casey, J.F., 1995. An Ultramafic Lift at the Mid-Atlantic Ridge: Successive Stages of Magmatism in Serpentinized Peridotites from the 15°N Region. *Petrology and Structural Geology* 6, 5–34.

Cannat, M., Mével, C., Maia, M., Deplus, C., Durand, C., Gente, P., Agrinier, P., Belarouchu, A., Dubuisson, G., Humler, E. & Reynolds, J., 1995. Thin crust, ultramafic exposures, and rugged faulting patterns at the Mid-Atlantic Ridge (22°–24°N). *Geology* 23, 49–52.

Cannat, M., Sauter, D., Mendel, V., Ruellan, E., Okino, K., Escartín, J., Combier, V. & Baala, M., 2006. Modes of seafloor generation at a melt-poor ultraslow-spreading ridge. *Geology* 34, 605–608.

Cannat, M., Sauter, D., Escartín, J., Lavier, L. & Picazo, S., 2009. Oceanic corrugated surfaces and the strength of the axial lithosphere at slow spreading ridges. *Earth and Planetary Science Letters* 288, 174–183.

Carlson, R.W., 2003. *Introduction to Volume 2*. [In:] R.W. Carlson (Ed.): Treatise on geochemistry. Vol. 2: The Mantle and Core. Elsevier, Amsterdam, 15–21.

Chamot-Rooke, N., Fournier, M., Petit, C., Fabbri, O., Huchon, P., Lepvrier C. & Maillot, B., 2008. *Sheba Ridge's*

Oceanic Core Complexes. Abstract presented at EGU General Assembly, Vienna, Austria.

Choi, S.H., Mukasa, S.B. & Shervais, J.W., 2008. Initiation of Franciscan subduction along a large-offset fracture zone: Evidence from mantle peridotites, Stonyford, California. *Geology* 36, 595–598.

Christie, D.M.,West, B.P., Pyle, D.G. & Hanan, B.B., 1998. Chaotic topography, mantle flow and mantle migration in the Australian-Antarctic discordance. *Nature* 394, 637–644.

Coogan, L.A., 2013. *The lower oceanic crust*. Manuscript submitted for publication. 113 pp.

d'Acremont, E., Leroy, S., Maia, M., Patriat, P., Beslier, M.-O., Bellahsen, N., Fournier, M. & Gente, P., 2006. Structure and evolution of the eastern Gulf of Aden: Insights from magnetic and gravity data (Encens-Sheba MD117cruise). *Geophysical Journal International* 165, 786–803.

Dannowski, A., Grevemeyer, I., Ranero, C.R., Ceuleneer, G., Maia, M., Morgan, J.P. & Genteet, P., 2010. Seismic structure of an oceanic core complex at the Mid-Atlantic Ridge, 22°19'N. *Journal of Geophysical Research* 115, 1–15.

deMartin, B.J., Sohn, R.A., Canales, J.P. & Humphris, S.E., 2007. Kinematics and geometry of active detachment faulting beneath the Trans-Atlantic Geotraverse (TAG) hydrothermal field on the Mid-Atlantic Ridge. *Geology* 35, 711–714.

Dick, H.J.B., 1989. *Abyssal peridotites, very slow-spreading ridges and ocean ridge magmatism*. [In:] A.D. Saunders & M.J. Norry (Eds): Magmatism in the Ocean Basins. Geological Society, London, 71–105.

Dick, H.J.B., 2010. *Tale of two core complexes: Contrasting crustal architecture and fault geometries*. Abstract presented at AGU Chapman Conference, Agros, Cyprus.

Dick, H.J.B. & Zhou, H., 2015. Ocean rises are products of variable mantle composition, temperature and focused melting. *Nature Geoscience* 8, 68–74.

Dick, H.J.B., Bryan, W.B. & Thompson, G., 1981. *Low-angle faulting and steady-state emplacement of plutonic rocks at ridge-transform intersections*. [In:] A.R. Ritsema (Ed.): European Seismological Commisssion Meeting and Abstracts. Eos, Transaction American Geophysical Union 62, 406.

Dick H.J.B., Schouten, H., Meyer, P,S., Gallo, D.G., Bergh, H., Tyce, R., Patriat, P., Johnson, K.T.M., Snow, J. & Fisher, A., 1991.Tectonic evolution of the Atlantis II Fracture Zone. [In:] R.P. Von Herzen, P.T. Robinson et al. (Eds): *Proceedings of the Ocean Drilling Program, Scientific Results* 118, 359–398.

Dick H.J.B., Natland J.H., Alt J.C., Bach, W., Bideau, D., Gee, J.S., Haggas, S., Hertogen, J.G.H., Hirth, G., Holm, P.M., Ildefonse, B., Iturrino, G.J., John, B.E., Kelley, D.S., Kikawa, E., Kingdon, A., LeRoux, P.J., Maeda, J., Meyer, P.S., Miller, D.J., Naslund, H.R., Niu, Y.-L. Robinson, P.T., Snow, J., Stephen, R.A., Trimby, P.W., Worm, H.-U. & Yoshinobu, A., 2000. A long in situ section of lower oceanic crust: Results of ODP Leg 176 drilling at the Southwest Indian Ridge. *Earth and Planetary Science Letters* 179, 31–51.

Dick, H.J.B., Arai, S., Hirth, G., John, B.J. & KROO-06 Scientific Party, 2001. A subhorizontal cross-section through the crust mantle boundary at the SW Indian Ridge. *Geophysical Research Abstracts* 3, 794.

Dick, H.J.B., Lin, J. & Schouten, H., 2003. An ultraslow spreading class of ocean ridge. *Nature* 426, 405–412.

Dick, H.J.B., Natland, J.H. & Ildefonse, B., 2006. Past and future impact of deep drilling in the oceanic crust and mantle. *Oceanography* 19, 72–80 .

Dick, H.J.B., Tivey, M.A. & Tucholke, B.E., 2008. Plutonic foundation of a slow-spreading ridge segment: Oceanic core complex at Kane Megamullion, 23°30'N, 45°20'W. *Geochemistry, Geophysics, Geosystems* 9, Q05014.

Dick, H.J.B., Lissenberg, C.J., & Warren, J.M., 2010. Mantle melting, melt transport, and delivery beneath a slow-spreading ridge: The paleo-MAR from 23°15'N to 23°45'N. *Journal of Petrology* 51, 425–467.

Drolia, R.K. & DeMets, C., 2005. Deformation in the diffuse India-Capricorn-Somalia triple junction from a multibeam and magnetic survey of the northern Central Indian Ridge, 3°S–10°S. *Geochemistry, Geophysics, Geosystems* 6, Q09009.

Drouin, M., Godard, M. & Ildefonse, B., 2007. Origin of olivine-rich troctolites from IODP Hole U1309D in the Atlantis Massif (Mid-Atlantic Ridge): petrostructural and geochemical study. *Eos, Transactions American Geophysical Union* 89(53), Fall Meet. Suppl., Abstract T53B-1300.

Drouin, M., Godard, M., Ildefonse, B., Bruguier, O. & Garrido, C.J., 2009. Geochemical and petrographic evidence for magmatic impregnation in the oceanic lithosphere at Atlantis Massif, Mid-Atlantic Ridge (IODP Hole U1309D, 30°N). *Chemical Geology* 264, 71–88.

Drouin, M., Ildefonse, B. & Godard, M., 2010. A microstructural imprint of melt impregnation in slow spreading lithosphere: Olivine-rich troctolites from the Atlantis Massif, Mid-Atlantic Ridge, 30°N, IODP Hole U1309D. *Geochemistry, Geophysics, Geosystems* 11, Q06003.

Dyment, J., Bissessur, D., Bucas, K., Cueff-Gauchard, V., Durand, L., Fouquet, Y., Gaill, F., Gente, P., Hoise, E., Ildefonse, B., Konn, C., Lartaud, F., LeBris, N., Musset, G., Nunes, A., Renard, J., Riou, V., Tasiemski, A., Thibaud, R., Torres, P., Yatheesh, V., Vodjdani, I. & Zbinden, M, 2009. Detailed investigation of hydrothermal site Rainbow, Mid-Atlantic Ridge, 36°13'N: Cruise MoMARDream. *InterRidge News* 18, 22–24.

Dziewonski, A.M. & Anderson, D.L, 1981. Preliminary reference Earth model. *Physics of the Earth and Planetary Interiors* 25, 297–356.

Escartín, J. & M. Cannat, M., 1999. Ultramafic exposures and the gravity signature of the lithosphere near the Fifteen-Twenty Fracture Zones (Mid-Atlantic Ridge, 14–16° N). *Earth and Planetary Science Letters* 171, 411–424.

Escartín, J. & Canales, J.P., 2011. Detachments in oceanic lithosphere: Deformation, magmatism, fluid flow, and ecosystems. *Eos, Transactions American Geophysical Union* 92, 31.

Escartín, J., Mével, C., Mac-Leod, C.J. & McCaig, A.M., 2003. Constraints on deformation conditions and the origin of oceanic detachments: The Mid-Atlantic Ridge core complex at 15°45′N. *Geophysics, Geochemistry, Geosystems* 4, 1067.

Escartín, J., Smith, D.K., Cann, J. Schouten, H., Langmuir, C.H. & Escrig, S., 2008. Central role of detachment faults in accretion of slow-spread oceanic lithosphere. *Nature* 455, 790–794.

Escartín, J., Soule, S.A., Cannat, M., Fornari, D.J., Düşünür, D. & Garcia, R., 2014. Lucky Strike seamount: Implications for the emplacement and rifting of segment-centered volcanoes at slow spreading mid-ocean ridges. *Geochemistry, Geophysics, Geosystems* 15, 4157–4179.

Exon, N., Pandey, D., Gallagher, S., Rajan, S., Coffin, M., Takai, K. & other workshop participants, 2011. *Detailed report on Indian Ocean IODP workshop*. Integrated Ocean Drilling Program, Goa, India, 50 pp.

Fouquet, F., Barriga, F., Charlou, J.L., Elderfield, H., German, C.R., Ondreas, H., Parson, L., Radford-Knoery, J., Relvas, J., Ribeiro, A., Schultz, A., Appriroual, R., Cambon, P., Costa, I., Donval, J.P., Douville, E., Landure, J.Y., Normand, A., Pelle, H., Ponsevera, E., Riches, S., Santana, H. & Stephan, M., 1998. FLORES diving cruise with the Nautile near the Azores – First dives on the Rainbow field: hydrothermal sweater/mantle interaction. *InterRidge News* 7, 24–28.

Fournier, M., Chamot-Rooke, N., Petit, C., Huchon, P., Al-Kathiri, A., Audin, L., Beslier, M.-O., d'Acremont, E., Fabbri, O., Fleury, J.-M. Khanbari, K., Lepvrier, C., Leroy, S., Maillot, B. & Merkouriev S., 2010. Arabia-Somalia plate kinematics, evolution of the Aden-Owen-Carlsberg triple junction, and opening of the Gulf of Aden. *Journal of Geophysical Research* 115, B04102.

Fournier, M., Petit, C., Chamot-Rooke, N., Fabbri, O., Huchon, P., Maillot, B. & Lepvrier, C., 2008. Do ridge–ridge–fault triple junctions exist on Earth? Evidence from the Aden–Owen–Carlsberg junction in the NW Indian Ocean. *Basin Research* 20, 575–590.

Fujimoto, H., Cannat, M., Fujioka, M.K., Gamo, T., German, C., Mével, C., Muench, U., Ohta, S., Oyaizu, M., Parson, L., Searle, R., Sohrin, Y. & T. Yama-ashi, T., 1999. First submersible investigation of mid-ocean ridges in the Indian Ocean. *InterRidge News* 8, 22–24.

Fujiwara, T., Lin, J. Matsumoto, T. Kelemen, P.B. Tucholke, B.E. & Casey, J.F., 2003. Crustal Evolution of the Mid-Atlantic Ridge near the Fifteen-Twenty Fracture Zone in the last 5 Ma. *Geochemistry, Geophysics, Geosystems*. 4(3), 1024.

Gente, P., Thibaud, R., Dyment, J., Fouquet, Y., Ildefonse, B., Hoisé, E., Bissessur, D., Yatheesh, V. & the MOMARDREAM 2008 Scientific Party, 2008. High resolution topography of the Rainbow hydrothermal area, Mid-Atlantic Ridge, 36°14′N. *Eos, Transactions American Geophysical Union* 89(53), Fall Meet. Suppl., Abstract T43B-2027.

Gold, T., 1999. *The Deep Hot Biosphere.* Copernicus, New York, 235 pp.

Gràcia, E., Bideau, D., Hekinian, R., Lagabrielle, Y., & Parson, L. M., 1997. Along-axis magmatic oscillations and exposure of ultramafic rocks in a second-order segment of the Mid-Atlantic Ridge (33° 43′N to 34° 07′N). *Geology* 25, 1059–1062.

Gràcia, E., Charlou, J.L., Radford-Knoery, J. & Parson, L., 2000. Non-transform offsets along the Mid-Atlantic Ridge south of the Azores (38°–34°N): Ultramafic exposures and hosting of hydrothermal vents. *Earth and Planetary Science Letters* 177, 89–103.

Grevemeyer, I., Reston, T.J. & Moeller, S., 2013. Microseismicity of the Mid-Atlantic Ridge at 7°S–8°15′S and at the Logatchev Massif oceanic core complex at 14°40′N–14°50′N. *Geochemistry, Geophysics, Geosystems* 14, 3532–3554.

Han, X., Wu, Z. & Qiu, B., 2012. Morphotectonic characteristics of the northern part of the Carlsberg Ridge near the Owen Fracture Zone and the occurrence of oceanic core complex formation. Abstract presented at *AGU Fall Meeting*, San Francisco, USA.

Hellebrand, E., Snow, J.E., Dick, H.J.B. & Hofmann, H., 2001. Coupled major and trace-element indicators in mid-ocean ridge peridotites. *Nature* 410, 677–681.

Hosford, A., Tivey, M. Matsumoto, T., Dick, H.J.B., Schouten, H. & Kinoshita, H., 2003. Crustal magnetization and accretion at the Southwest Indian Ridge near the Atlantis II fracture zone, 0-25 Ma. *Journal of Geophysical Research* 108, 2169.

Ildefonse, B., Andreani, M., Hoise, E., Ballu, V., Escartín, J., Dyment, J. & Fouquet, Y., 2007. Further geological sampling around the Rainbow hydrothermal site, Mid-Atlantic Ridge. *Eos, Transaction American Geophysical Union* 88(52), Fall Meet. Suppl., Abstract T53B-1306.

Jaroslow, G.E., Hirth, G. & Dick, H.J.B., 1996. Abyssal peridotite mylonites: implications for grain-size sensitive flow and strain localization in the oceanic lithosphere. *Tectonophysics* 256, 17–37.

Jousselin, D., Nicolas, A. & Boudier, F., 1998. Detailed mapping of a mantle diapir below a paleo-spreading center in the Oman ophiolite. *Journal of Geophysical Research* 103, 18153–18170.

Jousselin, D., Nicolas, A., Boudier, F. & Meshi, A., 2013. *High-T detachment shear zone in Mirdita ophiolite (Albania)*. Abstract nr T23F-2656 presented at AGU Fall Meetin, San Francisco, USA.

Kamesh Raju, A.K., Samudrala, K., Drolia, R.K., Amarnath, D., Ramachandran, R. & Mudholkar, A., 2012. Segmentation and morphology of the Central Indian Ridge between 3°S and 11°S, Indian Ocean. *Tectonophysics* 554–557, 114–126.

Karson, J.A., Früh-Green, G.L., Kelley, D.S.,Williams, E.A., Yoerger, D.R. & Jakuba, M., 2006. Detachment shear zone of the Atlantis Massif core complex, Mid-Atlantic Ridge, 30°N. *Geochemistry, Geophysics, Geosystems* 7, Q06016.

Karsten, J., Klein, E., Martinesz, F., Mühe, R., Sturm, M., Coleman, T., Hayasaka, J., Jung, D., Murray, G., Muse, B., Newsom, A., Stewart, M., Tougas, S. & Gallegos, J., 1999. The northern Chile Ridge revealed: Preliminary cruise report of PANORAMA Expedition Leg 04. *InterRidge News* 8, 15–21.

Kelemen, P.B., Hirth, G., Shimizu, N., Spiegelman, M. & Dick, H.J.B., 1997. A review of melt migration processes in the asthenospheric mantle beneath oceanic spreading centers. *Philosophical Transactions of the Royal Society* A 355, 283–318.

Kelley, D.S., Karson, J.A., Blackman, D.K., Fruh-Green, G.L., Butterfield, D.A., Lilley, M.D., Olson, E.J., Schrenk, M.O., Roe, K.K., Lebon, G.T. & Rivizzigno, P., 2001. An off-axis hydrothermal vent field near the Mid-Atlantic Ridge at 30°N. *Nature* 412, 145–149.

Klein, E.M., 2003. *Geochemistry of the Igneous Oceanic Crust*. [In:] R.L. Rudnick (Ed.): Treatise on geochemistry. Vol. 3: The Earth's Crust. Elsevier, Amsterdam, 433–463.

Kostitsyn, Yu.A., Silantyev, S.A., Belousova, E.A., Bortnikov, N.S., Krasnova, E.A. & Cannat, M., 2013. Time of the formation of the oceanic core complex of the hydrothermal field in the Mid-Atlantic Ridge (12°58′N): Evidence from zircon study. *Doklady Earth Sciences*, 447, 1301–1305.

Kumagai, H., Nakamura, K., Toki, T., Morishita, T., Okino, K., Ishibashi, J.I., Tsunogai, U., Kawaguchi, S., Gamo, T., Shibuya, T., Sawaguchi, T., Neo, N., Joshima, M., Sato, T. & Takai, K., 2008. Geological background of the Kairei and Edmond hydrothermal fields along the Central Indian Ridge: Implications of their vent fluids' distinct chemistry. *Geofluids* 8, 239–251.

Lagabrielle, Y., Brovarone, A.V. & Ildefonse, B., 2015. Fossil oceanic core complexes recognized in the blue schist metaophiolites of Western Alps and Corsica. *Earth-Science Reviews* 141, 1–26.

Lavier, L.L., Buck, W.R. & Poliakov, A.N.B, 1999. Self-consistent rolling-hinge model for the evolution of large-offset low-angle normal faults. *Geology* 27, 1127–1130.

Macdonald, K.C., Scheirer, D.S. Carbotte, S. & Fox, P.J, 1993. It's only Topography: Part 2. *GSA Today* 3, 29–35.

MacLeod, C.J., Escartín, J., Banerji, D., Banks, G.J., Gleeson, M., Irving, D.H.B., Lilly, R.M., McCaig, A.M., Niu, Y., Allerton, S. & Smith, D.K., 2002. Direct geological evidence for oceanic detachment faulting : The Mid-Atlantic Ridge , 15°45′N. *Geology* 30, 879–882.

MacLeod, C.J., Searle, R.C., Murton, B.J., Casey, J.F., Mallows, C., Unsworth, S.C., Achenbach, K.L. & Harris, M., 2009. Life cycle of oceanic core complexes. *Earth and Planetary Science Letters* 287, 333–344.

MacLeod, C.J., Carlut, J., Escartín, J., Horen, H. & Morris, A., 2011. Quantitative constraint on footwall rotations at the 15°45′N oceanic core complex, Mid-Atlantic Ridge: Implications for oceanic detachment fault processes. *Geochemistry, Geophysics, Geosystems* 12, Q0AG03.

Maffione, M., Morris, A. & Anderson, M.W., 2013. Recognizing detachment-mode seafloor spreading in the deep geological past. *Scientific Reports* 3, 2336.

Mallows, C. & Searle, R.C., 2012. A geophysical study of oceanic core complexes and surrounding terrain, Mid-Atlantic Ridge 13°N–14°N. *Geochemistry, Geophysics, Geosystems* 13, Q0AG08.

Manatschal, G., Sauter, D., Karpoff, A.M., Masini, E., Mohn, G. & Lagabrielle, Y., 2011. The Chenaillet ophiolite in the French/Italian Alps: an ancient analogue for an oceanic core complex? *Lithos* 124, 169–184.

Martinez, F. & Taylor, B., 2002. Mantle wedge control on back-arc crustal accretion. *Nature* 416, 417–420.

Marty, B. & Yokochi, R., 2006. Water in the Early Earth. *Review in Mineralogy & Geochemistry* 62, 421–450.

McCaig, A., 2010. *Hydrothermal Systems and Detachment Faulting*. Abstract presented at AGU Chapman Conference, Agros, Cyprus.

McCaig, A.M., Cliff, B., Escartín, J., Fallick, A.E. & MacLeod, C.J., 2007. Oceanic detachment faults focus very large volumes of black smoker fluids. *Geology* 35, 935–938.

McCollom, T.M. & Seewald, J.S., 2013. Serpentinites, Hydrogen, and Life. *Elements* 9, 129–134.

Ménez B, Pasini V. & Brunelli, D., 2012. Life in the hydrated suboceanic mantle. *Nature Geoscience* 5,133–137.

Mével, C., Agrinier, P., Cannat, M., Decitre, S., Dappoigny, A., Humler, E., Jendrzejewski, N., Kienast, J.R., Ludden, J., Murton, B., Oufi, O., Rabain, A., Seyler, M. & Tamura, Y., 1997. Sampling the South West Indian Ridge: first results of the EDUL cruise (R/V Marion Dufresne II, August 1997). *InterRidge News* 6, 25–26.

Miller, D.J. & Christensen, N.I, 1997. Seismic velocities of lower crustal and upper mantle rocks from the slow spreading Mid-Atlantic Ridge, south of the Kane transform zone (MARK). [In:] J.A. Karson, M. Cannat, D.J. Miller & D. Elthon (Eds): *Proceedings of the Ocean Drilling Program, Scientific Results* 153, 437–454.

Miranda, J.M., Silva, P.F., Lourenço, N., Henry, B., Costa, R. & Team, S., 2002. Study of the Saldanha massif (MAR, 36º34′N): Constrains from rock magnetic and geophysical data. *Marine Geophysical Research* 23, 299–318.

Mitchell, N., Escartín, J. & Allerton, S., 1998. Detachment Faults at Mid-Ocean Ridges Garner Interest. *Eos, Transaction American Geophysical Union* 79, 127.

Morishita, T., Hara, K., Nakamura, K., Sawaguchi, T., Tamura, A., Arai, S., Okino, K., Takai, K. & Kumagai, H., 2009. Igneous, alteration and exhumation processes recorded in abyssal peridotites and related fault rocks from an oceanic core complex along the Central Indian Ridge. *Journal of Petrology* 50, 1299–1325.

Morris, J.D. & Ryan, J.G., 2003. *Subduction zone processes and implications for changing composition of the upper and lower mantle*. [In:] R.W. Carlson (Ed.): Treatise on geochemistry. Vol. 2: The Mantle and Core. Elsevier, Amsterdam, 451–470.

Mudholkar, A., Kamesh Raju, K.A., Babu, E.V.S.S.K., Sreenivas, B., Vijaya Kumar, T. & Bhaskar Rao, Y.J., 2012. Oceanic core complexes along Carlsberg Ridge. *International Conference: Ridges and Hotspots around the Mascarene Islands*, LUX Island resort, Mauritius.

Nakamura, K., Morishita, T., Bach, W., Klein, F., Hara, K., Okino, K., Takai, K. & Kumagai, H., 2009. Serpentinized olivine-rich gabbroic rocks exposed near the Kairei Hydrothermal Field, Central Indian Ridge: Insights into the origin of the Kairei hydrothermal fluid supporting a unique microbial ecosystem. *Earth and Planetary Science Letters* 280, 128–136.

Nicolas, A., Boudier, F. & Meshi, A., 1999. Slow spreading accretion and mantle denudation in the Miridita ophiolite (Albania). *Journal of Geophysical Research* 104, 15155–15167.

Niu, Y. & Batiza, R., 1994. Magmatic processes at a slow spreading ridge segment: 26°S Mid-Atlantic Ridge, *Journal of Geophysical Research* 99, 19719–19740.

Nuriel, P., Katzir, Y., Abelson, M., Valley, J.W., Matthews, A., Spicuzza, M.J. & Ayalon, A., 2009. Fault-related oceanic serpentinization in the Troodos ophiolite, Cyprus: Implications for a fossil oceanic core complex. *Earth and Planetary Science Letters* 282, 34–46.

Ohara, Y., Yoshida, T., Kato, Y. & Kasuga, S., 2001.Giant megamullion in the Parece Vela backarc basin. *Marine Geophysical Researches* 22, 47–61.

Ohara, Y., Okino, K., Snow, J.E. & KR03-01 Shipboard Scientific Party, 2003a. Preliminary report of Kairei KR03-01 cruise: amagmatic tectonics and lithospheric composition of the Parece Vela Basin. *Interridge News* 12, 27–29.

Ohara, Y., Fujioka, K., Ishii, T. & Yurimoto, H., 2003b. Peridotites and gabbros from the Parece Vela backarc basin: unique tectonic window in an extinct backarc spreading ridge. *Geochemistry, Geophysics, Geosystems* 4, 8611.

Okino, K., Matsuda, K., Christie, D.M., Nogi, Y. & Koizumi, K., 2004. Development of oceanic detachment and asymmetric spreading at the Australian-Antarctic Discordance. *Geochemistry, Geophysics, Geosystems* 5, Q12012.

Palmer, J., Sempere, J.-C., Christie, D.M. & Morgan, J.P., 1993. Morphology and tectonics of the Australian-Antarctic Discordance between 123°E and 128°E. *Marine Geophysical Researches* 15, 121–152.

Palmiotto, C., Corda, L., Ligi, M., Cipriani, A., Dick, H. J.B., Douville, E., Gasperini, L., Montagna, P., Thil, F., Bosetti, A.M., Balestra, B. & Bonatti, E., 2013. Nonvolcanic tectonic islands in ancient and modern oceans. *Geochemistry, Geophysics, Geosystems* 14, 4698–4717.

Parkinson, I.J. & Pearce, J.A., 1998. Peridotites from the Izu-Bonin-Mariana Forearc (ODP Leg 125): evidence for mantle melting and melt-mantle interaction in a supra-subduction zone setting. *Journal of Petrology* 39, 1577–1618.

Pearson, D.G., Canil, D. & Shirey, S.B., 2003. *Mantle Samples Included in Volcanic Rocks: Xenoliths and Diamonds*. [In:] R.W. Carlson (Ed.): Treatise on geochemistry. Vol. 2: The Mantle and Core. Elsevier, Amsterdam, 171–275.

Penrose Conference Participants, 1972. Penrose Field Conference: Ophiolites. *Geotimes* 17, 24–25.

Petersen, S., Kuhn, K., Kuhn, T., Augustin, N., Hekinian, R., Franz L. & Borowski, C., 2009. The geological setting of the ultramafic-hosted Logatchev hydrothermal field (14°45'N, Mid-Atlantic Ridge) and its influence on massive sulfide formation. *Lithos* 112, 40–56.

Planert, L., Flueh, E.R., Tilmann, F., Grevemeyer, I. & Reston, T.J., 2010. Crustal structure of a rifted oceanic core complex and its conjugate side at the MAR at 5°S: Implications for melt extraction during detachment faulting and core complex formation. *Geophysical Journal International* 181, 113–126.

Pyle, D.G., 1993. *Geochemistry of mid-ocean ridge basalt within and surrounding the Australian Antarctic Discordance*. Ph.D. thesis. Oregon State University, 178 pp.

Pyle, D.G., Christie, D.M. & Mahoney, J.J., 1992. Resolving an isotope boundary within the Australian-Antarctic Discordance. *Earth and Planetary Science Letters* 112, 161–178.

Rampone, E., Piccardo, G. B., Vannucci, R. & Bottazzi, P., 1997. Chemistry and origin of trapped melts in ophiolitic peridotites. *Geochimica et Cosmochimica Acta* 41, 4557–4569.

Ranero, C.R. & Reston, T.J., 1999. Detachment faulting at ocean core complexes. *Geology* 27, 983–986.

Reston, T.J., Weinrebe, W., Grevemeyer, I., Flueh, E.R., Mitchell, N.C., Kirstein, L., Kopp, C. & Kopp, H., 2002. A rifted inside corner massif on the Mid-Atlantic Ridge at 5°S. *Earth and Planetary Science Letters* 200, 255–269.

Reston, T.J., Ranero, C.R., Ruoff, O., Perez-Gussinye, M. & Danobeitia, J.J., 2004. Geometry of extensional faults developed at slow-spreading centres from seismic reflection data in the Central Atlantic (Canary Basin). *Geophysical Journal International* 159, 591–606.

Reves-Sohn, R. & Humphris, S., 2004. *Seismicity and fluid flow of the TAG Hydrothermal Mound-4: Cruise report, STAG Leg 4*. Woods Hole Oceanographic Institution, Woods Hole, Massachusetts, 36 pp.

Ribeiro Da Costa, I., Barriga, F.J., Viti, C., Mellini, M. & Wicks, F.J., 2008. Antigorite in deformed serpentinites from the Mid-Atlantic Ridge. *European Journal of Mineralogy* 20, 563–572.

Sato, T., Okino, K. & Kumagai, H. 2009. Magnetic structure of an oceanic core complex at the southernmost Central Indian Ridge: Analysis of shipboard and deep-sea three-component magnetometer data. *Geochemistry, Geophysics, Geosystems*, 10, Q06003.

Schroeder, T. & John, B.E., 2004. Strain localization on an oceanic detachment fault system, Atlantis Massif, 30°N, Mid-Atlantic Ridge. *Geochemistry, Geophysics, Geosystems* 5, Q06015.

Schroeder, T., Cheadle, M.J., Dick, H.J.B., Faul, U., Casey, J.F. & Kelemen, P.B., 2007. Nonvolcanic seafloor spreading and corner-flow rotation accommodated by extensional faulting at 15°N on the Mid-Atlantic Ridge: A structural synthesis of ODP Leg 209. *Geochemistry, Geophysics, Geosystems* 8, Q06015.

Scott, H.P., Hemley, R.J., Mao, H.K., Herschbach, D.R., Fried, L.E., Howard, W.M. & Bastea, S., 2004. Generation of methane in the Earth's mantle: In situ high pressure-temperature measurements of carbonate reduction. *Proceedings of the National Academy of Sciences* 101, 14023–14026.

Searle, R.C. & Bralee, A.V, 2007. Asymmetric generation of oceanic crust at the ultra-slow spreading Southwest Indian Ridge, 64°E, *Geochemistry, Geophysics, Geosystems* 8, Q015015.

Searle, R.C., Cannat, M., Fujioka, K., Mével, C., Fujimoto, H., Bralee, A. & Parson, L., 2003. FUJI Dome: A large detachment fault near 64°E on the very slow-spread-

ing southwest Indian Ridge. *Geochemistry, Geophysics, Geosystems* 4, 9105.

Shipboard Scientific Party, 2003. *Leg 209 Preliminary Report.* Ocean Drilling Program, College Station, Texas, 100 pp.

Shipboard Scientific Party, 2005a. *Expedition 304 Preliminary Report: Oceanic Core Complex Formation, Atlantis Massif*. Integrated Ocean Drill. Program, College Station, Texas, 63 pp.

Shipboard Scientific Party, 2005b. *Expedition 305 Preliminary Report: Oceanic Core Complex Formation, Atlantis Massif*. Integrated Ocean Drill. Program, College Station, Texas, 78 pp.

Skinner, B.J., Porter, S.C. & Park, J., 2004. *Dynamic Earth: An Introduction to Physical Geology*. John Wiley, New Jersey, 630 pp.

Silantyev, S.A., Mironenko, M.V. & Novoselov, A.A., 2009a. Hydrothermal systems in peridotites of slow-spreading mid-oceanic ridges. Modeling phase transitions and material balance: Downwelling limb of a hydrothermal circulation cell. *Petrology*, 17, 138–157.

Silantyev, S.A., Mironenko, M.V. & Novoselov, A.A, 2009b. Hydrothermal systems hosted in peridotites at slow-spreading ridges. Modeling phase transformations and material balance: Upwelling limb of the hydrothermal cell. *Petrology*, 17, 523–536.

Smith, D.K., Cann, J.R. & Escartín, J., 2006. Widespread active detachment faulting and core complex formation near 13° N on the Mid-Atlantic Ridge. *Nature* 442, 440–443.

Smith, D.K., Escartín, J., Schouten, H. & Cann, J.R., 2008. Fault rotation and core complex formation: Significant processes in seafloor formation at slow-spreading mid-ocean ridges (Mid-Atlantic Ridge, 13°–15°N). *Geochemistry, Geophysics, Geosystems* 9, Q03003.

Smith, D.K., Escartín, J., Schouten, H. & Cann, J.R., 2012. Active long-lived faults emerging along slow-spreading mid-ocean ridges. *Oceanography* 25, 94–99.

Smith, D.K., Schouten, H., Dick, H.J.B., Cann, J.R., Salters, V., Marschall, H.R., Ji, F., Yoerger, D., Sanfilippo, A., Parnell-Turner, R., Palmiotto, C., Zheleznov, A., Bai, H., Junkin, W., Urann, B., Dick, S., Sulanowska, M., Lemmond, P. & Curry, S., 2014. Development and evolution of detachment faulting at 50 km of the Mid-Atlantic Ridge near 16.5°N. *Geochemistry, Geophysics, Geosystems* 15, 4692–4711.

Solomon, S.C., Huang, P.Y. & Meinke, L., 1988. The seismic moment budget of slowly spreading ridges. *Nature* 334, 58–60.

Suhr, G., Hellebrand, E., Johnson, K. & Brunelli, D., 2008. Stacked gabbro units and intervening mantle: A detailed look at a section of IODP Leg 305, Hole U1309D. *Geochemistry, Geophysics, Geosystems* 9, Q10007.

Tamura, A., Arai, S., Ishimaru, S. & Andal, E.S., 2008. Petrology and geochemistry of peridotites from IODP Site U1309 at Atlantis Massif, MAR 30°N: micro- and macro-scale melt penetrations into peridotites. *Contributions to Mineralogy and Petrology* 155, 491–509.

Tebbens, S.F., Cande, S.C., Kovacs, L., Parra, J.C., LaBrecque, J.L. & Vergara, H., 1997. The Chile ridge: A tectonic framework. *Journal of Geophysical Research* 102, 12035–12059.

Thatcher, W. & Hill, D.P., 1995. A simple model for fault generated morphology of slow-spreading mid-oceanic ridges. *Journal of Geophysical Research* 100, 561−570.

Tivey, M.A., Schouten, H. & Kleinrock, M.C. 2003. A near-bottom magnetic survey of the Mid-Atlantic Ridge axis at 26°N: Implications for the tectonic evolution of the TAG segment. *Journal of Geophysical Research* 108, 2277.

Tremblay, A., Meshi, A. & Bedard, J.H., 2009. Oceanic core complexes and ancient oceanic lithosphere: Insight from Iapetan and Tethyan ophiolites (Canada and Albania). *Tectonophysics* 473, 36–52.

Tucholke, B.E. & Lin, J., 1994. A geological model for the structure of ridge segments in slow spreading ocean crust. *Journal of Geophysical Research* 99, 11937–11958.

Tucholke, B.E., Lin, J. & Kleinrock, M.C., 1996. Mullions, megamullions, and metamorphic core complexes on the Mid-Atlantic Ridge. *Eos, Transaction American Geophysical Union* 77(46), Fall Meet. Suppl., Abstract F724.

Tucholke, B.E., Lin, J., Kleinrock, M.C., Tivey, M.A., Reed, T.B., Golf, J. & Jaroslow, G.E., 1997. Segmentation and crustal structure of the western Mid-Atlantic Ridge flank, 25°25′–27°10′N and 0–29 m.y. *Journal of Geophysical Research* 102, 203–223.

Tucholke, B.E., Lin, J. & Kleinrock, M.C., 1998. Megamullions and mullion structure defining oceanic metamorphic core complexes on the mid-Atlantic ridge. *Journal of Geophysical Research* 103, 9857–9866.

Tucholke, B.E., Fujioka, K., Ishihara, T., Hirth, G., & Kinoshita, M., 2001. Submersible study of an oceanic megamullion in the central North Atlantic. *Journal of Geophysical Research* 106, 145–161.

Tucholke, B.E., Behn, M.D., Buck, R. & Lin, J., 2008. The role of melt supply in oceanic detachment faulting and formation of megamullions. *Geology* 36, 455–458.

Tucholke, B.E., Humphris, S.E. & Dick, H.J.B., 2013. Cemented mounds and hydrothermal sediments on the detachment surface at Kane Megamullion: A new manifestation of hydrothermal venting. *Geochemistry, Geophysics, Geosystems* 14, 3352–3378.

Wang, W., Chu, F., Zhu, J., Dong, Y., Yu, X., Chen, L. & Li, Z., 2013. Mantle melting beneath the Southwest Indian Ridge: signals from clinopyroxene in abyssal peridotites. *Acta Oceanologica Sinica* 32, 50–59.

White, R.S., McKenzie, D. & O'Nions, R.K., 1992. Oceanic crustal thickness from seismic measurements and rare earth element inversions. *Journal of Geophysical Research* 97, 19683–19715.

Whitney, D.L., Teyssier, C., Rey, P.F. & Buck, W.R., 2013. Continental and oceanic core complexes. *Geological Society of America Bulletin* 125, 273–298.

Wilkinson, J.F.G., 1986. Classification and average chemical compositions of common basalts and andesites. *Journal of Petrology* 27, 31–62.

Wilson, M., 1997. *Igneous Petrogenesis*. Springer, Dordrecht, 466 pp.

Wilson, S., 2010. *Mantle source composition beneath Mid Atlantic Ridge: controls on the development of e-MORB segment and oceanic core complexes*. School of Ocean and

Earth Sciences, University of Southampton, PhD thesis, 392 pp.

Xu, M., Canales, J.P., Tucholke, B.E. & DuBois, D.L., 2009. Heterogeneous seismic velocity structure of the upper lithosphere at Kane oceanic core complex, Mid-Atlantic Ridge. *Geochemistry, Geophysics, Geosystems* 10, Q10001.

Yi, S.B., Oh, C.W., Pak, S.J., Kim, J., & Moon, J.W., 2014. Geochemistry and petrogenesis of mafic-ultramafic rocks from the Central Indian Ridge, latitude 8°–17° S: denudation of mantle harzburgites and gabbroic rocks and compositional variation of basalts. *International Geology Review* 56, 1691–1719.

Yu, Z., Li, J., Liang, Y., Han, X., Zhang, J. & Zhu, L., 2013. Distribution of large-scale detachment faults on mid-ocean ridges in relation to spreading rates. *Acta Oceanologica Sinica*, 12, 109–117.

Zhao, M., Canales, J.P. & Sohn, R.A., 2012. Three-dimensional seismic structure of a Mid-Atlantic Ridge segment characterized by active detachment faulting (Trans-Atlantic Geotraverse, 25°55′N–26°20′N). *Geochemistry, Geophysics, Geosystems* 13, Q0AG13.

Zhao, M., Qui, X., Li, J., Sauter, D., Ruan, A., Chen, J., Cannat, M., Singh, S., Zhang, J., Wu, Z. & Niu, X, 2013. Three-dimensional seismic structure of the Dragon Flag oceanic core complex at the ultraslow spreading Southwest Indian Ridge (49°39′E). *Geochemistry, Geophysics, Geosystems* 14, 4544–4563.

Zhou, H., 2015. Regional geology of active Dragon Hydrothermal Field, Southwest Indian Ridge. *IODP workshop: Indian ocean crust & mantle drilling*, Woods Hole, MA, USA, May 13–16, 2015.

Zhou, H. & Dick, H.J.B., 2013. Thin crust as evidence for depleted mantle supporting the Marion Rise. *Nature* 494, 195–200.

Zonenshain, L.P., Kuzmin, M.I., Lisitsin, A.P., Bogdanov, Y.A. & Baranov, B.V., 1989. Tectonics of the Mid-Atlantic rift valley between the TAG and MARK areas (26–24°N): evidence for vertical tectonism. *Tectonophysics* 159, 1–23.

Manuscript received: 15 December 2014
Revision accepted: 13 June 2015

Sulfide-oxide fractional crystallization controls metal transport through a slow-spread lower oceanic crust with a high magma supply: IODP Hole U1473A

Jakub Ciazela[1,2*], Juergen Koepke[1], Harald Strauss[3], Bartosz Pieterek[2], Henry J.B. Dick[4], Andrzej Muszynski[2], Thomas Kuhn[5], Marcel Bender[1], Andreas Stracke[6]

[1] *Institut für Mineralogie, Leibniz Universität Hannover, Callinstr. 3, 30167 Hannover, Germany*

[2] *Institute of Geology, Adam Mickiewicz University, ul. Bogumiła Krygowskiego 12, 61-680 Poznań, Poland*

[3] *Institut für Geologie und Paläontologie - Historische und Regionale Geologie, Westfälische Wilhelms-Universität Münster, Corrensstr. 24, D-48149 Münster, Germany*

[4] *Department of Geology and Geophysics, Woods Hole Oceanographic Institution, MS #8, McLean Laboratory, Woods Hole MA 02543-1539, USA*

[5] *Bundesanstalt für Geowissenschaften und Rohstoffe, Stilleweg 2, 30655 Hannover, Germany.*

[6] *Institut für Geologie und Paläontologie - Historische und Regionale Geologie, Westfälische Wilhelms-Universität Münster, Corrensstr. 24, D-48149 Münster, Germany*

** corresponding author: j.ciazela@mineralogie.uni-hannover.de, phone: +49 511 762 2322, fax: +49 511 762 3045*

KEYWORDS*:*

Oceanic lower crust, sulfide, oxide, fractional crystallization, IODP, seafloor massive sulfide

ABSTRACT:

Primary and secondary transport of chalcophile metals through the oceanic lithosphere control the formation of seafloor massive sulfide (SMS) deposits. Although, chalcophile elements have been investigated in the upper oceanic crust, little work has thoroughly examined their migration through the lower oceanic crust due to scarcity of drilled material. In 2016, International Ocean Discovery Program (IODP) Expedition 360 drilled the 810-m-deep U1473A hole into the gabbroic lower crust of the Atlantis Bank ocean core complex (OCC) at the Southwest Indian Ridge (SWIR; 32°42’S, 57°17’E). We selected 101 evenly distributed samples

representing the range of rocks in the drill hole to analyze their metal and S contents along with the S and Sr isotopes. Sulfides throughout the hole are almost exclusively pyrrhotite-chalcopyrite-pentlandite grains. This paragenesis along with a consistent trace element composition throughout the hole as well as the mantle-derived S and Sr isotope signatures indicate the predominant role of magmatic processes in the transport of chalcophile metals. Downhole Cu, S, Fe_2O_3, MnO, Co and P_2O_5 upward-decreasing trends matching Mg-number trends and shipboard-defined magmatic units suggest dominant role of fractional crystallization. Sulfide are closely associated with oxides and we observe high correlation coefficients between S, MnO, TiO_2, and Fe_2O_3. Based on textural features, we show that oxides crystallize first immediately followed by sulfides. The crystallization of sulfides after oxides is achieved by lowering the level of sulfide concentration at sulfide saturation (SCSS) in the portion of melt suffered by loss of iron and decreased oxygen fugacity after oxide precipitation. As sulfides and oxides fractionate early they tend to accumulate at the lower part of gabbroic bodies, which are by ~50% enriched in Cu and by ~100% enriched in S with respect to the upper parts. In addition, gabbro bodies located deeper in the crust are enriched in metals with respect to shallower gabbro bodies. Deep position of sulfide-rich interval in the stratigraphic column hampers their penetration by hydrothermal fluids, and may be the reason why SMS deposits have not been found at Atlantis Bank although they are common in OCCs.

1. INTRODUCTION

Sulfide ores on land are plummeting due to the high demand of the industry. Shrinking on-shore resources have led to combing the ocean floor (Boschen et al., 2013; Hoagland et al., 2010). The average Cu grade of seafloor massive sulfide (SMS) deposits is from 2 to 25 times higher than the average Cu grade of active land-based mines (Hein et al., 2013). Therefore, chalcophile element transport through the oceanic crust has been of major scientific interest in the last three decades.

Chalcophile elements have been investigated in the holes drilled into the upper fast-spread oceanic crust (Alt et al., 2010, 1989; Bach et al., 2003). However, SMS deposits preferentially occur along the slow-spreading ridges (86%) with respect to intermediate spreading ridges (12%) and fast-spreading ridges (2%) (Hannington et al., 2011). This is also reflected in the distribution of International Seabed Authority (ISA) sulfide exploration areas. Among seven ISA contractors,

China, Russia, France, and Poland operate on ultra-slow and slow-spreading ridge sections with Korea, Germany, and India operating on slow-to-intermediate-spreading ridge sections. In addition, the SMS deposits with the highest metal grades occur on top of oceanic core complexes (OCC) (Hannington et al., 2010). OCCs are exposures of the lower crust and mantle moved to the seafloor along detachment faults, which occur along the ultraslow-to-intermediate spreading ridges. The plutonic rocks may thus be a key to understand magmatic processes crucial for metal-rich SMS deposits.

Although several important studies have been dedicated to sulfides (Miller and Cervantes, 2002; Natland et al., 1991) and sulfur (Alt and Anderson, 1991; Bach et al., 2001; Delacour et al., 2008) in the slow-spread oceanic lower crust, the scarcity of available material has not fully allowed to thoroughly examine the transport of chalcophile and siderophile metals. As a result, the source and processes leading to the formation of large SMS deposits on top of the slow-spread oceanic crust are yet not fully understood. The character of magmatic processes at the slow-spread lithosphere may depend on the rate of local magma supply (Ciazela et al., 2015). Recently, we studied how magmatic processes control metal migration in a slow-spread lower oceanic lithosphere with low magma supply, and highlighted the crucial role of melt-mantle reaction in there (Ciazela et al., 2017). To study metal transport at a slow-spread oceanic lithosphere with a high magma supply three of us took part in the International Ocean Discovery Program (IODP) Expedition 360, which drilled the 810-m-deep U1473A hole into the gabbroic lower crust of the Atlantis Bank OCC at the Southwest Indian Ridge (SWIR). We selected 101 evenly distributed samples representing the range of rocks in the drill hole to analyze their metal and S contents and S isotopes. This study allowed us to demonstrate a high role of magmatic transport with limited role of hydrothermal transport in the lower oceanic crust. In addition, we have shown that fractional crystallization is a principal mechanism of sulfide and oxide differentiation in the local crust.

2. GEOLOGICAL SETTING AND SAMPLE COLLECTION

2.1. Geological setting

The Atlantis Bank is a well-studied OCC (Dick et al., 2015 and references therein) located at ~100 km south of the axial valley of the ultraslow-spreading section of SWIR (32°40′ S and 57°15′ E) and close to the Atlantis II Transform fault. The bank consists of a raised dome about

40 by 30 km in size, and rising from 5700 m water depth at the base of the transform wall to about 750 m on a ~25 km^2 large flat-topped platform (Fig. 1). The platform is part of a continuous gabbro massif, which was emplaced ~12 Myr ago (Baines et al., 2009) and is exposed throughout the dome. Gabbro overlies granular mantle peridotite that forms the lower slopes of the eastern wall of the Atlantis II Transform. Mapping shows that the basement on the wave-cut platform largely consists of shallow dipping gabbro mylonite generated by detachment faulting (Dick et al., 2015). The predominance of gabbro in the platform basement has been confirmed by four IODP expeditions during which three holes have been drilled (Fig. 1), including the 1508-m deep but inactive Hole 735B from 1997 (Dick et al., 2000).

2.2. Sample Collection

Expedition 360, which was finished in January 2016, drilled 2 km northeast from 735B resulting in the 789-m deep Hole U1473A (Dick et al., 2016). In July 2016, the hole was cleaned, deepened to 810 m and reinforced with cement to maintain the hole in good condition before the next scientific expedition (MacLeod et al., 2017). The ultimate goal is to drill through the crust-mantle boundary (Ciazela et al., 2016; Dick et al., 2016; MacLeod et al., 2017). Preliminary assessment of the drilled lithology indicates repeated intrusions of the ~300-m scale olivine gabbro (76.5 vol.% of the recovered rocks) and gabbro (14.6 vol.%) cumulate into the crust. Minor oxide gabbro layers and patches (7.4 vol.%) occur within the olivine gabbro (Dick et al., 2016). Gabbroic rocks are occasionally cut by felsic veins (remaining 1.5 vol.%). A highly fractured carbonate cemented zone has been encountered between 170 and 570 mbsf with a recovery rate of 44%. This zone likely represents a system of late high-angle normal faults. Below 570 mbsf, drilling conditions were excellent with a 96% recovery (Dick et al., 2016). A total of 97 gabbroic samples and 4 felsic veins have been selected for whole-rock analyses in this study (Fig. 2). The samples are distributed in relatively equal intervals to provide a representative downhole profile. However, the bottom part of the hole where most sulfides occurred has been sampled more densely (Fig. 2). Gabbroic samples are typically 150-200 g large, 1 cm thick, 6 cm wide, and 10 cm long slabs cut out from the core.

3. METHODS

3.1. Major elements

Major elements (Table S1 Supplementary Material) were determined using X-ray Fluorescence (XRF) spectroscopy at the Bundesanstalt für Geowissenschaften and Rohstoffe, Hannover, Germany. To form tablets for the analyses, 1 g of sample powder and 5 g $LiBO_2$ were mixed and melted for 20 minutes at 1200°C. The tablets were analyzed with a wavelength dispersive PANalytical AXIOS X-ray spectrometer equipped with a Rh X-ray tube. To calibrate the XRF measurements, several international standards were used. The relative uncertainty is between 1 and 2%. Loss-on-ignition (LOI) method was used to determine the total volatile concentrations. To evaporate volatiles, samples were heated in a muffle furnace at 1030°C for 10 min.

3.2. Trace elements

Trace elements (Table S2 Supplementary Material) were determined with Instrumental Neutron Activation Analysis (INAA) and Inductively Coupled Plasma Mass Spectrometry (ICPMS) at the Activation Laboratories Ltd., Ontario, Canada with the Ultratrace 5 package (see the Ultratrace 5 - Total Digestion - ICPMS, INAA subsection of the Methods section of the Actlab website www.actlabs.com for detailed description). For the ICPMS analysis, 0.25 g per sample were digested in a sequence of four acids (perchloric, hydrofluoric, hydrochloric and nitric). For INAA measurements, 30 g of sample powder were used to minimize nugget effect for Au. The powders were encapsulated in polyethylene vials. Samples and internal standards were irradiated with flux wires at a thermal neutron flux of 7×10^{12} n $cm^{-2}s^{-1}$. After seven days needed for ^{24}Na decay, elemental concentrations in samples were counted on a high purity Ge detector.

3.3. Sulfur concentrations

ELTRA CS 800 (Institut für Mineralogie, Leibniz Universität Hannover) and CS 580 (Institut für Geologie und Paläontologie, Westfalische Wilhelm Universität Münster) carbon/sulfur Analyzers were used to determine the sulfur concentrations (Table S3 Supplementary Material). Sample powders (60 to 150 mg) were placed in a porcelain crucible, combusted in an O_2-atmosphere at 1350°C, and detected using infrared. Detailed analytical procedure is provided by Lissner et al. (2014).

3.4. Sulfur isotopes

Sulfur extraction and isotopic analyses were carried out at the Institut für Geologie und Paläontologie, Westfalische Wilhelm Universität Münster, Germany. Acid volatile sulfides (AVS) and Cr-reducible sulfur (CRS) were sequentially or together (Table S3 Supplementary Material) extracted to Ag_2S using a modified method of Canfield et al. (1986). The $^{34}S/^{32}S$ ratios are reported as $\delta^{34}S$ related to Vienna Canyon Diablo Troilite (V-CDT) and measured using a Thermo Finnigan Delta Plus MS. IAEA-S1, IAEA-S2, IAEA-S3 and NBS 127 were used as reference materials. To determine the $\Delta^{33}S$, defined as $\ln(\delta^{33}S + 1) - 0.515 \times \ln(\delta^{34}S + 1)$, and $\Delta^{36}S$, defined as $\ln(\delta^{36}S + 1) - 1.90 \times \ln(\delta^{34}S + 1)$ (Ono et al., 2012), multiple sulfur isotopes (32, 33, 34, 36) were measured using a ThermoScientific Mat 253 MS. For this scope, the Ag_2S's were at first fluorinated in Ni reactors at 300 °C to form SF_6, which were then cryogenically and chromatographically purified, and introduced to the MS. IAEA-S1 was used as a reference material. The $\delta^{34}S$ obtained by this method match well the $\delta^{34}S$ values obtained with the Thermo Finnigan Delta Plus MS (Fig. S1 Supplementary Material). In all these cases where $\delta^{34}S$ values are obtained by both methods (Table S3 Supplementary Material), the averages of the two are plotted (Fig. 3).

3.5. Strontium isotopes

Strontium digestion, separation and analysis were carried at Institut für Mineralogie, Westfalische Wilhelm Universität Münster, Germany. At first, 50 mg of fine powder were digested with HF-HNO_3 followed by HCl. Strontium was separated by using standard cation exchange procedures, loaded on W filaments, and measured on a Finnigan-Mat Triton multicollector MS. The NBS 987 standard measured along with the samples gave $^{87}Sr/^{86}Sr$ 0.710234±7 (2 SD; n=7) during the measurement period, which agrees well with the long-term reproducibility of 0.710240.

4. RESULTS

4.1. Petrographic characteristic of sulfide and oxide assemblages

Sulfides occur almost exclusively as polysulfide grains (Fig. 4) composed of pyrrhotite (~80 vol.%), chalcopyrite (~15 vol.%), and pentlandite (~5 vol.%). This proportion is rather consistent throughout the hole although the abundance of pentlandite varies from ~10 vol.% at the bottom of the hole to ~2-3 vol.% at the top. Pentlandite generally occur as small crystals dispersed

throughout the pyrrhotite, whereas most of the chalcopyrite form massive crystals, often on the rims of the pyrrhotite (Fig. 4b). Exsolutions of pentlandite in pyrrhotite imply they formed from a monosulfides solid solution upon cooling. Exsolutions of troilite in the pyrrhotite (Fig. 4c) are also observed throughout the hole. Some of the sulfides form up to 200 μm large globules, which are often enclosed in clinopyroxene (Fig. 4a). In addition, we found associated inclusions of clinopyroxene in the pyrrhotite. The sulfides typically occur with more abundant Fe-Ti oxides. These are titanomagnetites or exsolutions of titanomagnetite and ilmenite (Fig. 4a). Sulfides are usually fresh or slightly weathered. Only in Sample 9R-3 116/123 (74.8 mbsf) we found pyrite partially replacing pyrrhotite.

4.2. Bulk-rock compositions

Our gabbroic rocks are on average slightly less altered than all the U1473A rocks (Fig. S2 Supplementary Material). They are slightly (3-9%, rank 1) to moderately (10-29%, rank 2) altered with an average rank of 1.6 (Table S4 Supplementary Material). Our felsic veins are extensively (rank 4, 60-89%) to completely (5, ≥90%) completely with an average rank of 4.7. The gabbroic rocks always contain olivine, and are mostly classified as olivine gabbro (>5% modal olivine, Table S4 Supplementary Material). This is reflected in their high Mg-number (72) and low SiO_2 content (50.2 wt%; Table S1 Supplementary Material). A low average LOI of 0.5 wt% confirms low alteration intensity (Table S1 Supplementary Material). Felsic veins are more evolved with an average Mg-number of 62 and an average SiO_2 content of 68.0 wt%. Higher average LOI (1.1 wt%) of felsic veins is consistent with their stronger alteration (Table S1 Supplementary Material).

Felsic veins are on average depleted in major (1.7 wt% Fe_2O_3, 0.19 wt% TiO_2, 0.03 wt% MnO; Table S1 Supplementary Material) and trace siderophile and chalcophile metals (63 ppm Cu, 27 ppm Zn, 29 ppm Co; Table S2 Supplementary Material) with respect to gabbroic rocks (7.3 wt% Fe_2O_3, 0.67 wt% TiO_2, 0.13 wt% MnO; 84 ppm Cu, 46 ppm Zn, 49 ppm Co; Tables S1-2 Supplementary Material). In gabbroic rocks, metal concentrations decrease upwards the hole. This is the case both for chalcophile (Figs. 3, 5 and 6a) and siderophile elements (Fig. 6a-c). The metal concentrations drop not linearly but in discrete intervals, which boundaries correspond to the large-scale (Fig. 5) or medium-scale gabbroic bodies (cf. Figs. 2 and 6). The Cu and S concentrations scatter but seem to follow the general large-scale igneous differentiation

trends defined by Mg-number (Fig. 5). Cu and S decrease from ~110 to ~50 ppm, and from ~900 to ~450 ppm, respectively in the lower large-scale gabbroic body (Fig. 5). At ~300 mbsf, the upper large-scale gabbroic body starts, which contains ~100 ppm Cu and 950 ppm S at its bottom and only ~55 ppm Cu and ~400 ppm S at its top. Interestingly these trends for sulfide-related elements are mirrored by the apatite-related P_2O_5 (Fig. 6d). Siderophile elements, which scatter less then chalcophile elements, allow for their correlations also with medium-scale gabbroic bodies distinguished in Fig. 2. For example, the bottom Unit VIII is characterized by decreasing concentrations of Co, MnO and Fe_2O_3 from ~50 ppm, ~0.12 wt%, and ~6.5 wt% to ~40 ppm, 0.10 wt%, and 5.2 wt%, respectively. Similar decreasing trends are clear for the following Units VII, VI, and V but not obvious for Units IV to I, which were less densely sampled.

The correlation matrix (Table S5 Supplementary Material) of various major and trace elements reveals high correlations between sulfide-related (S, Cu, Pb, Ag, Co, Zn, Fe_2O_3), oxide-related (Fe_2O_3, TiO_2, MnO, Zn, Co, Ga, V), and apatite-related elements (P_2O_5), whereas correlation is scares in other cases. One major exception is Ni; although being often chalcophile and siderophile, here it seems to be majorly controlled by olivine or pyroxenes as it correlates with Cr. The highest correlation coefficients (R; 0.82-0.93) is found for oxide-forming major elements (Fe_2O_3, TiO_2, MnO; Table S5 Supplementary Material and Fig. 7b). This trio correlates well with siderophile metals such as Ga (0.36-0.48; Table S5 Supplementary Material and Fig. 7e), Zn (0.76-0.92; Table S5 Supplementary Material and Fig. 7g), Co (0.61-0.75; Table S5 Supplementary Material and Fig. 7h), and to a lesser extent Cu (0.22-0.32). The moderately high correlation with Cu unlikely results from incorporation of Cu. Copper partitions highly into sulfides as confirmed by high Cu-S correlation coefficient (0.56), and sulfides often co-occur with oxides in U1473A (Section 4.1 and Fig. 7a). This is confirmed by high correlation of sulfur with the oxide-forming major elements (0.71-0.77) and inherent trace elements like Zn (0.65) or Co (0.62) or Ga (0.41) (Table S5 Supplementary Material and Fig. 7a). Interestingly, the correlation coefficient between the S and metals seems to be the highest in S-rich samples (Fig. 7a). P_2O_5 correlates well with the oxide forming-elements (0.44-0.59; Table S5 Supplementary Material and Fig. 7b) and moderately with S (0.27; Table S5 Supplementary Material).

4.2.1. Sulfur speciation and isotopic composition

Sulfur, in addition to its concentration discussed in Section 4.2, was further analyzed for its speciation forms and isotopic composition. Nearly entire S in our rocks is sulfide-S, with sulfate-S being >10% in only 4 of 101 rocks (Fig. 8). The highest sulfate-S content approaches ~24% (Fig. 8). Sulfate-S seems to slightly increase towards the ocean floor (Fig. 8).

The sulfide-S was analyzed for their AVS and CRS contents in the top 450 m of the hole. Here, the AVS-S content in the sulfide-S seems to gradually decrease upwards the hole although this data scatters significantly (Fig. 9).

Sulfur isotopes have been analyzed either in bulk sulfide-S or separately in CRS-S, and AVS-S which also can yield sulfide-S when summed up together. Where, the $\delta^{34}S$ values for CRS-S and AVS-S are obtained, $\delta^{34}S$ is consistently higher by ~0.5 ‰ in CRS-S than in AVS-S. The sulfide-S $\delta^{34}S$ values are between -1‰ and 1 ‰ in 54 of 58 analyzed samples (Table S3 Supplementary Material and Fig. 3). These samples contain only pyrrhotite-chalcopyrite-pentlandite sulfide grains (e.g., Fig. 4a-b) and show relatively low scatter of S and Cu contents (Fig. 3). They predominate throughout the hole with two exceptions. First exception is the aforementioned Sample 9R-3 116/123 located 75 mbsf, which contains the secondary pyrite (Section 4.1) and shows a $\delta^{34}S$ of 3.8‰. Notably most other samples from this interval (0-200 mbsf) display slightly enhanced $\delta^{34}S$ signatures between 0.5‰ and 1.0‰ (Fig. 3). The second exception is found at the bottom of the highly fracture carbonate cemented zone (530-570 mbsf), where one sample displays a $\delta^{34}S$ of 4.8%, and other two between 0.5‰ and 1.5‰ (Fig. 3). In addition, Sample 25R1 127/133 shows a highly negative value of -25.0‰. This result was repeated in two analytical sessions to exclude that was an error (Table S3 Supplementary Material). The $\Delta^{33}S$ values range from -0.035‰ to -0.012‰ in the upper part of the hole (Table S3 Supplementary Material). In the lower part, this range is slightly shifted towards lower values (-0.041‰ to -0.020‰).

4.2.2. Strontium isotopes

Strontium isotopes have been measured in 12 samples equally distributed throughout the hole (Table 1). The range of $^{87}Sr/^{86}Sr$ values obtained in this study (0.70275-0.70313) overlaps with 0.70281 reported for SWIR N-MORBs (Ito et al., 1987). This far from the values of 0.70884 and 0.70915 reported for 12 Ma and modern seawater (McArthur et al. 2012). The $^{87}Sr/^{86}Sr$ values increase upwards the hole (Table 1).

5. DISCUSSION

5.1. Magmatic versus hydrothermal metal transport

Regardless whether the alteration intensity of our samples is slight (3-10%) or moderate (10-29%; Table S4 Supplementary Material and Fig. 9), its impact on sulfur and metal cycle seems to be negligible (Figs. 3, 5-7). Pyrrhotite-pentlandite-chalcopyrite assemblages that exsolved from a sulfide liquid, which are typical sulfides throughout the hole (Fig. 4) are found in many magmatic sulfide deposits (Ballhaus and Sylvester, 2000; Dare et al., 2010; Song et al., 2009) and are commonly interpreted as magmatic in the lower oceanic crust (Miller and Cervantes, 2002). The magmatic origin of our sulfides is also reflected in their sulfide-S $\delta^{34}S$ values. Sulfur isotopes allow to distinguish between the mantle- and seawater-derived sulfur. While mantle $\delta^{34}S$ is 0±2‰ (Oeser et al., 2012; Peters et al., 2010; Tostevin et al., 2014), seawater $\delta^{34}S$ is ~21‰, which elevates $\delta^{34}S$ in hydrothermal sulfides to higher values (typically 2 to 9‰, Peters et al., 2010). We found signature matching hydrothermal sulfides in only two samples. Potentially, also the aforementioned Sample 25R1 127/133 with the highly negative value of -25.0‰ (Section 4.2.1) could have had a hydrothermal signature before, and later be altered to -25.0‰ through microbial reduction (cf., Alt and Shanks, 2011; Oeser et al., 2012). Normally, a portion of hydrothermal sulfur is enclosed in sulfates as revealed for the lower crust in the Oman ophiolite (Oeser et al., 2012). Amon our samples, sulfates are scarce, however, as we documented by the comparison of the obtained total sulfur (TS) and sulfide-S values (Fig. 9 and Section 4.2.1).

The negative $\Delta^{33}S$ signatures (Section 4.2.1) also seem to confirm magmatic and not seawater S source. The seawater $\Delta^{33}S$ signature is +0.050 (Ono et al., 2012; Tostevin et al., 2014), which is far from the slightly negative range of values obtained in our study (-0.041‰ to -0.012‰). Although even some MORBs show higher, close to neutral $\Delta^{33}S$ values, such as +0.001±0.017‰ (2σ; one East Pacific Rice (EPR) sample; Ono et al., 2012) or -0.008‰ (two MAR samples; Peters et al., 2010), Labidi et al. (2012) reported negative $\Delta^{33}S$ values (-0.020±10‰, 2σ) for 13 MORB samples from the MAR, EPR and SWIR ridges, which well overlap our range. The range of $\Delta^{33}S$ signatures (-0.041‰ to -0.020‰) found in the lower crust of the Oman ophiolite (Oeser et al., 2012) is also close to our $\Delta^{33}S$ values. In contrast, higher $\Delta^{33}S$ values are displayed by the overlying sheeted dikes (-0.036‰ to -0.013‰) and pillow basalts (-0.004‰ to +0.002‰; Oeser et al., 2012).

Slightly higher $\Delta^{33}S$ values at the upper part of the hole (Section 4.2.1 and Table S3 Supplementary Material) seem to indicate that flux of seawater-S is enhanced at the upper part of the hole. Although this is not visible by the general alteration rank in our and shipboard samples (Fig. 9), it seems to be supported by enhanced $\delta^{34}S$ (Fig. 3) and to some extent by enhanced sulfate-S (Fig. 8) and the occurrence of pyrite in the top 200 m of the hole. The increased values of $^{87}Sr/^{86}Sr$, $\Delta^{33}S$ and $\delta^{34}S$ at the top of the hole could either result from a direct effect of hydrothermal alteration or from assimilation of hydrothermally altered crust by the gabbro-forming magma. This latter hypothesis could explain no increase in the alteration rank at the upper part of U1473A with respect to what is downwards. On the other hand, this could be also explained by the fact that S addition during low-temperature alteration is often not commensurate with the alteration grade expressed in percent of secondary minerals (Fig. 7 in Bach et al. 2001).

Our observations are consistent with those found in other two long IODP Holes drilled into the lower oceanic crust, 1508-m-deep 735B Hole into Atlantis Bank, and 1415-m-deep U1309D Hole into Atlantis Massif along the MAR. The Cu concentrations in the lower part of Hole 735B is likely fully controlled by magmatic processes. The Cu and Ni trends are stable and clear in this part of the hole (Miller and Cervantes, 2002) as is typical for fresh rocks. In addition, the major magmatic boundary at 960 mbsf is clearly visible in the downhole Cu and Ni profiles. In contrast to that, a hydrothermal overprint probably occurred in the upper part of the hole. There, the least altered rocks contain 610 ppm S contrasting with <100 ppm S in the most altered rocks (Alt and Anderson, 1991). This is further confirmed by enhanced $^{87}Sr/^{86}Sr$ in the top 500 m of the hole with respect to the fresh MORB $^{87}Sr/^{86}Sr$ signature deeper in the hole (Bach et al., 2001). Similarly in Hole U1309D, high $\delta^{34}S$ signatures (6 to 13‰) in the upper section indicate strong hydrothermal overprint, whereas moderate $\delta^{34}S$ signatures (-1 to 1‰ in 9 of 10 samples) from the lower part of the hole are linked to magmatic processes (Delacour et al., 2008).

On the whole, the consistent mineral composition (Section 4.1), metal (Figs. 3, 5-7) and S concentrations (Table S3 Supplementary Material and Fig. 3), Sr (Table 1), and S isotope signatures (Table S3 Supplementary Material and Fig. 3), and S speciation patterns (Figs. 8 and 9) throughout Hole U1473A indicate the predominant role of magmatic processes in the transport of chalcophile metals at the lower oceanic crust with only minor hydrothermal overprint at the top 200 m. This contrasts with the upper oceanic crust known from long ODP Holes 504B (Bach

et al., 2003; Teagle et al., 1998) and 1256D (Alt et al., 2010; Alt and Shanks, 2011), where hydrothermal fluids play an important role in the transport of metals. These observations are consistent with data reported for the Oman ophiolite, where the entire section of the upper lithosphere encompassing the upper and the lower crust is available and was investigated for S isotopes. Here, the sulfide-S of the lower crust consistently shows the mantle $\delta^{34}S$ signature (-2 to +2‰), whereas pillow lavas, sheeted dikes and dike-gabbro transition zone all display enhanced (>2‰) $\delta^{34}S$ values (Oeser et al., 2012). In Atlantis Bank, the upper crust was removed during detachment faulting, subsequent tectonic uplift and erosion (Baines et al., 2003; Dick et al., 2000). The pre-erosional high-temperature seawater circulation was likely limited to the upper crust, and later low-temperature fluids did not significantly affect the S and metal distribution.

5.2. Fractional crystallization controls magmatic metal transport

Downhole Cu and S (Figs. 3 and 5), Fe_2O_3, MnO, Co and P_2O_5 (Fig. 6) trends matching magmatic units and Mg-number trends (Figs. 2 and 5) indicate dominant role of fractional crystallization in the magmatic transport of metals and S. Similar Fe and Ti upward decreasing trends explained by fractional crystallization of oxides are known from many layered intrusion complexes (Charlier et al., 2008; Namur et al., 2012; Zhang et al., 2012). This is further supported by decreasing mode of pentlandite in our sulfide grains upwards the hole (Section 4.1) associated with decreasing whole-rock Ni content which correlate with decreasing Mg-number upwards the hole (Ciazela et al., 2016; Dick et al., 2016; MacLeod et al., 2017).

Our results revealing that metals are involved in fractional crystallization on a large- and medium-scale are consistent with the model of the slow-spread lower oceanic crust proposed by Coogan (2014), which is majorly based on the lower crust of Atlantis Bank (Dick et al., 2000). In his model, Coogan suggests magma bodies of 500-m height which differentiate in isolation from each other (cf. our Fig. 5). Smaller-scale chemical variations (cf. our Figs. 2 and 6) may in return record shorter timescale episodic inflation of the large magma bodies by sill-shaped intrusions emplaced into a crystal mush.

In addition, Coogan proposes that felsic veins form when an almost solid mush fractures and the last increments of interstitial melt are sucked into the fractures. In this view, felsic veins are products of fractional crystallization products of most evolved melt. Considering that metal

content always decrease with progressive fractional crystallization (Figs. 3, 5, and 6), this is consistent with our felsic veins being yet more depleted in Co, Zn, Cu, S and Fe, and Mn than the most evolved gabbros (Section 4.2 and Table S2 Supplementary Material). In fact, the major element composition of the felsic vein match trends obtained by extrapolation of major element compositions in U1473A (MacLeod et al., 2017) and Hess Deep gabbros (Gillis et al., 2014).

The prominent role of fractional crystallization for metal differentiation does not exclude an auxiliary role of other processes. Dick et al. (1991) and Natland et al. (1991) suggest that some oxides in the Atlantis Bank gabbro form as a result of disequilibrium between the melts that precipitated them and the silicate phases. In fact, we found examples of a similar process at igneous layer boundaries where late melt likely intruded mush zone. Here modal oxides and sulfides are enriched with respect to the background gabbro causing largely enhanced Cu and S concentrations (Pieterek et al., 2017). Three samples collected from such boundaries (13R-1 26/33; 13R-1 67/75; 18R-1 18/25; see Table S2 Supplementary Material) are visible as spikes in our Cu and S profiles (110 and 159 mbsf in Figs. 3 and 5, compare also to Table S2 Supplementary Material).

5.3. Coupled oxide-sulfide fractionation

Coexistence of sulfides with oxides documented using ore microscopy (Fig. 4a) along with high correlation coefficient between S, MnO, TiO_2, and Fe_2O_3 (Fig. 6c and Table S5 Supplementary Material) provide strong evidence that sulfides and oxides crystallize nearly simultaneously. Sulfide globules show a flat side at the contact with oxides (Fig. 4a), which indicates that oxides crystallize first and trigger immediate precipitation of sulfides aside. This fact and the common occurrence of sulfide-oxide parageneses both in the oceanic (Natland et al., 1991) and the continental gabbro (Augé et al., 2017) suggest that precipitation of oxides lowers sulfur concentration at sulfide saturation (SCSS) of a given melt.

Keith et al. (2017) who observed similar oxide-sulfide couples in oceanic basalts suggest the sulfides formed due to decreasing oxygen fugacity upon oxide crystallization. On the other hand, we recently proposed that the crystallization of sulfides from slow-spreading ridge magmas is often achieved due to loss of iron (Ciazela et al., 2017). SCSS strongly decreases with the decreasing iron content of the melt, especially in the range of 5–15 wt% FeO (Ariskin et al., 2013; Haughton et al., 1974; O'Neill and Mavrogenes, 2002). In the case of oxide precipitation,

sulfide crystallization could thus result from a synergetic effect of decreasing oxygen fugacity and iron loss. Such a synergetic effect could explain (Fig. 4a) the discussed textural features (Fig. 4a) and the excellent correlation between the sulfur and siderophile metals (Fig 6c, e-h).

5.4. Role of magma supply for fractional crystallization in slow-spread oceanic ridges

Slow-spread oceanic crust is thinner and more heterogeneous than fast-spread oceanic crust. (Blackman et al., 2011; Blackman and Collins, 2010; Cannat, 1996; Cannat et al., 1997; Ciazela et al., 2015; Dick et al., 2008). These features of the slow-spread oceanic crust affect how sulfides differentiate during magmatic processes and how metals are transported between the mantle and the ocean floor. Where magma supply is low, sulfides typically differentiate through melt-mantle reaction (Ciazela et al., 2017, 2015). Melt-mantle reaction leads to high sulfide enrichment at the contacts of gabbro and peridotite (Ciazela et al., 2017). In Atlantis Bank, where the magma supply is high (Ciazela et al., 2015; Dick et al., 2000), sulfides differentiate mostly through fractional crystallization. Although melt-rock reaction may occur within crust (Lissenberg et al., 2013; Lissenberg and Dick, 2008), and affect sulfides and oxides (Dick et al., 1991; Natland et al., 1991), this is only a local process. A disequilibrium strong enough to drive sulfide precipitation can occur only at layer boundaries where two distinct lithologies meet such as olivine gabbro and gabbro (Section 5.3 and Pieterek et al. 2017).

Interaction between mantle and melt although strongly affecting sulfides (Ciazela et al., 2017) can occur only at the rims of magmatic plutons, and these extend over many kilometers in Atlantis Bank (Dick et al., 2015). This stands in contrast with other OCCs as Kane Megamullion (Dick et al., 2010, 2008) or even Atlantis Massif (Blackman et al., 2011; Blackman and Collins, 2010) where gabbroic bodies are much thinner. As a consequence, sulfides in Atlantis Bank are mostly controlled through gravitationally driven fractional crystallization with oxides and sulfides crystallizing and separating early and therefore tending to accumulate at the lower part of gabbroic bodies. The lower parts of gabbroic bodies are by ~50% enriched in Cu and by ~100% enriched in S with respect to the upper parts (Fig. 3). In addition, gabbro bodies located deeper in the crust are enriched in chalcophile elements with respect to shallower gabbro bodies. Both facts are consistent with MORBs having sulfur concentrations above sulfide saturation during their ascent through the slow-spread lower crust with high magma supply.

5.5. Implications for seafloor massive sulfides

Where magma supply is low, sulfides typically differentiate through melt-mantle reaction, and melt-mantle reaction leads to high sulfide enrichment at the contacts of gabbro and peridotite (Ciazela et al., 2017). These zones are often located shallow under the seafloor and are easy to penetrate by hydrothermal circulation (Ciazela et al., 2017). These zones of magmatic enrichment related to melt refertilization might be one of the reasons why massive sulfide deposits form mostly at the slow spreading ridges and not at the fast spreading ridges (Hannington et al., 2011). Many SMS deposits in the recent oceans, including those largest and with the highest Cu grade (Petersen and Hein, 2013; Hein et al., 2013), are hosted in the peridotite-dominated lithosphere with a thin and heterogeneous crust (Andreani et al., 2014; Ciazela et al., 2015; Petersen et al., 2009; Tucholke et al., 2013), where melt-mantle reaction is likely more enhanced (Ciazela et al., 2017). This peculiar distribution of SMS deposits seems to reflect the style of magmatic differentiation determined by magma supply, although not necessarily the spreading rate (cf. Hannington et al. 2011). Atlantis Bank with its low spreading provides a primary example of that. In spite of the low local spreading rate of 14.6 mm (Zhou and Dick, 2013), the local magma supply is relatively high, and no seafloor massive sulfides have been found on the Atlantis Bank ocean floor to date (Dick et al., 2015). In contrast, SMS deposits are abundant towards southwest (Dragon Flag OCC; Ciazela et al., 2015; Tao et al., 2014, 2012, 2011) and northeast (53°E OCC; Ciazela et al., 2015; Tao et al., 2014, 2012; Zhou and Dick, 2013) where lithosphere is thinner and more melt-mantle reaction occur.

6. CONCLUSIONS

1. The consistent mineral, trace element, and S and Sr isotope compositions throughout the hole indicates the predominant role of magmatic processes in the transport of chalcophile metals through the lower oceanic crust. Downhole Cu and S, Fe_2O_3, MnO, Co and P_2O_5 trends matching magmatic units and Mg-number trends indicate dominant role of fractional crystallization in the magmatic transport of metals and S. Similar Fe and Ti upward-decreasing trends explained by fractional crystallization of oxides are known from many layered intrusion complexes.
2. Coexistence of sulfides with oxides and high correlation coefficient between S, MnO, TiO_2, and Fe_2O_3 indicate that sulfides and oxides crystallize nearly simultaneously. Based on

textural features, we have demonstrated that oxides crystallized first and triggered immediate sulfide precipitation. The crystallization of sulfides during melt-mantle reaction can be achieved by lowering the level of sulfide concentration at sulfide saturation in the portion of melt suffered by loss of iron and decreased oxygen fugacity after oxide precipitation.

3. Due to high magma supply in Atlantis Bank, sulfides differentiate mostly through fractional crystallization. Sulfides fractionate early and thus tend to accumulate at the lower part of gabbroic bodies. The lower parts of gabbroic bodies are by ~50% enriched in Cu and by ~100% enriched in S with respect to the upper parts. In addition, gabbro bodies located deeper in the crust are enriched in chalcophile elements with respect to shallower gabbro bodies. Both facts are consistent with MORBs having sulfur concentrations above sulfide saturation during their ascent through the slow-spread lower crust with high magma supply.
4. Most seafloor massive sulfides, especially with the highest Cu-grades, occur along slow-spread oceanic lithosphere with relatively low magma supply. In Atlantis Bank where magma budget is high and the crust was fully developed, zones of the highest sulfide enrichment show lower degree of metal concentrations (up to ~130 ppm Cu) than analogical zones in the slow-spread crust with a low magma supply (up to ~300 ppm Cu). In addition, the former are emplaced at the bottom of gabbroic bodies where hydrothermal fluids have only limited access. This is likely the reason why seafloor massive sulfides have not been found at Atlantis Bank although they are common in oceanic core complexes.

ACKNOWLEDGEMENTS

We would like to thank the other Expedition 360 Scientists and the crew of JOIDES Resolution. Without this group effort, there would have been no samples for this study. We thank A. Fugmann and A. Lutter from Universität Münster for conducting the S isotope analyses, and S. Schurr, and F. Boekhout for their help during J. Ciazela's stay in Münster. Further help was provided by M. Keith from the University of Leicester, G. Wigowska, and M. Nowak from the Adam Mickiewicz University, and J. Feige, F. Holtz, and C. Zhang from the Leibniz Universität Hannover, for which we are grateful. This research was funded by the grants of the National Science Center Poland (KO 1723/23-1) and the Graduate Academy of Leibniz Universität

Hannover (60421784) to J. Ciazela, and the German Science Foundation (Bo2941/4-1) to J. Koepke and H. Strauss.

REFERENCES

Alt, J.C., Anderson, T.F., 1991. Mineralogy and Isotopic Composition of Sulfur in Layer 3 Gabbros From the Indian Ocean, Hole 735B. Proc. Ocean Drill. Program, Sci. Results 118, 113–125.

Alt, J.C., Anderson, T.F., Bonnell, L., 1989. The geochemistry of sulfur in a 1.3 km section of hydrothermally altered oceanic crust, DSDP Hole 504B. Geochim. Cosmochim. Acta 53, 1011–1023. doi:10.1016/0016-7037(89)90206-8

Alt, J.C., Laverne, C., Coggon, R.M., Teagle, D.A.H., Banerjee, N.R., Morgan, S., 2010. Subsurface structure of a submarine hydrothermal system in ocean crust formed at the East Pacific Rise, ODP/IODP Site 1256. Geochemistry, Geophys. Geosystems 11, Q10010. doi:10.1029/2010GC003144

Alt, J.C., Shanks, W.C., 2011. Microbial sulfate reduction and the sulfur budget for a complete section of altered oceanic basalts, IODP Hole 1256D (eastern Pacific). Earth Planet. Sci. Lett. 310, 73–83. doi:10.1016/j.epsl.2011.07.027

Andreani, M., Escartin, J., Delacour, A., Ildefonse, B., Godard, M., Dyment, J., Fallick, A.E., Fouquet, Y., 2014. Tectonic structure, lithology, and hydrothermal signature of the Rainbow massif (Mid-Atlantic Ridge 36°14'N). Geochemistry, Geophys. Geosystems 15, 3543–3571. doi:10.1002/2014GC005269.Received

Ariskin, A.A., Danyushevsky, L. V., Bychkov, K.A., McNeill, A.W., Barmina, G.S., Nikolaev, G.S., 2013. Modeling solubility of Fe-Ni sulfides in basaltic magmas: The effect of nickel. Econ. Geol. 108, 1983–2003. doi:10.2113/econgeo.108.8.1983

Augé, T., Bailly, L., Roig, J.-Y., 2017. A double Fe-Ti oxide and Fe-sulphide liquid immiscibility in the Itsindro Gabbro Complex, Madagascar. J. African Earth Sci. 135, 152–172. doi:10.1016/j.jafrearsci.2017.08.009

Bach, W., Alt, J.C., Niu, Y., Humphris, S.E., Erzinger, J., Dick, H.J.B., 2001. The geochemical

consequences of late-stage low-grade alteration of lower ocean crust at the SW Indian Ridge: Results from ODP Hole 735B (Leg 176). Geochim. Cosmochim. Acta 65, 3267–3287. doi:10.1016/S0016-7037(01)00677-9

Bach, W., Bernhard, P.E., Hart, S.R., Blusztajn, J.S., 2003. Geochemistry of hydrothermally altered oceanic crust: DSDP/ODP Hole 504B - Implications for seawater-crust exchange budgets and Sr- and Pb-isotopic evolution of the mantle. Geochemistry, Geophys. Geosystems 4, 40–55. doi:10.1029/2002GC000419

Baines, A.G., Cheadle, M.J., John, B.E., Grimes, C.B., Schwartz, J.J., Wooden, J.L., 2009. SHRIMP Pb / U zircon ages constrain gabbroic crustal accretion at Atlantis Bank on the ultraslow-spreading Southwest Indian Ridge. Earth Planet. Sci. Lett. 287, 540–550. doi:10.1016/j.epsl.2009.09.002

Baines, G., Cheadle, M.J., Dick, H.J.B., Scheirer, A.H., John, B.E., Kusznir, N.J., Matsumoto, T., 2003. Mechanism for generating the anomalous uplift of oceanic core complexes: Atlantis Bank, southwest Indian Ridge. Geology 31, 1105–1108. doi:10.1130/G19829.1

Ballhaus, C., Sylvester, P., 2000. Noble Metal Enrichment Processes in the Merensky Reef, Bushveld Complex. J. Petrol. 41, 545–561. doi:10.1093/petrology/41.4.545

Blackman, D.K., Collins, J., 2010. Lower crustal variability and the crust/mantle transition at the Atlantis Massif oceanic core complex. Geophys. Res. Lett. 37, 1–5. doi:10.1029/2010GL045165

Blackman, D.K., Ildefonse, B., John, B.E., Ohara, Y., Miller, D.J., Abe, N., Abratis, M., Andal, E.S., Andreani, M., Awaji, S., Beard, J.S., Brunelli, D., Charney, A.B., Christie, D.M., Collins, J., Delacour, A.G., Delius, H., Drouin, M., Einaudi, F., Escartín, J., Frost, B.R., Früh-Green, G., Fryer, P.B., Gee, J.S., Godard, M., Grimes, C.B., Halfpenny, A., Hansen, H.-E., Harris, A.C., Tamura, A., Hayman, N.W., Hellebrand, E., Hirose, T., Hirth, J.G., Ishimaru, S., Johnson, K.T.M., Karner, G.D., Linek, M., MacLeod, C.J., Maeda, J., Mason, O.U., McCaig, A.M., Michibayashi, K., Morris, A., Nakagawa, T., Nozaka, T., Rosner, M., Searle, R.C., Suhr, G., Tominaga, M., von der Handt, A., Yamasaki, T., Zhao, X., 2011. Drilling constraints on lithospheric accretion and evolution at Atlantis Massif, Mid-Atlantic

Ridge 30°N. J. Geophys. Res. 116, B07103. doi:10.1029/2010JB007931

Boschen, R.E., Rowden, A.A., Clark, M.R., Gardner, J.P.A., 2013. Mining of deep-sea seafloor massive sulfides: A review of the deposits, their benthic communities, impacts from mining, regulatory frameworks and management strategies. Ocean Coast. Manag. 84, 54–67. doi:10.1016/j.ocecoaman.2013.07.005

Cannat, M., 1996. How thick is the magmatic crust at slow spreading oceanic ridges? J. Geophys. Res. 101, 2847–2857.

Cannat, M., Lagabrielle, Y., Bougault, H., Casey, J., de Coutures, N., Dmitriev, L., Fouquet, Y., 1997. Ultramafic and gabbroic exposures at the Mid-Atlantic Ridge: geological mapping in the 15°N region. Tectonophysics 279, 193–213. doi:10.1016/S0040-1951(97)00113-3

Charlier, B., Sakoma, E., Sauvé, M., Stanaway, K., Vander, J., Duchesne, J., 2008. The Grader layered intrusion (Havre-Saint-Pierre Anorthosite , Quebec) and genesis of nelsonite and other Fe – Ti – P ores 101, 359–378. doi:10.1016/j.lithos.2007.08.004

Ciazela, J., Dick, H.J.B., Koepke, J., Pieterek, B., Muszynski, A., Botcharnikov, R., Kuhn, T., 2017. Thin crust and exposed mantle control sulfide differentiation in slow-spreading ridge magmas. Geology 45. doi:10.1130/G39287.1

Ciazela, J., Dick, H.J.B., MacLeod, C.J., Blum, P., the Expedition 360 Scientists, 2016. IODP Expedition 360: first stage of drilling into Earth's Mantle. Przegląd Geol. 64, 889–895.

Ciazela, J., Koepke, J., Dick, H.J.B., Muszynski, A., 2015. Mantle rock exposures at oceanic core complexes along mid-ocean ridges. Geologos 21. doi:10.1515/logos-2015-0017

Coogan, L.A., 2014. The Lower Oceanic Crust, in: Treatise on Geochemistry: Second Edition. Elsevier Ltd., pp. 497–541. doi:10.1016/B978-0-08-095975-7.00316-8

Dare, S.A.S., Barnes, S.J., Prichard, H.M., 2010. The distribution of platinum group elements (PGE) and other chalcophile elements among sulfides from the Creighton Ni-Cu-PGE sulfide deposit, Sudbury, Canada, and the origin of palladium in pentlandite. Miner. Depos. 45, 765–793. doi:10.1007/s00126-010-0295-6

Delacour, A., Früh-Green, G.L., Bernasconi, S.M., 2008. Sulfur mineralogy and geochemistry of serpentinites and gabbros of the Atlantis Massif (IODP Site U1309). Geochim. Cosmochim. Acta 72, 5111–5127. doi:10.1016/j.gca.2008.07.018

Dick, H.J.B., Lissenberg, C.J., Warren, J.M., 2010. Mantle Melting, Melt Transport, and Delivery Beneath a Slow-Spreading Ridge: The Paleo-MAR from 23 15'N to 23 45'N. J. Petrol. 51, 425–467. doi:10.1093/petrology/egp088

Dick, H.J.B., Macleod, C.J., Blum, P., 2015. Southwest Indian Ridge Lower Crust and Moho: the nature of the lower crust and Moho at slower spreading ridges (SloMo-Leg 1). Int. Ocean Discov. Progr. Sci. Prospect. 360.

Dick, H.J.B., Macleod, C.J., Blum, P., the Expedition 360 Scientists, 2016. Expedition 360 Preliminary report: Southwest Indian Ridge lower crust and Moho. International Ocean Discovery Program.

Dick, H.J.B., Meyer, P.S., Bloomer, S.H., Kirby, S., Stakes, D., Mawer, C., 1991. Lithostratigraphic evolution of an in-situ section of oceanic layer 3. Proc. Ocean Drill. Progr. 118, 439–538.

Dick, H.J.B., Natland, J.H., Alt, J.C., Bach, W., Bideau, D., Gee, J.S., Haggas, S., Hertogen, J.G.H., Hirth, G., Holm, P.M., Ildefonse, B., Iturrino, G.J., John, B.E., Kelley, D.S., Kikawa, E., Kingdon, A., Leroux, P.J., Maeda, J., Meyer, P.S., Miller, D.J., Naslund, H.R., Niu, Y.L., Robinson, P.T., Snow, J., Stephen, R., Trimby, P.W., Worm, H.U., Yoshinobu, A., 2000. A long in situ section of the lower ocean crust: Results of ODP Leg 176 drilling at the Southwest Indian Ridge. Earth Planet. Sci. Lett. 179, 31–51.

Dick, H.J.B., Tivey, M.A., Tucholke, B.E., 2008. Plutonic foundation of a slow-spreading ridge segment: Oceanic core complex at Kane Megamullion, 23°30′N, 45°20′W. Geochemistry, Geophys. Geosystems 9, Q05014. doi:10.1029/2007GC001645

Gillis, K.M., Snow, J.E., Klaus, A., Abe, N., Adrião, A.B., Akizawa, N., Ceuleneer, G., Cheadle, M.J., Faak, K., Falloon, T.J., Friedman, S. a, Godard, M., Guerin, G., Harigane, Y., Horst, A.J., Hoshide, T., Ildefonse, B., Jean, M.M., John, B.E., Koepke, J., Machi, S., Maeda, J., Marks, N.E., McCaig, A.M., Meyer, R., Morris, A., Nozaka, T., Python, M., Saha, A.,

Wintsch, R.P., 2014. Primitive layered gabbros from fast-spreading lower oceanic crust. Nature 505, 204–7. doi:10.1038/nature12778

Hannington, M., Jamieson, J., Monecke, T., Petersen, S., 2010. Sea-Floor Massive Sulfides and Base Metal Resources: Toward an Estimate of Global Sea-Floor Massive Sulfide Potential. Soc. Econ. Geol. Inc. 317–338.

Hannington, M., Jamieson, J., Monecke, T., Petersen, S., Beaulieu, S., 2011. The abundance of seafloor massive sulfide deposits. Geology 39, 1155–1158. doi:10.1130/G32468.1

Haughton, D.R., Roeder, P.L., Skinner, B.J., 1974. Solubility of sulfur in mafic magmas. Econ. Geol. 69, 451–467. doi:10.2113/gsecongeo.69.4.451

Hein, J.R., Mizell, K., Koschinsky, A., Conrad, T., 2013. Deep-ocean mineral deposits as a source of critical metals for high- and green-technology applications: Comparison with land-based resources. Ore Geol. Rev. 51, 1–14. doi:10.1016/j.oregeorev.2012.12.001

Hoagland, P., Beaulieu, S., Tivey, M.A., Eggert, R.G., German, C., Glowka, L., Lin, J., 2010. Deep-sea mining of seafloor massive sulfides. Mar. Policy 34, 728–732. doi:10.1016/j.marpol.2009.12.001

Ito, E., White, W.M., Göpel, C., 1987. The O, Sr, Nd and Pb isotope geochemistry of MORB. Chem. Geol. 62, 157–176. doi:10.1016/0009-2541(87)90083-0

Lissenberg, C.J., Dick, H.J.B., 2008. Melt-rock reaction in the lower oceanic crust and its implications for the genesis of mid-ocean ridge basalt. Earth Planet. Sci. Lett. 271, 311–325. doi:10.1016/j.epsl.2008.04.023

Lissenberg, C.J., MacLeod, C.J., Howard, K. a., Godard, M., 2013. Pervasive reactive melt migration through fast-spreading lower oceanic crust (Hess Deep, equatorial Pacific Ocean). Earth Planet. Sci. Lett. 361, 436–447. doi:10.1016/j.epsl.2012.11.012

Lissner, M., König, S., Luguet, A., le Roux, P.J., Schuth, S., Heuser, A., le Roex, A.P., 2014. Selenium and tellurium systematics in MORBs from the southern Mid-Atlantic Ridge (47–50°S). Geochim. Cosmochim. Acta 144, 379–402. doi:10.1016/j.gca.2014.08.023

MacLeod, C.J., Dick, H.J.B., Blum, P., the Expedition 360 Scientists, 2017. Soutwest Indian Ridge Lower Crust and Moho. Proc. Int. Ocean Discov. Progr. 360.

Miller, J., Cervantes, P., 2002. Sulfide mineral chemistry and petrography and platinum group element composition in gabbroic rocks from the Southwest Indian Ridge, in: Proceedings of the Ocean Drilling Program, Scientific Results. pp. 1–29.

Namur, O., Charlier, B., Holness, M.B., 2012. Dual origin of Fe-Ti-P gabbros by immiscibility and fractional crystallization of evolved tholeiitic basalts in the Sept Iles layered intrusion. Lithos 154, 100–114. doi:10.1016/j.lithos.2012.06.034

Natland, J.H., Meyer, P.S., Dick, H.J.B., Bloomer, S.H., 1991. Magmatic oxides and sulfides in gabbroic rocks from Hole 735B and the later development of the liquid line of descent. Proc. Ocean Drill. Program, Sci. Results 118, 75–111.

O'Neill, H.S.C., Mavrogenes, J.A., 2002. The Sulfide Capacity and the Sulfur Content at Sulfide Saturation of Silicate Melts at 1400°C and 1 bar. J. Petrol. 43, 1049–1087. doi:10.1093/petrology/43.6.1049

Oeser, M., Strauss, H., Wolff, P.E., Koepke, J., Peters, M., Garbe-Schönberg, D., Dietrich, M., 2012. A profile of multiple sulfur isotopes through the Oman ophiolite. Chem. Geol. 312–313, 27–46. doi:10.1016/j.chemgeo.2012.04.008

Ono, S., Keller, N.S., Rouxel, O., Alt, J.C., 2012. Sulfur-33 constraints on the origin of secondary pyrite in altered oceanic basement. Geochim. Cosmochim. Acta 87, 323–340. doi:10.1016/j.gca.2012.04.016

Peters, M., Strauss, H., Farquhar, J., Ockert, C., Eickmann, B., Jost, C.L., 2010. Sulfur cycling at the Mid-Atlantic Ridge: A multiple sulfur isotope approach. Chem. Geol. 269, 180–196. doi:10.1016/j.chemgeo.2009.09.016

Petersen, S., Kuhn, K., Kuhn, T., Augustin, N., Hékinian, R., Franz, L., Borowski, C., 2009. The geological setting of the ultramafic-hosted Logatchev hydrothermal field (14°45′N, Mid-Atlantic Ridge) and its influence on massive sulfide formation. Lithos 112, 40–56. doi:10.1016/j.lithos.2009.02.008

Pieterek, B., Ciazela, J., Koepke, J., Strauss, H., Dick, H., Duczmal-Czernikiewicz, A., Bender, M., Muszyński, A., 2017. Layer boundaries attract sulfides throughout the igneous layering of the lower oceanic crust : IODP Hole U1473A, Atlantis Bank, Southwest Indian Ridge. Mineral. - Spec. Pap. 47, 36.

Song, X.Y., Keays, R.R., Zhou, M.F., Qi, L., Ihlenfeld, C., Xiao, J.F., 2009. Siderophile and chalcophile elemental constraints on the origin of the Jinchuan Ni-Cu-(PGE) sulfide deposit, NW China. Geochim. Cosmochim. Acta 73, 404–424. doi:10.1016/j.gca.2008.10.029

Tao, C., Li, H., Huang, W., Han, X., Wu, G., Su, X., Zhou, N., Lin, J., He, Y., Zhou, J., 2011. Mineralogical and geochemical features of sulfide chimneys from the 49°39′E hydrothermal field on the Southwest Indian Ridge and their geological inferences. Chinese Sci. Bull. 56, 2828–2838. doi:10.1007/s11434-011-4619-4

Tao, C., Li, H., Jin, X., Zhou, J., Wu, T., He, Y., Deng, X., Gu, C., Zhang, G., Liu, W., 2014. Seafloor hydrothermal activity and polymetallic sulfide exploration on the southwest Indian ridge. Chinese Sci. Bull. 59, 2266–2276. doi:10.1007/s11434-014-0182-0

Tao, C., Lin, J., Guo, S., Chen, Y.J., Wu, G., Han, X., German, C.R., Yoerger, D.R., Zhou, N., Li, H., Su, X., Zhu, J., 2012. First active hydrothermal vents on an ultraslow-spreading center: Southwest Indian Ridge. Geology 40, 47–50. doi:10.1130/G32389.1

Teagle, D.A.H., Alt, J.C., Halliday, A.N., 1998. Tracing the chemical evolution of fluids during hydrothermal recharge: Constraints from anhydrite recovered in ODP Hole 504B. Earth Planet. Sci. Lett. 155, 167–182. doi:10.1016/S0012-821X(97)00209-4

Tostevin, R., Turchyn, A. V., Farquhar, J., Johnston, D.T., Eldridge, D.L., Bishop, J.K.B., McIlvin, M., 2014. Multiple sulfur isotope constraints on the modern sulfur cycle. Earth Planet. Sci. Lett. 396, 14–21. doi:10.1016/j.epsl.2014.03.057

Tucholke, B.E., Humphris, S.E., Dick, H.J.B., 2013. Cemented mounds and hydrothermal sediments on the detachment surface at Kane Megamullion: A new manifestation of hydrothermal venting. Geochemistry, Geophys. Geosystems 14, 3352–3378. doi:10.1002/ggge.20186

Zhang, X.Q., Song, X.Y., Chen, L.M., Xie, W., Yu, S.Y., Zheng, W.Q., Deng, Y.F., Zhang, J.F., Gui, S.G., 2012. Fractional crystallization and the formation of thick Fe-Ti-V oxide layers in the Baima layered intrusion, SW China. Ore Geol. Rev. 49, 96–108. doi:10.1016/j.oregeorev.2012.09.003

Zhou, H., Dick, H.J.B., 2013. Thin crust as evidence for depleted mantle supporting the Marion Rise. Nature 494, 195–200. doi:10.1038/nature11842

TABLES

Table 1. Isotopic signatures and contents of Sr in the U1473A gabbros

Sample	$\delta^{87}Sr$		Sr (ppm)
2R-1 37/46	0.70290		144
3R-3 120/128	0.70302		119
5R-1 121/129	0.70285		103
7R-2 33/40	0.70313		159
23R-2 130/134	0.70287		161
36R-3 23/30	0.70284		184
49R-1 84/96	0.70285		179
51R-5 48/57	0.70282		179
59R-3 0/10	0.70282		173
75R-1 83/91	0.70275		135
76R-1 13/23	0.70275		180
83R-9 88/98	0.70276		161
Standard			
NBS 987	0.710234 ± 7	(2 SD; n=7)	
Reference			
N-MORB from SWIR	0.70281	(Ito 1987)	
Modern seawater	0.70915	(McArthur 2012)	
12 Ma seawater	0.70884	(McArthur 2012)	

SD - standard deviation; n- number of measurements

FIGURES

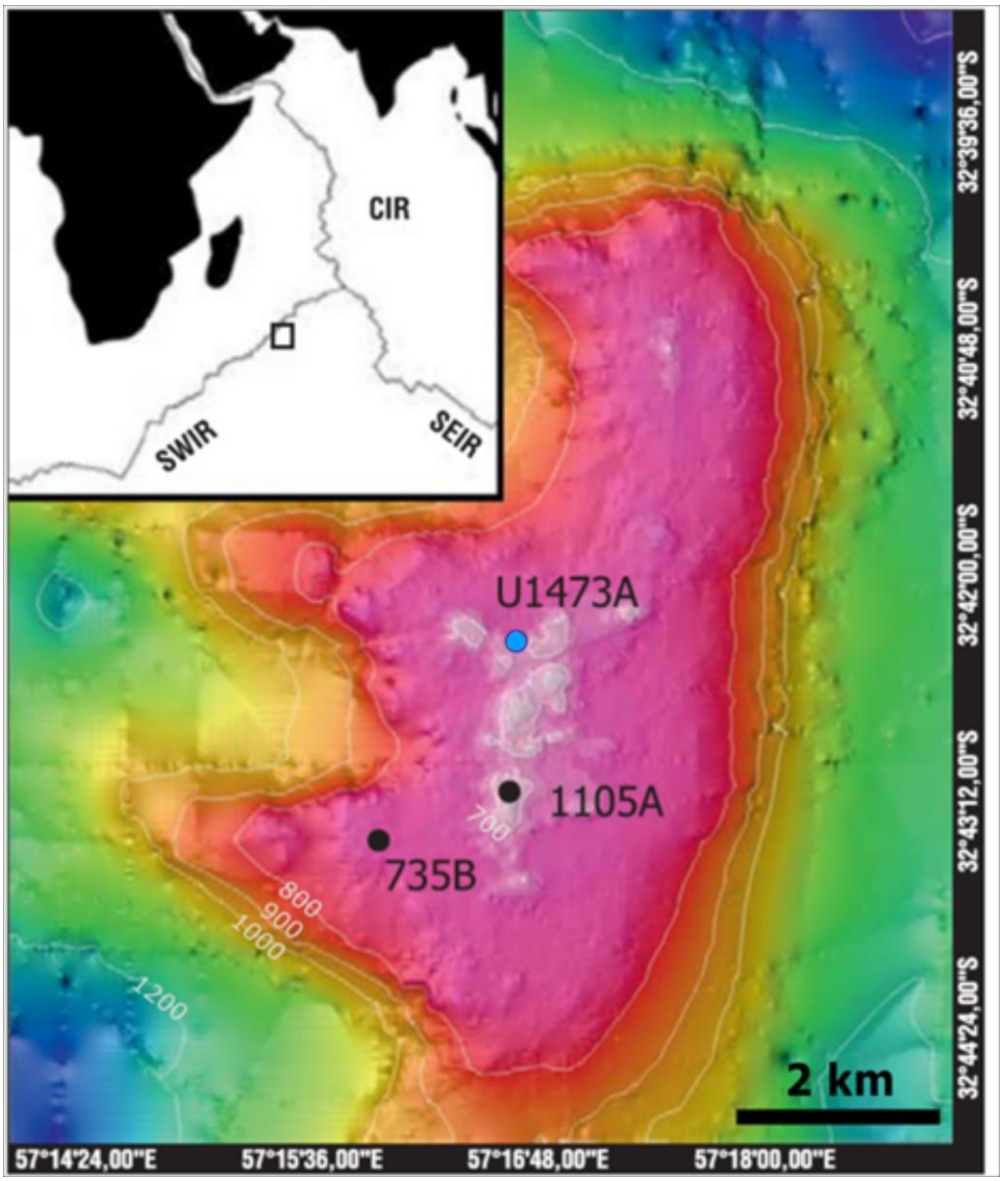

Fig. 1. Bathymetry map showing the flat-topped platform of the Atlantis Bank at a depth of 700-800 meters below sea level (see the contour lines). The blue dot marks the location of a recent IODP Hole U1473A. The black dots represent two previous holes. The inset shows Atlantis Bank's location along the Southwest Indian Ridge (SWIR) in the Indian Ocean. CIR – Central Indian Ridge, SEIR – Southeast Indian Ridge. Modified from Ciazela et al. (2016).

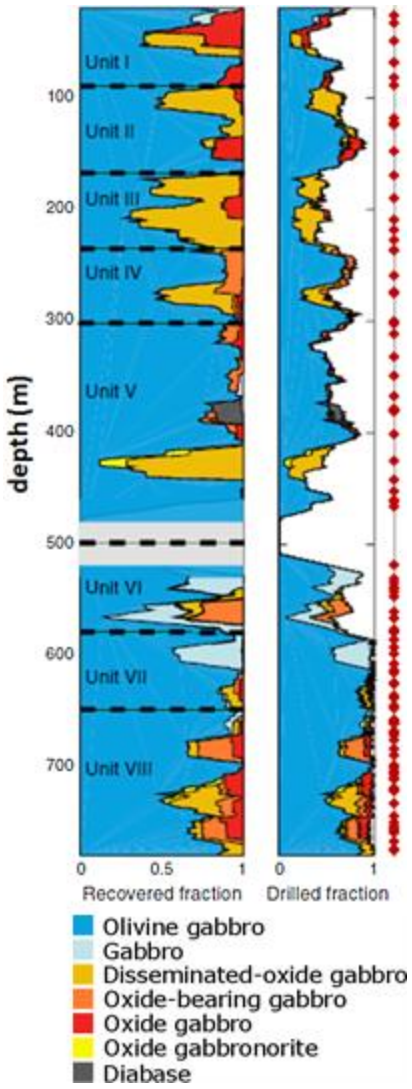

Fig. 2. Lithostratigraphy of IODP Hole U1473A. Relative rock abundances are averaged over 20 running meters. The right column shows relative abundances in drilled material. Note that recovery rate is ~45% in the upper part of the hole and close to 100% in the lower part of the hole. A 30-m long interval in the middle part was drilled without coring. Mostly olivine gabbro were recovered. Gabbro and a variety of oxide gabbros are minor but occur throughout the hole. Diabase is present only locally, for example in veins. The axis on the right side shows the distribution of 101 samples (red diamonds) studied in this paper. Units I-VIII were distinguished based on the shipboard macroscopic core description (MacLeod et al., 2017). Modified from Dick et al. (2016) and Ciazela et al. (2016).

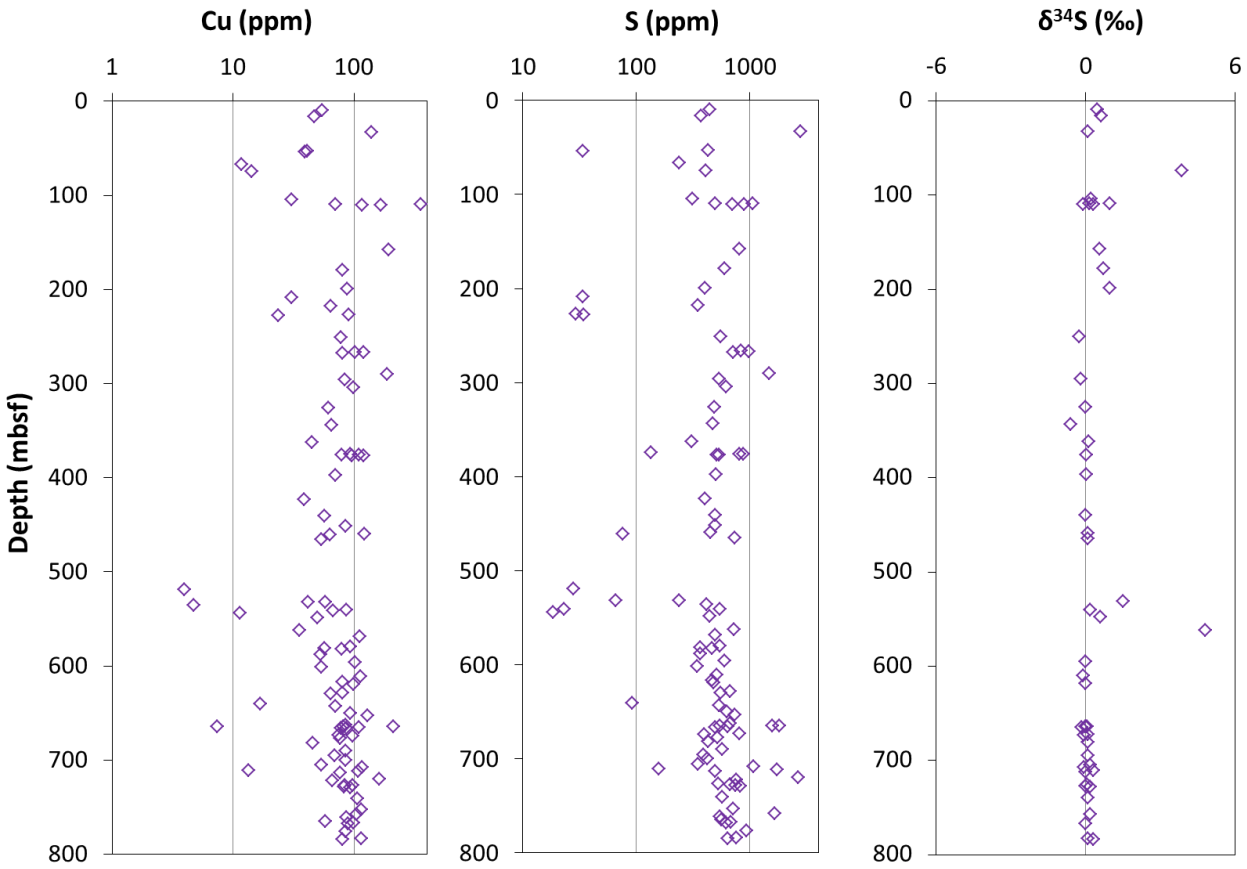

Fig. 3. IODP U1473A downhole profiles of the Cu and S contents along with the $\delta^{34}S$ signatures.

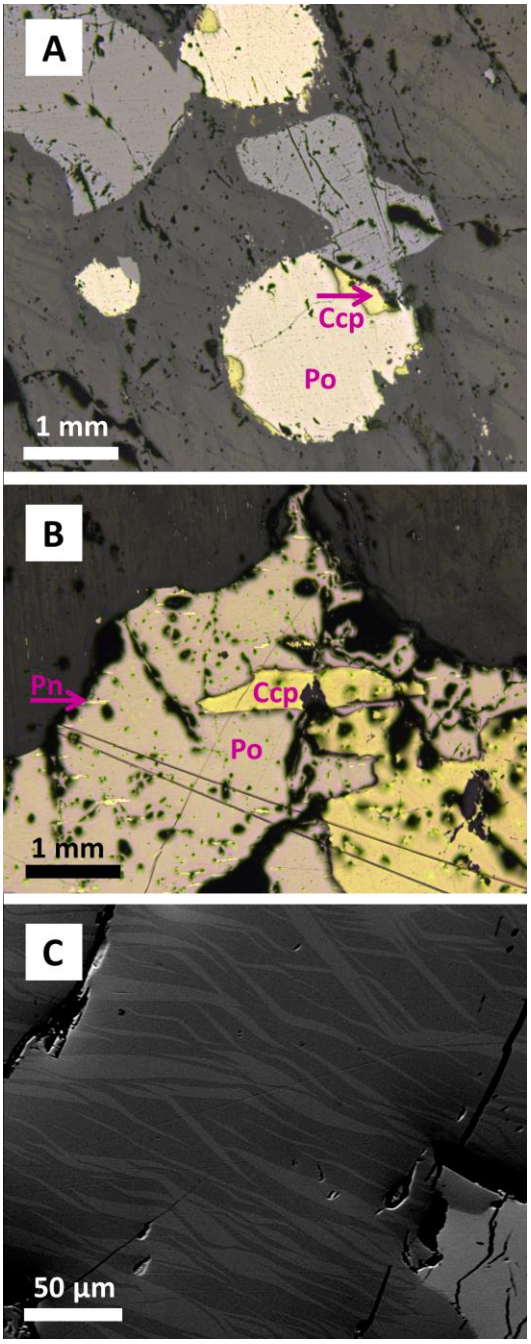

Fig. 4. A) Globular sulfides (yellow) in sample U1473A-75R-1 83/91-CIAZ. The left globule is enclosed in clinopyroxene (dark grey). Note that the sulfides are associated with the iron-titanium oxides (bright grey). Reflected light. B) Pentlandite (Pn) exsolutions in pyrrhotite (Po) in Sample U1473A-80R-7 90/100-CIAZ. Ccp is chalcopyrite. Reflected light. C) Troilite (bright bands) exsolved from pyrrhotite (dark bands) in sample U1473A-82R-6 43/53-CIAZ. Back-scattered electron (BSE) image.

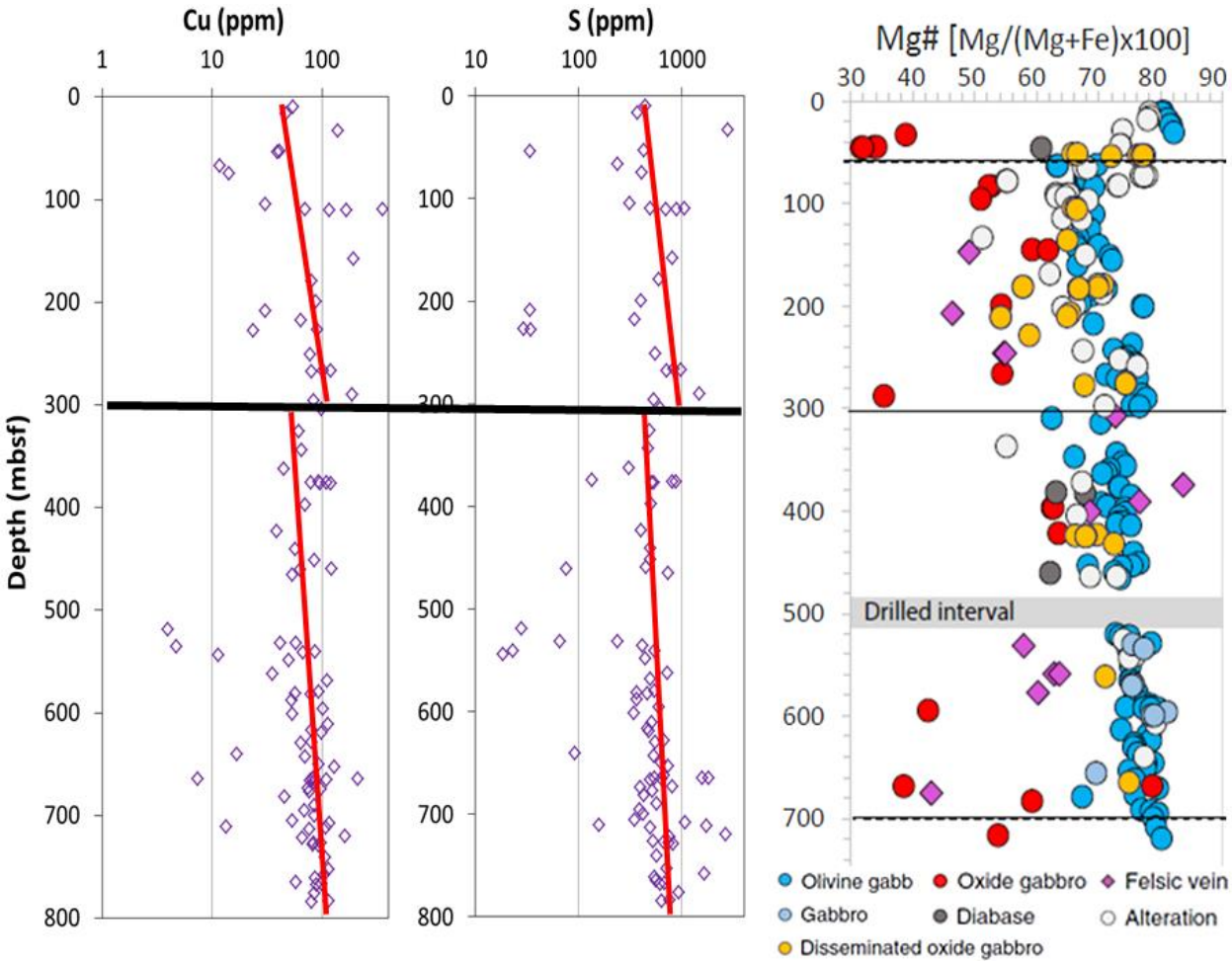

Fig. 5. IODP U1473A downhole profiles of the Cu and S contents along with Mg-numbers (Mg#). Note that two large-scale gabbroic bodies can be distinguished based on Mg#s, and that Cu and S contents correlate with the Mg#s trends in both of these bodies. The enhanced Mg#s in the top 60 m might result from hydrothermal alteration (see Section 4.1), and therefore neither Cu-Mg# nor S-Mg# correlation can be observed there. Adapted from Dick et al. (2016).

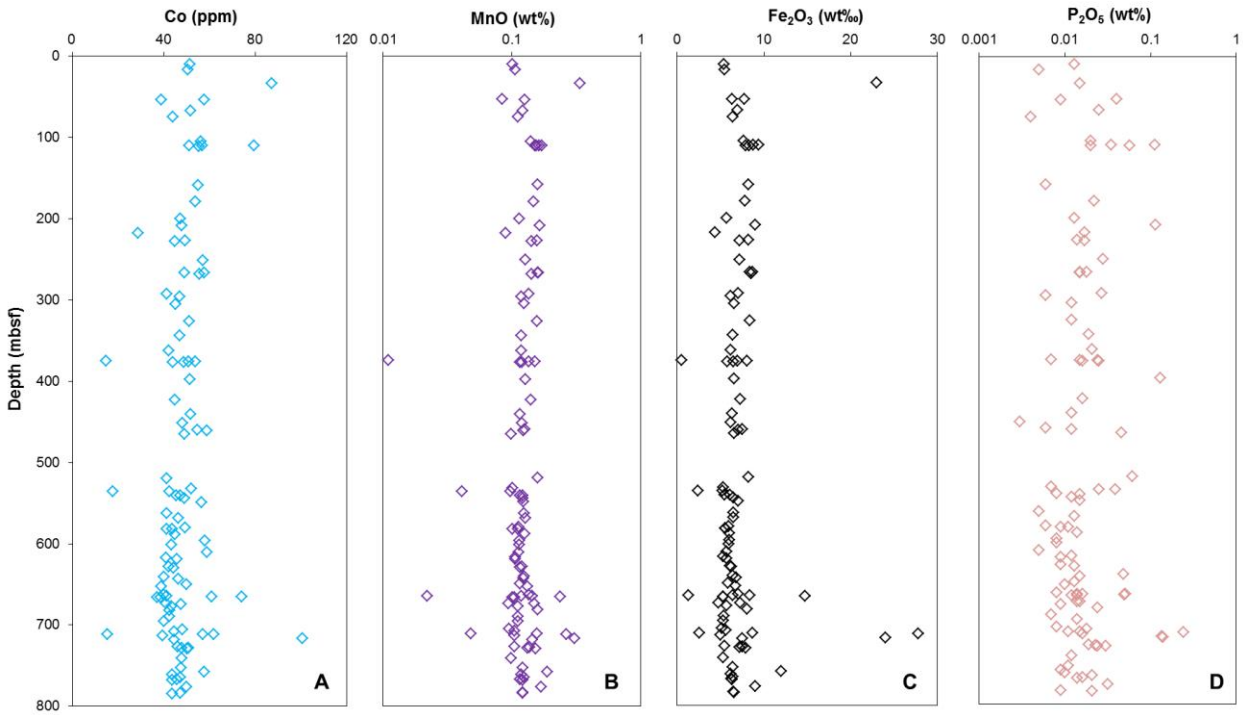

Fig. 6. IODP U1473A downhole profiles of the Co (A), MnO (B), Fe_2O_3 (C), and P_2O_5 (D) contents.

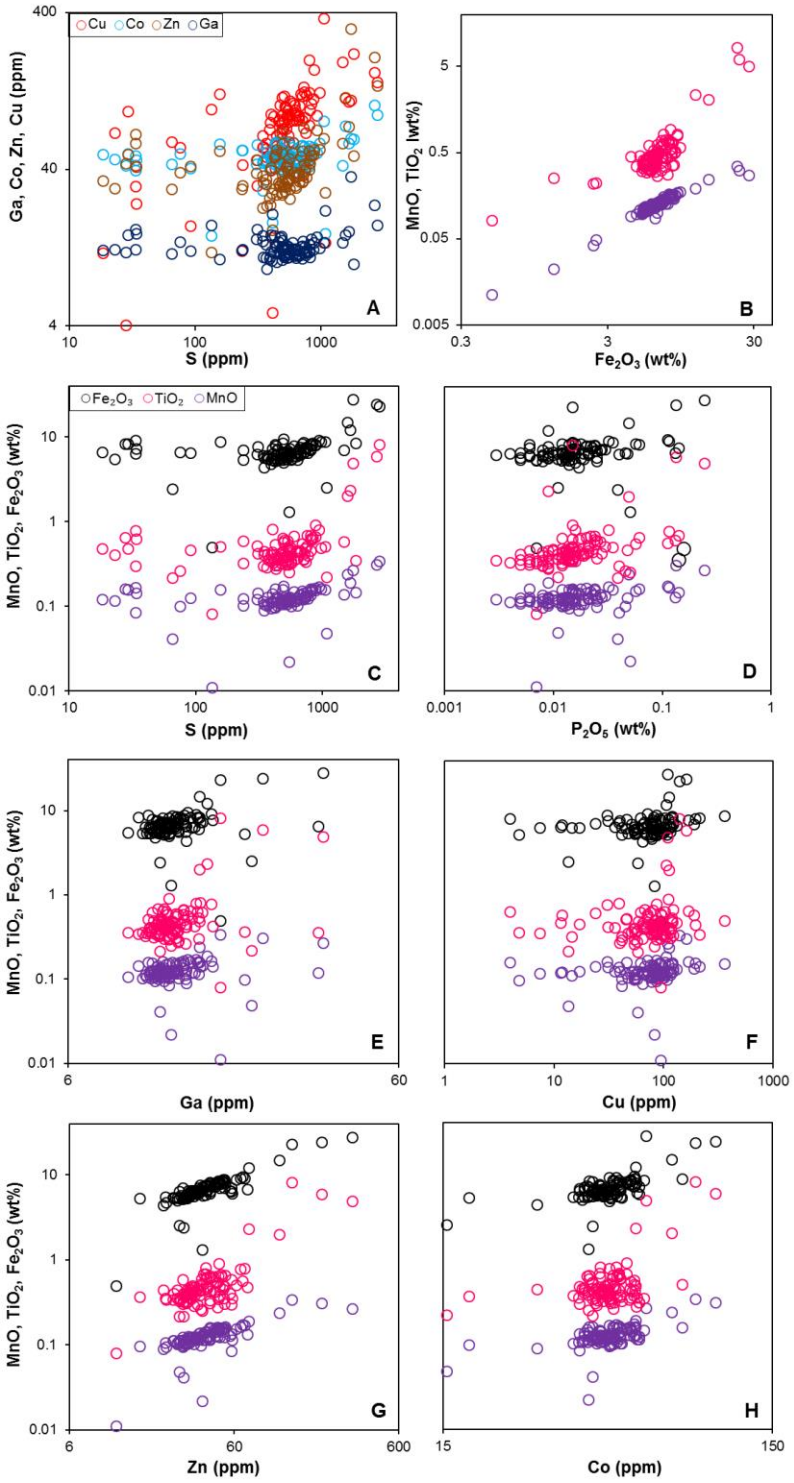

Fig. 7. A) Cu, Co, Zn and Ga versus S contents of the U1473A (Atlantis Bank, Southwest Indian Ridge) rocks. B) MnO and TiO_2 versus Fe_2O_3 contents of the U1473A rocks. C-H) MnO, TiO_2, and Fe_2O_3 versus S, P_2O_5, Ga, Cu, Zn, and Co contents of the U1473A rocks.

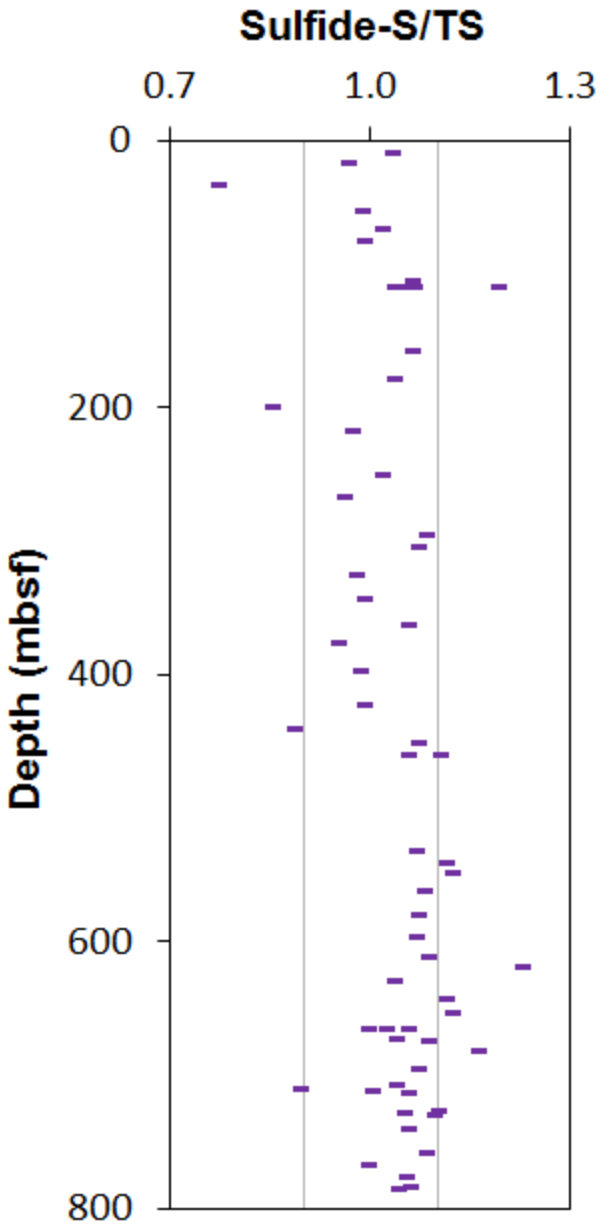

Fig. 8. IODP U1473A downhole profile of sulfide-S/TS (total sulfur). By the ratio of 1, only sulfide and no sulfate occur. Some scatter may result from powder inhomogeneity. Note that sulfate content slightly increases towards the ocean floor and the maximum sulfate content is ~24% (Sample 5R-1 121/129).

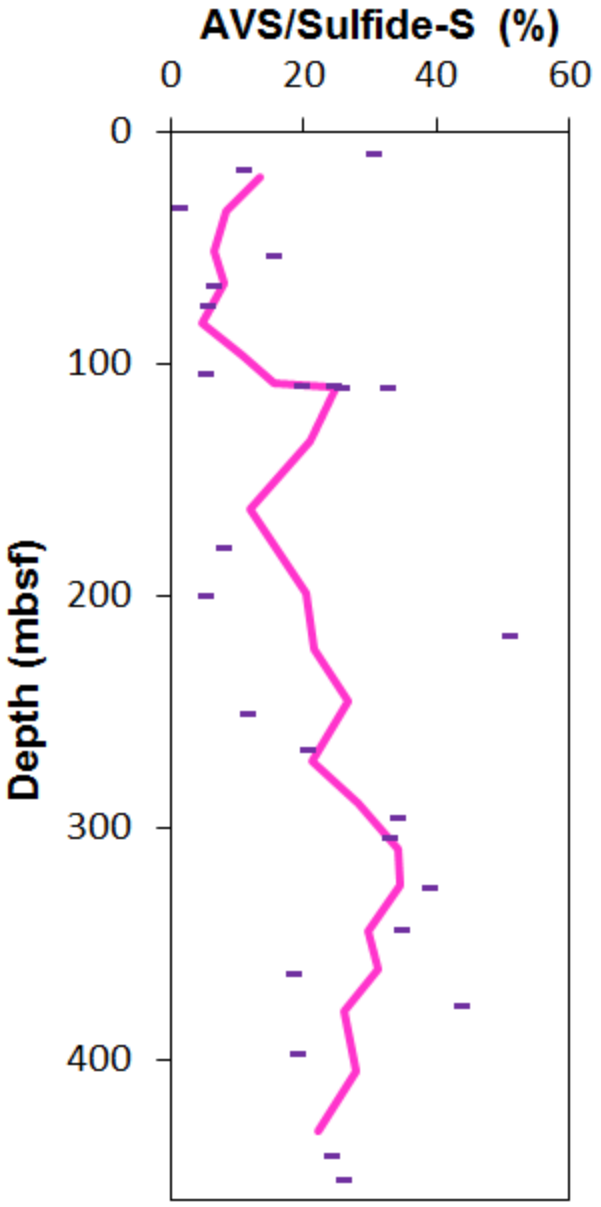

Fig. 9. Percentage of Acid Volatile Sulfides (AVS)-sulfur in the total sulfide (TS)-sulfur at the upper part of IODP Hole U1473A. The three-sample-based running average (pink line) illustrates that the AVS content grows downwards the hole, with a major boundary at ~200 mbsf, where the style of alteration changes (Figure S2 Supplementary Material).

SUPPLEMENTARY MATERIAL

Table S1. Major element contents (wt%) and Mg-numbers of the U1473A gabbros and felsic veins

Sample	Rock	Depth (mbsf)	SiO_2	TiO_2	Al_2O_3	Fe_2O_3	MnO	MgO	CaO	Na_2O	K_2O	P_2O_5	LOI	Total	Mg#
2R-1 37/46	Gabbroic	9.9	49.8	0.35	16.5	5.4	0.10	11.1	13.7	2.2	0.03	0.013	0.5	99.7	80
3R-3 120/128	Gabbroic	16.8	50.2	0.35	14.0	5.5	0.11	11.8	14.9	2.0	0.03	0.005	0.9	99.7	81
5R-1 121/129	Gabbroic	33.2	40.4	8.13	8.5	23.0	0.34	7.2	9.9	2.2	0.07	0.015	0.0	99.7	38
7R-2 33/40	Gabbroic	53.1	49.0	0.30	19.1	6.4	0.08	7.2	11.7	2.7	0.10	0.040	3.2	99.9	69
7R-2 74/80	Gabbroic	53.5	50.0	0.27	19.0	7.8	0.13	8.4	10.9	3.2	0.03	0.009	0.2	99.9	68
8R-4 140/147	Gabbroic	66.7	49.7	0.59	16.5	7.0	0.12	9.5	12.6	2.9	0.06	0.025	1.0	99.8	73
9R-3 116/123	Gabbroic	74.8	49.7	0.33	15.5	6.4	0.11	10.8	13.3	2.5	0.05	0.004	1.2	99.8	77
12R-4 48/57	Gabbroic	104.7	52.2	0.42	17.8	7.7	0.14	7.0	10.4	4.0	0.06	0.020	0.2	99.9	64
13R-1 26/33	Gabbroic	109.8	50.5	0.50	16.4	8.8	0.16	8.7	11.4	3.2	0.06	0.035	0.1	99.8	66
13R-1 40/50	Gabbroic	109.9	50.2	0.56	16.1	9.4	0.17	8.7	11.5	3.0	0.06	0.112	0.1	99.9	65
13R-1 67/75	Gabbroic	110.2	51.1	0.65	14.2	7.9	0.16	8.9	13.8	2.7	0.04	0.020	0.3	99.8	69
13R-1 75/83	Gabbroic	110.3	50.4	0.55	15.7	8.3	0.15	9.2	12.4	2.8	0.04	0.057	0.3	99.8	69
18R-1 18/25	Gabbroic	158.2	50.9	0.45	15.5	8.2	0.16	9.0	12.5	2.8	0.05	0.006	0.3	99.8	68
20R-2 17/23	Gabbroic	179.0	50.7	0.67	15.5	7.8	0.15	8.8	12.6	2.8	0.08	0.022	0.7	99.8	69
23R-2 130/134	Gabbroic	199.6	50.3	0.44	16.3	5.7	0.11	10.0	13.8	2.3	0.09	0.013	0.7	99.8	78
24R-2 39/46	Gabbroic	208.4	49.8	0.77	15.6	9.0	0.16	8.1	11.5	3.2	0.10	0.115	1.6	99.8	64
25R-1 127/133	Gabbroic	217.5	52.2	0.44	18.3	4.4	0.09	6.4	14.2	3.2	0.08	0.017	0.6	99.8	74
26R-1 81/88	Gabbroic	226.7	52.1	0.48	16.4	8.2	0.16	7.3	10.6	3.5	0.10	0.014	0.9	99.9	64
26R-2 23/28	Gabbroic	227.6	52.1	0.62	17.0	7.2	0.14	6.7	10.9	4.0	0.08	0.017	1.2	99.9	65
28R-4 111/121	Gabbroic	250.8	50.0	0.42	16.4	7.2	0.13	10.2	12.5	2.6	0.05	0.028	0.4	99.9	74
30R-2 25/35	Gabbroic	266.5	51.1	0.64	15.7	8.4	0.16	8.3	12.3	2.9	0.05	0.018	0.3	99.9	66
30R-2 44/52	Gabbroic	266.6	50.1	0.48	15.2	8.7	0.16	9.7	12.6	2.6	0.05	0.015	0.3	99.8	69
30R-3 26/33	Gabbroic	267.8	49.7	0.35	17.7	8.5	0.14	8.8	11.4	2.9	0.05	0.015	0.3	99.8	67
32R-6 134/141	Gabbroic	292.7	50.8	0.58	15.2	7.0	0.14	9.3	13.2	2.7	0.11	0.027	0.7	99.8	72
33R-2 64/72	Gabbroic	295.7	50.3	0.36	15.8	6.2	0.12	10.6	13.8	2.4	0.03	0.006	0.3	99.8	77
34R-2 12/21	Gabbroic	304.6	51.0	0.43	15.6	6.5	0.13	9.6	13.5	2.6	0.05	0.012	0.4	99.9	74
36R-3 23/30	Gabbroic	326.0	51.1	0.63	16.0	8.4	0.16	8.5	11.7	3.1	0.05	0.012	0.2	99.9	67

Sample	Rock	Depth (mbsf)	SiO_2	TiO_2	Al_2O_3	Fe_2O_3	MnO	MgO	CaO	Na_2O	K_2O	P_2O_5	LOI	Total	Mg#
38R-2 58/66	Gabbroic	343.9	51.2	0.42	18.0	6.4	0.12	8.0	12.2	3.1	0.06	0.019	0.4	99.9	71
40R-1 73/78	Gabbroic	362.4	51.8	0.52	17.4	6.2	0.12	7.8	12.5	3.2	0.06	0.021	0.2	99.9	71
41R-3 30/32	Felsic	374.6	75.9	0.08	12.5	0.5	0.01	0.5	2.3	5.4	1.31	0.007	1.4	99.9	67
41R-4 11/20	Gabbroic	375.7	50.0	0.90	14.7	8.1	0.15	10.0	13.2	2.4	0.05	0.015	0.3	99.8	71
41R-4 38/45	Gabbroic	376.0	50.5	0.68	15.2	7.0	0.14	9.7	13.9	2.4	0.04	0.024	0.2	99.8	73
41R-4 84/93	Gabbroic	376.5	51.2	0.59	16.8	5.8	0.12	8.7	13.7	2.7	0.04	0.025	0.3	99.9	75
41R-4 97/103	Gabbroic	376.6	50.6	0.39	17.2	6.5	0.12	9.0	13.2	2.7	0.04	0.016	0.1	99.8	73
43R-6 53/59	Gabbroic	397.6	50.9	0.60	16.2	6.6	0.13	9.4	12.9	2.9	0.05	0.131	0.2	99.9	74
47R-2 108/113	Gabbroic	423.1	51.9	0.80	16.5	7.3	0.14	7.6	12.1	3.4	0.05	0.016	0.2	99.8	67
49R-1 84/96	Gabbroic	440.7	50.8	0.38	17.6	6.3	0.12	8.9	12.8	2.8	0.03	0.012	0.2	99.8	74
50R-2 38/47	Gabbroic	451.5	51.1	0.35	16.7	6.2	0.12	9.3	13.2	2.7	0.03	0.003	0.2	99.9	75
51R-1 32/42	Gabbroic	459.6	50.4	0.33	17.8	7.5	0.13	9.0	11.6	2.9	0.03	0.006	0.2	99.9	70
51R-5 48/57	Gabbroic	460.7	50.5	0.31	17.2	7.1	0.12	9.8	11.6	2.9	0.08	0.012	0.3	99.9	73
51R-1 141/146	Gabbroic	465.3	46.1	0.26	19.8	6.6	0.10	4.3	14.7	3.2	0.07	0.046	4.5	99.8	57
57R-1 4/7	Gabbroic	519.2	51.6	0.64	14.2	8.2	0.16	8.6	12.1	3.0	0.20	0.061	1.0	99.8	67
59R-3 0/10	Gabbroic	531.9	51.0	0.32	17.8	5.3	0.10	8.8	13.3	2.8	0.03	0.007	0.5	99.9	77
59R-5 79/85 VEIN	Felsic	535.4	68.3	0.21	14.1	2.4	0.04	3.6	3.5	6.2	0.22	0.039	1.3	99.8	75
59R-5 79/85	Gabbroic	535.4	50.4	0.36	16.9	5.2	0.10	9.6	13.7	2.5	0.06	0.025	0.8	99.7	78
60R-2 61/69	Gabbroic	540.5	51.0	0.40	16.5	6.1	0.12	8.8	13.4	2.7	0.05	0.008	0.7	99.8	74
60R-2 106/111	Gabbroic	540.9	49.7	0.41	16.6	5.5	0.12	8.8	13.2	2.8	0.13	0.015	2.6	99.8	76
60R-5 40/48	Gabbroic	544.2	49.7	0.47	15.6	6.5	0.12	9.9	13.0	2.6	0.06	0.012	1.9	99.9	75
61R-1 21/31	Gabbroic	548.6	50.7	0.37	17.5	7.0	0.12	8.6	12.0	2.9	0.05	0.015	0.6	99.9	71
62R-4 55/61	Gabbroic	562.4	51.5	0.41	16.6	6.5	0.12	8.0	12.7	3.0	0.06	0.005	0.9	99.9	71
63R-1 75/84	Gabbroic	568.6	50.7	0.40	16.3	6.5	0.13	9.1	13.1	2.6	0.06	0.013	1.0	99.8	73
64R-3 66/76	Gabbroic	579.7	50.7	0.31	17.3	6.0	0.11	9.5	13.1	2.7	0.04	0.006	0.2	99.9	76
64R-5 45/52	Gabbroic	581.7	50.9	0.29	18.8	5.6	0.10	8.3	12.6	3.0	0.05	0.009	0.3	99.9	75
64R-6 0/9	Gabbroic	582.1	52.7	0.41	15.6	5.6	0.11	8.9	12.8	3.1	0.07	0.011	0.7	99.8	76
65R-1 99/110	Gabbroic	588.2	50.9	0.41	15.1	6.0	0.13	10.6	14.2	2.3	0.03	0.014	0.3	99.8	78
65R-7 15/26	Gabbroic	596.0	50.6	0.35	16.5	6.0	0.11	10.3	13.2	2.5	0.03	0.008	0.3	99.9	77
66R-4 2/10	Gabbroic	601.4	53.0	0.30	15.0	6.0	0.11	9.2	11.9	3.2	0.14	0.008	1.2	99.8	75

Sample	Rock	Depth (mbsf)	SiO_2	TiO_2	Al_2O_3	Fe_2O_3	MnO	MgO	CaO	Na_2O	K_2O	P_2O_5	LOI	Total	Mg#
67R-4 8/19	Gabbroic	610.8	50.5	0.31	16.2	5.7	0.11	10.8	13.0	2.5	0.03	0.005	0.7	99.8	79
68R-1 58/67	Gabbroic	616.9	51.0	0.38	16.6	5.4	0.11	9.3	14.0	2.5	0.05	0.012	0.5	99.8	77
68R-3 7/17	Gabbroic	619.2	50.2	0.32	17.0	5.7	0.11	9.9	13.8	2.4	0.03	0.009	0.4	99.8	78
69R-2 116/127	Gabbroic	628.4	50.9	0.45	16.2	6.1	0.12	9.0	14.1	2.5	0.04	0.009	0.3	99.8	75
69R-3 90/98	Gabbroic	629.5	50.7	0.46	17.6	6.3	0.12	8.7	12.9	2.8	0.04	0.013	0.2	99.8	73
70R-4 86/92	Gabbroic	640.4	49.6	0.46	15.5	6.4	0.13	9.9	13.5	2.5	0.05	0.048	1.8	99.9	75
70R-6 92/101	Gabbroic	642.9	50.3	0.48	16.2	6.8	0.12	10.2	13.3	2.3	0.04	0.015	0.2	99.8	75
72R-2 0/9	Gabbroic	649.7	50.5	0.44	15.9	5.9	0.12	10.3	14.2	2.3	0.04	0.013	0.2	99.8	78
73R-1 88/97	Gabbroic	652.8	50.6	0.47	15.2	6.7	0.13	10.0	14.3	2.3	0.03	0.010	0.2	99.8	75
74R-7 72/81	Gabbroic	662.7	50.4	0.43	15.6	7.0	0.14	9.7	13.8	2.4	0.04	0.008	0.3	99.8	73
74R-8 126/135 VEIN	Felsic	664.5	71.7	0.25	15.7	1.3	0.02	0.7	2.5	6.9	0.36	0.051	0.4	99.8	50
74R-8 126/135	Gabbroic	664.5	50.3	0.36	17.0	6.4	0.12	9.4	13.1	2.7	0.08	0.014	0.3	99.8	74
75R-1 44/52	Gabbroic	664.7	48.9	0.34	14.4	8.4	0.14	12.4	12.8	2.1	0.04	0.016	0.3	99.8	75
75R-1 83/91	Gabbroic	665.1	48.0	2.00	12.9	14.8	0.24	10.1	9.4	2.3	0.07	0.049	0.0	99.8	58
75R-2 70/79	Gabbroic	666.1	50.4	0.37	17.0	5.3	0.10	9.7	14.1	2.4	0.04	0.012	0.4	99.8	78
75R-3 0/9	Gabbroic	666.2	50.4	0.35	16.3	5.3	0.11	10.1	14.3	2.4	0.04	0.014	0.5	99.8	79
75R-8 19/29	Gabbroic	673.5	50.9	0.63	15.5	7.3	0.15	9.3	13.4	2.6	0.05	0.015	0.1	99.8	72
76R-1 13/23	Gabbroic	674.1	51.1	0.34	17.7	4.7	0.09	9.2	13.9	2.6	0.03	0.014	0.3	99.9	79
76R-3 86/93	Gabbroic	677.2	50.4	0.34	16.4	5.7	0.11	10.2	13.9	2.5	0.03	0.009	0.2	99.8	78
77R-1 100/110	Gabbroic	681.7	51.9	0.53	16.3	8.1	0.16	7.8	11.7	3.4	0.09	0.024	0.1	99.9	65
78R-5 101/110	Gabbroic	689.9	51.3	0.34	16.4	5.4	0.11	9.4	14.2	2.5	0.04	0.007	0.2	99.9	77
79R-2 55/63	Gabbroic	695.4	50.8	0.40	15.4	5.3	0.11	10.0	15.3	2.1	0.03	0.014	0.2	99.8	79
80R-2 125/133	Gabbroic	705.3	50.1	0.30	18.1	5.2	0.10	9.3	14.0	2.5	0.04	0.008	0.2	99.8	78
80R-4 127/137	Gabbroic	707.8	50.0	0.40	16.8	5.6	0.11	10.0	14.1	2.4	0.06	0.018	0.3	99.8	78
80R-7 90/100 VEIN	Felsic	711.0	56.0	0.22	22.9	2.5	0.05	1.6	9.4	5.8	0.20	0.011	1.1	99.9	56
80R-7 90/100	Gabbroic	711.0	49.3	0.51	14.0	8.7	0.16	11.8	13.0	2.1	0.05	0.015	0.1	99.8	73
80R-8 18/24	Gabbroic	711.7	38.2	4.89	12.6	27.8	0.27	4.8	8.8	2.7	0.12	0.244	0.0	100.4	26
81R-1 35/43	Gabbroic	713.2	51.3	0.45	16.7	5.0	0.11	8.6	14.8	2.5	0.07	0.016	0.3	99.8	77
81R-3 97/107	Gabbroic	716.7	40.4	5.87	8.3	24.0	0.31	8.3	10.2	1.8	0.11	0.134	0.2	99.6	41
81R-4 78/88	Gabbroic	718.0	50.4	0.68	14.6	7.5	0.14	10.1	13.7	2.3	0.06	0.141	0.2	99.7	73

Sample	Rock	Depth (mbsf)	SiO_2	TiO_2	Al_2O_3	Fe_2O_3	MnO	MgO	CaO	Na_2O	K_2O	P_2O_5	LOI	Total	Mg#
82R-5 56/66	Gabbroic	726.8	50.3	0.39	17.2	5.5	0.11	9.7	14.1	2.4	0.02	0.019	0.2	99.8	78
82R-6 43/53	Gabbroic	728.0	49.9	0.44	15.9	7.5	0.14	10.3	13.1	2.4	0.05	0.023	0.0	99.8	73
82R-6 74/84	Gabbroic	728.3	50.3	0.51	15.8	7.2	0.13	9.8	13.6	2.4	0.05	0.030	0.0	99.8	73
82R-7 14/24	Gabbroic	729.1	50.1	0.61	13.5	7.9	0.15	11.0	14.4	2.1	0.05	0.024	0.0	99.8	73
83R-9 88/98	Gabbroic	740.8	50.1	0.32	17.4	5.3	0.10	9.9	13.9	2.4	0.02	0.012	0.3	99.8	79
85R-2 101/111	Gabbroic	752.9	49.8	0.36	15.8	6.4	0.12	10.5	13.8	2.3	0.06	0.011	0.7	99.8	76
86R-2 43/53	Gabbroic	757.9	48.2	2.31	14.2	12.0	0.19	8.1	12.0	2.7	0.08	0.009	0.0	99.8	57
87R-2 0/10	Gabbroic	761.3	50.6	0.45	16.1	6.2	0.12	9.8	14.0	2.4	0.06	0.010	0.1	99.8	76
87R-5 0/10	Gabbroic	764.6	50.5	0.49	15.3	6.4	0.12	10.3	14.2	2.3	0.06	0.021	0.1	99.8	76
87R-7 32/42	Gabbroic	767.1	50.4	0.44	17.1	6.3	0.12	9.5	13.3	2.6	0.06	0.016	0.1	99.8	75
87R-7 115/125	Gabbroic	768.0	50.4	0.45	15.7	6.4	0.12	9.9	14.2	2.4	0.06	0.014	0.2	99.8	76
88R-6 85/89	Gabbroic	776.3	51.1	0.80	16.3	9.0	0.17	8.9	10.6	2.8	0.10	0.032	0.0	99.8	66
89R-4 8/19	Gabbroic	783.6	50.3	0.40	16.2	6.5	0.12	9.9	13.6	2.5	0.05	0.009	0.2	99.8	75
89R-4 88/98	Gabbroic	784.4	50.4	0.45	16.5	6.6	0.12	9.4	13.5	2.7	0.07	0.021	0.2	99.8	74

mbsf – meters below seafloor. Fe_2O_3* = Total Fe as Fe_2O_3. LOI – loss-on-ignition. Mg# = [molar Mg/(molar Mg + molar Fe)] x 100

Table S2. Trace element contents (ppm) of the U1473A gabbro and felsic veins

Sample	Depth[a]	Cu	Cd	Pb	Bi	Ga	Ge	Tl	Au	Ag	Zn	As	Sb	Se	Ni	Co	Cr	V	Mo	Sr	Zr	Y
2R-1 37/46	9.9	55	< 0.1	< 0.5	< 0.02	10.1	0.7	< 0.05	0.008	< 0.05	27	< 0.5	2.5	< 0.1	193	52	917	124	0.23	144	15	8.0
3R-3 120/128	16.8	47	0.2	< 0.5	< 0.02	9.1	1.0	< 0.05	< 0.002	< 0.05	23	< 0.5	7	< 0.1	192	51	870	166	0.12	119	12	9.4
5R-1 121/129	33.2	141	0.2	< 0.5	< 0.02	17.3	0.1	< 0.05	< 0.002	< 0.05	134	< 0.5	2.3	< 0.1	60	88	21	100	< 0.05	103	4	28.5
7R-2 33/40	53.1	42	1.4	< 0.5	< 0.02	12.1	0.1	< 0.05	< 0.002	< 0.05	58	< 0.5	2.6	< 0.1	165	39	166	118	0.28	159	14	12.9
7R-2 74/80	53.5	40	< 0.1	< 0.5	< 0.02	12.9	< 0.1	< 0.05	< 0.002	< 0.05	48	< 0.5	3.2	< 0.1	98	58	91	97	0.14	200	11	6.1
8R-4 140/147	66.7	12	1.5	< 0.5	< 0.02	12.0	0.2	< 0.05	< 0.002	< 0.05	29	2.5	3.4	< 0.1	142	52	326	135	< 0.05	156	26	15.6
9R-3 116/123	74.8	15	0.4	< 0.5	< 0.02	10.3	0.7	< 0.05	< 0.002	< 0.05	28	< 0.5	1.7	< 0.1	152	44	447	126	0.22	153	13	8.5
12R-4 48/57	104.7	31	< 0.1	< 0.5	< 0.02	16.4	0.1	< 0.05	< 0.002	< 0.05	45	< 0.5	5.9	< 0.1	42	56	14	149	0.05	211	20	10.6
13R-1 26/33	109.8	361	0.2	22.3	0.02	13.5	0.5	< 0.05	< 0.002	0.22	62	< 0.5	16.7	< 0.1	73	80	39	156	0.20	179	30	11.9
13R-1 40/50	109.9	72	0.1	1.5	< 0.02	13.8	0.6	< 0.05	< 0.002	< 0.05	67	< 0.5	1.1	< 0.1	68	57	43	138	0.16	180	45	20.4
13R-1 67/75	110.2	170	0.1	2.8	< 0.02	13.4	1.0	< 0.05	< 0.002	< 0.05	53	< 0.5	1.9	< 0.1	68	51	68	218	0.14	161	39	21.9
13R-1 75/83	110.3	119	0.1	2.7	< 0.02	12.7	0.7	< 0.05	< 0.002	< 0.05	48	< 0.5	11.2	< 0.1	73	56	76	179	0.24	163	47	13.2
18R-1 18/25	158.2	197	0.1	10.6	0.02	13.1	0.8	< 0.05	< 0.002	0.09	51	0.6	7.7	< 0.1	74	55	47	189	1.27	167	16	11.3
20R-2 17/23	179.0	81	0.1	1.0	0.02	13.4	0.2	< 0.05	< 0.002	< 0.05	50	4.4	18.7	< 0.1	79	54	82	190	0.21	168	36	20.0
23R-2 130/134	199.6	89	< 0.1	0.6	0.02	11.8	0.1	< 0.05	< 0.002	< 0.05	39	< 0.5	3.8	< 0.1	129	47	639	143	0.49	161	25	12.3
24R-2 39/46	208.4	31	0.1	1.2	< 0.02	16.3	0.4	< 0.05	< 0.002	< 0.05	66	< 0.5	0.9	< 0.1	86	48	113	158	0.12	157	42	34.5
25R-1 127/133	217.5	65	< 0.1	0.6	< 0.02	13.7	0.2	< 0.05	< 0.002	< 0.05	22	< 0.5	< 0.1	< 0.1	61	29	286	158	0.26	192	27	11.7
26R-1 81/88	226.7	92	0.1	1.4	< 0.02	15.0	0.4	< 0.05	< 0.002	< 0.05	49	1.7	4	< 0.1	30	50	< 2	153	0.07	196	24	12.1
26R-2 23/28	227.6	24	< 0.1	0.7	< 0.02	15.3	0.2	< 0.05	< 0.002	< 0.05	41	< 0.5	1.4	< 0.1	31	45	< 2	120	< 0.05	220	23	14.9
28R-4 111/121	250.8	79	< 0.1	< 0.5	< 0.02	11.6	0.7	< 0.05	< 0.002	< 0.05	46	< 0.5	1.8	< 0.1	138	57	175	141	0.14	164	35	12.3
30R-2 25/35	266.5	103	< 0.1	< 0.5	0.02	14.1	0.7	< 0.05	0.010	< 0.05	48	< 0.5	1.2	< 0.1	79	49	143	199	0.06	184	27	13.7
30R-2 44/52	266.6	121	< 0.1	< 0.5	< 0.02	12.4	0.5	< 0.05	< 0.002	< 0.05	53	< 0.5	0.4	< 0.1	120	58	158	178	0.06	162	20	11.8
30R-3 26/33	267.8	81	0.1	< 0.5	< 0.02	12.8	0.2	< 0.05	< 0.002	< 0.05	52	< 0.5	0.2	< 0.1	103	56	87	126	0.21	190	15	7.6
32R-6 134/141	292.7	191	0.1	2.4	0.03	13.4	0.5	0.09	< 0.002	< 0.05	58	< 0.5	7	0.2	115	42	187	132	0.25	147	19	20.6
33R-2 64/72	295.7	85	< 0.1	< 0.5	< 0.02	10.7	0.5	< 0.05	< 0.002	< 0.05	32	< 0.5	8.5	< 0.1	151	47	379	159	0.07	152	16	9.4
34R-2 12/21	304.6	101	< 0.1	< 0.5	< 0.02	12.3	0.6	< 0.05	< 0.002	< 0.05	38	< 0.5	2.8	< 0.1	128	45	293	165	0.3	159	17	19.7
36R-3 23/30	326.0	62	0.1	1.0	< 0.02	14.8	1.0	< 0.05	< 0.002	< 0.05	51	< 0.5	11.3	< 0.1	68	51	43	200	0.23	184	23	13.4

Sample	Depth[a]	Cu	Cd	Pb	Bi	Ga	Ge	Tl	Au	Ag	Zn	As	Sb	Se	Ni	Co	Cr	V	Mo	Sr	Zr	Y
38R-2 58/66	343.9	66	< 0.1	< 0.5	< 0.02	14.5	0.5	< 0.05	< 0.002	< 0.05	43	< 0.5	4.8	< 0.1	81	47	67	137	0.09	200	31	16.1
40R-1 73/78	362.4	45	< 0.1	0.8	< 0.02	14.2	0.9	< 0.05	0.003	< 0.05	37	< 0.5	6.1	< 0.1	52	42	33	170	0.25	201	26	12.9
41R-3 30/32*	374.6	95	< 0.1	11.3	< 0.02	17.3	0.3	0.11	< 0.002	0.09	12	< 0.5	30.6	< 0.1	5	15	< 2	4	0.50	62.8	62	54.1
41R-4 11/20	375.7	111	< 0.1	< 0.5	< 0.02	12.1	0.5	< 0.05	< 0.002	< 0.05	48	1.0	0.4	< 0.1	111	54	153	154	0.11	155	31	17.1
41R-4 38/45	376.0	122	0.1	1.6	< 0.02	11.7	0.7	< 0.05	< 0.002	< 0.05	39	< 0.5	14.8	< 0.1	109	51	188	186	0.18	152	34	15.0
41R-4 84/93	376.5	97	< 0.1	0.9	0.02	12.9	0.6	< 0.05	< 0.002	< 0.05	40	1.6	3.7	< 0.1	113	49	177	144	0.37	185	23	11.1
41R-4 97/103	376.6	80	< 0.1	< 0.5	0.05	12.6	0.5	< 0.05	< 0.002	< 0.05	32	< 0.5	1.3	< 0.1	94	44	207	155	0.22	178	29	13.1
43R-6 53/59	397.6	71	< 0.1	0.5	< 0.02	12.7	0.1	< 0.05	< 0.002	< 0.05	38	< 0.5	4	< 0.1	92	52	63	177	0.26	180	84	17.6
47R-2 108/113	423.1	39	< 0.1	< 0.5	< 0.02	15.1	0.7	< 0.05	< 0.002	< 0.05	41	< 0.5	0.6	< 0.1	54	45	38	208	0.09	183	27	12.6
49R-1 84/96	440.7	57	< 0.1	< 0.5	0.03	12.6	0.1	< 0.05	< 0.002	< 0.05	37	< 0.5	6	< 0.1	112	52	231	139	0.16	179	16	8.6
50R-2 38/47	451.5	87	< 0.1	0.5	< 0.02	12.3	0.9	< 0.05	< 0.002	< 0.05	33	< 0.5	3.3	< 0.1	102	49	160	153	0.21	179	12	8.8
51R-1 32/42	459.6	123	< 0.1	< 0.5	< 0.02	12.5	0.6	< 0.05	0.005	< 0.05	43	< 0.5	2.7	< 0.1	116	55	97	131	0.15	184	12	7.8
51R-5 48/57	460.7	64	< 0.1	0.9	< 0.02	12.7	0.1	< 0.05	< 0.002	< 0.05	53	< 0.5	2.5	< 0.1	125	59	113	115	0.16	179	13	19.2
51R-1 141/146	465.3	54	0.1	< 0.5	< 0.02	13.6	< 0.1	< 0.05	< 0.002	< 0.05	38	9.6	1.5	< 0.1	89	49	74	99	1.60	240	13	6.5
57R-1 4/7	519.2	4	< 0.1	< 0.5	< 0.02	11.6	0.3	< 0.05	< 0.002	< 0.05	43	0.6	< 0.1	< 0.1	114	42	240	139	0.06	205	56	17.9
59R-3 0/10	531.9	42	< 0.1	< 0.5	< 0.02	12.1	0.8	< 0.05	< 0.002	< 0.05	31	< 0.5	4.9	< 0.1	96	52	286	133	0.07	173	12	7.7
59R-5 79/85 VEIN*	535.4	59	< 0.1	< 0.5	< 0.02	11.4	0.4	< 0.05	< 0.002	0.12	30	< 0.5	0.2	< 0.1	173	43	642	125	0.12	156	26	14.4
59R-5 79/85	535.4	5	< 0.1	4.7	< 0.02	20.5	< 0.1	< 0.05	< 0.002	0.07	16	< 0.5	1.7	< 0.1	24	18	126	17	0.17	123	20	88.8
60R-2 61/69	540.5	88	< 0.1	< 0.5	< 0.02	12.7	0.5	< 0.05	< 0.002	< 0.05	34	1.3	0.6	< 0.1	97	48	112	169	0.15	163	18	10.9
60R-2 106/111	540.9	68	< 0.1	0.8	0.03	12.2	0.5	< 0.05	< 0.002	< 0.05	30	2.8	0.2	< 0.1	94	46	112	147	0.37	159	16	10.4
60R-5 40/48	544.2	12	< 0.1	< 0.5	< 0.02	12.0	0.5	< 0.05	< 0.002	< 0.05	33	2.3	< 0.1	< 0.1	111	49	106	164	0.08	162	19	11.1
61R-1 21/31	548.6	51	< 0.1	< 0.5	< 0.02	12.9	0.5	< 0.05	< 0.002	< 0.05	49	< 0.5	1.8	< 0.1	93	57	99	141	0.23	182	17	9.1
62R-4 55/61	562.4	36	0.1	< 0.5	< 0.02	13.7	0.4	< 0.05	< 0.002	< 0.05	33	0.6	0.5	< 0.1	72	42	50	179	< 0.05	167	13	10.2
63R-1 75/84	568.6	113	< 0.1	0.8	< 0.02	12.6	0.2	< 0.05	< 0.002	< 0.05	57	< 0.5	1.1	< 0.1	109	47	118	170	0.14	169	25	13.1
64R-3 66/76	579.7	95	< 0.1	0.6	< 0.02	12.1	0.4	< 0.05	< 0.002	< 0.05	43	< 0.5	< 0.1	< 0.1	128	50	137	146	0.06	175	11	7.9
64R-5 45/52	581.7	58	< 0.1	< 0.5	< 0.02	13.0	0.1	< 0.05	< 0.002	< 0.05	34	< 0.5	< 0.1	< 0.1	106	44	94	114	0.23	188	11	7.1
64R-6 0/9	582.1	80	< 0.1	0.9	< 0.02	13.6	0.7	< 0.05	< 0.002	< 0.05	32	< 0.5	0.4	< 0.1	116	41	156	163	0.10	145	20	28.3
65R-1 99/110	588.2	53	< 0.1	< 0.5	< 0.02	10.7	0.9	< 0.05	< 0.002	< 0.05	32	< 0.5	< 0.1	< 0.1	118	45	156	178	0.09	136	19	10.5

Sample	Depth[a]	Cu	Cd	Pb	Bi	Ga	Ge	Tl	Au	Ag	Zn	As	Sb	Se	Ni	Co	Cr	V	Mo	Sr	Zr	Y
65R-7 15/26	596.0	104	< 0.1	< 0.5	< 0.02	11.4	0.5	< 0.05	< 0.002	< 0.05	58	< 0.5	4.4	< 0.1	134	58	214	152	0.30	145	16	8.8
66R-4 2/10	601.4	55	0.1	1.0	< 0.02	14.9	0.6	< 0.05	< 0.002	< 0.05	36	< 0.5	1	< 0.1	111	44	214	133	0.10	131	15	46.1
67R-4 8/19	610.8	115	< 0.1	< 0.5	< 0.02	10.9	0.6	< 0.05	< 0.002	< 0.05	31	< 0.5	4.9	< 0.1	141	59	215	129	0.11	160	10	9.5
68R-1 58/67	616.9	82	< 0.1	< 0.5	< 0.02	11.8	0.8	< 0.05	< 0.002	< 0.05	31	< 0.5	0.5	< 0.1	125	41	272	156	0.19	168	17	16.4
68R-3 7/17	619.2	101	< 0.1	< 0.5	< 0.02	11.4	0.6	< 0.05	< 0.002	< 0.05	31	< 0.5	1.3	< 0.1	139	46	291	141	0.10	182	13	7.9
69R-2 116/127	628.4	81	< 0.1	< 0.5	< 0.02	11.9	0.7	< 0.05	< 0.002	< 0.05	36	< 0.5	< 0.1	< 0.1	108	43	254	179	0.11	170	18	10.5
69R-3 90/98	629.5	65	0.1	< 0.5	< 0.02	12.6	0.5	< 0.05	< 0.002	< 0.05	34	< 0.5	0.9	< 0.1	112	45	134	152	0.12	183	16	8.8
70R-4 86/92	640.4	17	< 0.1	< 0.5	< 0.02	11.9	0.6	< 0.05	< 0.002	< 0.05	41	0.8	0.2	< 0.1	133	40	182	169	0.28	139	46	12.0
70R-6 92/101	642.9	71	< 0.1	< 0.5	< 0.02	11.3	0.8	< 0.05	< 0.002	< 0.05	41	< 0.5	< 0.1	< 0.1	145	47	264	145	0.14	150	21	10.6
72R-2 0/9	649.7	94	< 0.1	0.6	< 0.02	11.1	0.6	0.08	< 0.002	< 0.05	31	< 0.5	< 0.1	0.2	146	50	428	129	0.26	142	20	9.3
73R-1 88/97	652.8	132	0.2	6.4	0.16	11.5	0.8	< 0.05	0.004	0.21	72	< 0.5	< 0.1	< 0.1	162	39	389	177	0.53	147	19	12.6
74R-7 72/81	662.7	87	< 0.1	< 0.5	< 0.02	11.4	0.7	< 0.05	< 0.002	< 0.05	37	0.8	< 0.1	< 0.1	129	40	332	173	0.07	161	17	11.3
74R-8 126/135 VEIN*	664.5	83	< 0.1	< 0.5	< 0.02	12.3	0.3	< 0.05	< 0.002	< 0.05	38	< 0.5	< 0.1	< 0.1	138	42	256	136	0.16	172	16	14.8
74R-8 126/135	664.5	8	< 0.1	5.7	0.08	34.3	< 0.1	0.09	< 0.002	< 0.05	< 0.5	< 0.5	0.4	< 0.1	< 0.5	< 0.1	< 2	5	0.64	69.1	110	46.7
75R-1 44/52	664.7	215	0.1	< 0.5	< 0.02	9.8	0.1	< 0.05	< 0.002	< 0.05	48	1.6	0.3	0.1	263	61	242	146	0.13	135	19	9.1
75R-1 83/91	665.1	112	< 0.1	< 0.5	< 0.02	15.0	0.1	< 0.05	< 0.002	< 0.05	113	< 0.5	4.3	< 0.1	96	74	183	155	< 0.05	135	23	17.1
75R-2 70/79	666.1	87	< 0.1	< 0.5	0.02	10.7	0.2	< 0.05	< 0.002	< 0.05	30	< 0.5	< 0.1	< 0.1	148	37	329	139	0.10	157	16	8.0
75R-3 0/9	666.2	79	< 0.1	< 0.5	< 0.02	10.4	0.3	< 0.05	< 0.002	< 0.05	28	0.9	< 0.1	< 0.1	135	39	370	138	0.18	156	17	8.5
75R-8 19/29	673.5	76	0.1	0.8	0.07	11.9	0.7	< 0.05	< 0.002	< 0.05	45	< 0.5	< 0.1	< 0.1	95	41	187	184	0.19	160	24	14.7
76R-1 13/23	674.1	78	< 0.1	< 0.5	< 0.02	11.0	0.6	< 0.05	< 0.002	< 0.05	23	< 0.5	2.4	< 0.1	119	48	248	136	0.08	180	17	7.6
76R-3 86/93	677.2	99	< 0.1	< 0.5	< 0.02	11.2	< 0.1	< 0.05	< 0.002	< 0.05	29	< 0.5	0.6	< 0.1	127	44	298	143	0.57	168	16	8.1
77R-1 100/110	681.7	46	< 0.1	0.6	< 0.02	14.9	0.7	< 0.05	< 0.002	< 0.05	47	< 0.5	0.3	< 0.1	53	43	29	169	0.10	176	37	14.4
78R-5 101/110	689.9	86	< 0.1	0.8	0.02	11.4	0.1	0.08	< 0.002	< 0.05	26	< 0.5	0.8	0.2	94	43	131	162	0.32	165	13	8.1
79R-2 55/63	695.4	71	< 0.1	< 0.5	< 0.02	10.6	0.9	< 0.05	< 0.002	< 0.05	26	< 0.5	< 0.1	< 0.1	119	40	588	167	0.20	144	19	9.7
80R-2 125/133	705.3	86	< 0.1	< 0.5	< 0.02	11.7	0.5	< 0.05	< 0.002	< 0.05	29	1.3	< 0.1	< 0.1	144	48	536	126	0.06	173	15	7.5
80R-4 127/137	707.8	55	< 0.1	< 0.5	< 0.02	10.9	0.8	< 0.05	< 0.002	< 0.05	32	< 0.5	< 0.1	< 0.1	137	45	486	137	0.11	157	17	8.5
80R-7 90/100 VEIN*	711.0	14	< 0.1	3.0	< 0.02	21.5	0.4	< 0.05	< 0.002	< 0.05	28	0.6	0.5	< 0.1	21	15	21	30	0.28	194	10	19.6
80R-7 90/100	711.0	119	0.1	< 0.5	< 0.02	10.5	0.2	< 0.05	< 0.002	< 0.05	52	1.2	0.2	< 0.1	181	57	361	168	0.18	136	18	11.2

Sample	Depth[a]	Cu	Cd	Pb	Bi	Ga	Ge	Tl	Au	Ag	Zn	As	Sb	Se	Ni	Co	Cr	V	Mo	Sr	Zr	Y
80R-8 18/24	711.7	109	0.2	0.9	< 0.02	35.4	< 0.1	< 0.05	< 0.002	< 0.05	312	1.7	< 0.1	< 0.1	83	62	170	216	0.20	146	19	51.0
81R-1 35/43	713.2	78	< 0.1	0.5	< 0.02	12.1	0.3	< 0.05	< 0.002	< 0.05	27	< 0.5	1.3	< 0.1	107	40	540	164	0.27	164	21	12.3
81R-3 97/107	716.7	163	0.2	0.8	0.02	23.3	< 0.1	0.07	< 0.002	< 0.05	205	< 0.5	0.1	< 0.1	133	101	207	334	0.11	82	9	41.2
81R-4 78/88	718.0	67	< 0.1	0.5	0.02	11.2	0.6	0.05	0.026	< 0.05	41	< 0.5	< 0.1	< 0.1	109	45	651	133	0.12	145	18	12.5
82R-5 56/66	726.8	99	< 0.1	< 0.5	< 0.02	11.1	0.6	< 0.05	< 0.002	< 0.05	30	0.5	1.2	< 0.1	163	46	662	137	0.68	169	19	9.0
82R-6 43/53	728.0	85	< 0.1	0.7	0.04	11.1	0.3	0.18	< 0.002	< 0.05	37	< 0.5	< 0.1	0.2	148	51	670	151	0.45	151	16	8.8
82R-6 74/84	728.3	84	< 0.1	< 0.5	< 0.02	11.5	0.2	< 0.05	< 0.002	< 0.05	39	< 0.5	< 0.1	< 0.1	134	48	511	156	0.41	156	23	10.5
82R-7 14/24	729.1	94	0.1	< 0.5	< 0.02	10.8	0.8	< 0.05	0.003	< 0.05	43	< 0.5	< 0.1	< 0.1	146	51	641	194	0.10	127	29	15.4
83R-9 88/98	740.8	108	< 0.1	< 0.5	< 0.02	11.3	0.3	< 0.05	< 0.002	< 0.05	30	< 0.5	0.9	< 0.1	172	48	899	136	0.17	161	17	8.2
85R-2 101/111	752.9	116	< 0.1	< 0.5	< 0.02	10.6	0.1	< 0.05	< 0.002	< 0.05	33	1.1	0.7	< 0.1	161	48	436	141	0.09	147	16	8.4
86R-2 43/53	757.9	106	< 0.1	< 0.5	< 0.02	15.8	0.1	< 0.05	< 0.002	< 0.05	74	1.7	< 0.1	< 0.1	98	58	171	106	0.06	161	7	16.7
87R-2 0/10	761.3	88	0.1	< 0.5	< 0.02	11.5	0.8	< 0.05	< 0.002	< 0.05	32	1.1	< 0.1	< 0.1	120	44	273	162	0.19	166	19	10.8
87R-5 0/10	764.6	59	< 0.1	< 0.5	< 0.02	10.9	0.8	< 0.05	< 0.002	< 0.05	34	< 0.5	< 0.1	< 0.1	115	48	321	166	0.10	156	21	10.5
87R-7 32/42	767.1	91	< 0.1	< 0.5	< 0.02	12.1	0.6	< 0.05	< 0.002	< 0.05	36	< 0.5	< 0.1	< 0.1	126	46	212	145	0.07	168	20	9.1
87R-7 115/125	768.0	100	< 0.1	< 0.5	< 0.02	11.2	0.5	< 0.05	< 0.002	< 0.05	33	< 0.5	< 0.1	< 0.1	124	44	269	169	0.06	157	20	10.4
88R-6 85/89	776.3	87	< 0.1	0.5	< 0.02	14.6	0.7	< 0.05	0.004	< 0.05	70	< 0.5	< 0.1	< 0.1	103	50	131	145	0.21	173	28	17.0
89R-4 8/19	783.6	117	< 0.1	< 0.5	< 0.02	11.8	0.2	< 0.05	< 0.002	< 0.05	35	< 0.5	< 0.1	< 0.1	150	48	296	155	0.27	169	17	10.1
89R-4 88/98	784.4	81	< 0.1	0.6	< 0.02	12.0	0.3	< 0.05	< 0.002	< 0.05	36	< 0.5	0.6	< 0.1	128	44	270	149	0.15	168	25	10.3

[a]Depth in meters below seafloor.
*felsic rock

Table S3. Sulfur geochemistry of the U1473A gabbros and felsic veins

Sample	TS ppm	Sulfide-S AVS+CRS		AVS		CRS		Measured as SO_2[a]						Measured as SF_6[b]					
								$\delta^{34}S$ [‰]			$\delta^{34}S$ [‰]			$\Delta^{33}S$ [‰]			$\Delta^{36}S$ [‰]		
		ppm	/TS	ppm	%	ppm	%	AVS	CRS	AVS+CRS	AVS	CRS	AVS+CRS	AVS	CRS	AVS+CRS	AVS	CRS	AVS+CRS
2R-1 37/46	443	453	1.02	134	30	319	70	-0.5	0.9	0.5	-0.4	0.8	0.5	-0.028	-0.029	-0.029	0.775	0.609	0.658
3R-3 120/128	374	358	0.96	36	10	322	90	0.1	0.7	0.6	-0.1	0.7	0.6	-0.012	-0.016	-0.016	0.808	2.128	1.996
5R-1 121/129	2804	2133	0.76	3	0	2130	100		0.1	0.1		0.0			-0.007			1.562	
7R-2 33/40	34																		
7R-2 74/80	432	423	0.98	61	14	362	86					0.8			-0.025			0.899	
8R-4 140/147	237	238	1.01	13	5	226	95					3.1			-0.020			1.262	
9R-3 116/123	409	401	0.98	18	5	383	95	4.3	3.8	3.8	4.8	3.9	3.9	-0.021	-0.024	-0.024	0.871	0.657	0.667
12R-4 48/57	310	326	1.05	13	4	313	96	0.7	0.2	0.2		0.0			-0.027			0.630	
13R-1 26/33	1055	1113	1.05	261	23	852	77	-0.1	1.3	1.0									
13R-1 40/50	494	585	1.18	109	19	476	81	-0.5	0.3	0.2		0.1			-0.017			0.918	
13R-1 67/75	884	907	1.03	286	31	621	69	-0.5	0.1	-0.1		0.1			-0.037			0.437	
13R-1 75/83	697	720	1.03	177	25	543	75	-0.6	0.6	0.3		0.4			-0.032			0.785	
18R-1 18/25	806	848	1.05							0.6			0.5			-0.035			0.769
20R-2 17/23	596	612	1.03	42	7	570	93	0.9	0.7	0.7	0.8	0.7	0.8	-0.013	-0.027	-0.026	0.811	0.636	0.648
23R-2 130/134	403	340	0.84	14	4	326	96	0.1	1	1.0		1.0			-0.034			0.944	
24R-2 39/46	34																		
25R-1 127/133[c]	347	334	0.96		50		50				-24.9	-25.0	-24.9	-0.034	-0.025	-0.030	0.789	0.673	0.731
26R-1 81/88	29																		
26R-2 23/28	34																		
28R-4 111/121	557	562	1.01	59	11	503	89	-0.7	-0.2	-0.3	-0.6	-0.1	-0.1	-0.022	-0.012	-0.013	0.709	2.660	2.454
30R-2 25/35	838	797	0.95	156	20	641	80				0.2			-0.029			0.875		
30R-2 44/52	975																		
30R-3 26/33	716																		
32R-6 134/141	1489																		
33R-2 64/72	539	579	1.07	192	33	387	67				-0.6	0.0	-0.2	-0.025	-0.023	-0.024	0.685	0.897	0.826
34R-2 12/21	617	656	1.06	209	32	447	68				-1.0	-0.5	-0.6	-0.019	-0.015	-0.016	0.710	0.527	0.585
36R-3 23/30	489	474	0.97	179	38	294	62	-0.3	0.2	0.0	0.1			-0.008			3.370		
38R-2 58/66	474	466	0.98	157	34	308	66	0.2	-1	-0.6									
40R-1 73/78	306	320	1.05	56	17	264	83	-0.6	0.3	0.1	-0.9	0.3	0.1	-0.022	-0.026	-0.025	0.775	0.742	0.748
41R-3 30/32*	135																		
41R-4 11/20	878																		
41R-4 38/45	809																		

Sample	TS ppm	Sulfide-S AVS+CRS		AVS		CRS		Measured as SO_2[a]						Measured as SF_6[b]					
								$\delta^{34}S$ [‰]			$\delta^{34}S$ [‰]			$\Delta^{33}S$ [‰]			$\Delta^{36}S$ [‰]		
		ppm	/TS	ppm	%	ppm	%	AVS	CRS	AVS+CRS	AVS	CRS	AVS+CRS	AVS	CRS	AVS+CRS	AVS	CRS	AVS+CRS
41R-4 84/93	534	502	0.94	215	43	288	57				-0.3	0.3	0.0	-0.027	-0.036	-0.032	0.715	0.809	0.769
41R-4 97/103	512																		
43R-6 53/59	503	491	0.98	88	18	403	82	-0.2	0.1	0.0	-0.5	0.0	-0.1	-0.027	-0.015	-0.017	0.957	1.048	1.031
47R-2 108/113	402	395	0.98									-0.3			-0.021			0.859	
49R-1 84/96	496	434	0.88	100	23	334	77	-0.7	0.2	0.0	-0.8	0.2	0.0	-0.035	-0.005	-0.012	0.911	4.481	3.658
50R-2 38/47	491	522	1.06	130	25	391	75				-0.6	0.2	0.0	-0.019	-0.035	-0.031	0.672	0.829	0.790
51R-1 32/42	736	771	1.05										0.1			-0.033			0.805
51R-5 48/57	448	490	1.09										0.1			-0.032			1.064
51R-1 141/146	76																		
57R-1 4/7	28																		
59R-3 0/10	238	252	1.06										1.5			-0.026			0.766
59R-5 79/85 VEIN*	66																		
59R-5 79/85	415																		
60R-2 61/70	543	598	1.10										0.2						
60R-2 106/112	23															-0.035			0.663
60R-5 40/48	18																		
61R-1 21/31	440	490	1.11										0.6			-0.035			1.008
62R-4 55/61	725	775	1.07										4.8			-0.022			0.643
63R-1 75/84	494												-0.1			-0.027			0.727
64R-3 66/76	543	577	1.06																
64R-5 45/52	366																		
64R-6 0/9	462																		
65R-1 99/110	369																		
65R-7 15/26	601	636	1.06										0.0			-0.023			0.787
66R-4 2/10	343																		
67R-4 8/19	514	554	1.08										-0.1			-0.027			0.753
68R-1 58/67	467																		
68R-3 7/17	476	579	1.22										0.0			-0.036			0.702
69R-2 116/127	667																		
69R-3 90/98	553	568	1.03										0.0			-0.023			0.886
70R-4 86/92	92																		
70R-6 92/101	534	591	1.11										0.2			-0.033			0.859
72R-2-W 0/9	629																		

Sample	TS ppm	Sulfide-S AVS+CRS		AVS		CRS		Measured as SO_2[a]						Measured as SF_6[b]					
								$\delta^{34}S$ [‰]			$\delta^{34}S$ [‰]			$\Delta^{33}S$ [‰]			$\Delta^{36}S$ [‰]		
		ppm	/TS	ppm	%	ppm	%	AVS	CRS	AVS+CRS	AVS	CRS	AVS+CRS	AVS	CRS	AVS+CRS	AVS	CRS	AVS+CRS
73R-1 88/97	732	814	1.11										0.0			-0.026			0.854
74R-7 72/81	670																		
74R-8 126/135 VEIN*	547																		
74R-8 126/135																			
75R-1 44/52	1830	1856	1.01							0.1			0.0			-0.026			0.624
75R-1 83/91	1572	1643	1.05							-0.1			0.1			-0.026			0.732
75R-2 70/79	634	625	0.99							-0.2			-0.1			-0.024			0.733
75R-3 0/9	494																		
75R-8 19/29	808	832	1.03							0.1			0.0			-0.036			0.720
76R-1 13/23	396	427	1.08							0			-0.1			-0.027			2.002
76R-3 86/93	515																		
77R-1 100/110	428	493	1.15							0.1			0.1			-0.026			1.856
78R-5 101/110	567																		
79R-2 55/63	393	417	1.06							0.1			0.1			-0.027			0.803
80R-2 125/133	424																		
80R-4 127/137	348	358	1.03							0.2			0.1			-0.036			1.067
80R-7 90/100 VEIN*	1079									-0.1			0.0			-0.033			0.861
80R-7 90/100	157	139	0.89																
80R-8 18/24	1733	1722	0.99							0.3			0.3			-0.041			0.857
81R-1 35/43	493	516	1.05							0			0.2			-0.032			0.817
81R-3 97/107	2680																		
81R-4 78/88	762																		
82R-5 56/66	526	575	1.09							0.1			0.0			-0.024			0.800
82R-6 43/53	671																		
82R-6 74/84	753	783	1.04							-0.1			0.1			-0.039			0.916
82R-7 14/24	824	895	1.09							0.2			0.1			-0.023			0.623
83R-9 88/98	569	596	1.05							0.1			-0.1			-0.034			0.765
85R-2 101/111	710																		
86R-2 43/53	1665	1789	1.07							0.2			0.2			-0.038			0.609
87R-2 0/10	548																		
87R-5 0/10	559																		
87R-7 32/42	620	611	0.99							-0.1			0.1			-0.025			0.753
87R-7 115/125	676																		

Sample	TS ppm	Sulfide-S AVS+CRS		AVS		CRS		Measured as SO_2[a]						Measured as SF_6[b]					
								$\delta^{34}S$ [‰]			$\delta^{34}S$ [‰]			$\Delta^{33}S$ [‰]			$\Delta^{36}S$ [‰]		
		ppm	/TS	ppm	%	ppm	%	AVS	CRS	AVS+CRS	AVS	CRS	AVS+CRS	AVS	CRS	AVS+CRS	AVS	CRS	AVS+CRS
88R-6 85/89	935	975	1.04																
89R-4 8/19	765	803	1.05							0.1			0.0			-0.041			0.630
89R-4 88/98	636	656	1.03							0.3			-0.1			-0.027			4.294

TS - total sulfur. AVS - acid volatile sulfide. CRS - chromium reducible sulfur.

[a] isotopic data represent an average of two duplicates from two different analytical sessions. [b] ThermoFinnigan Delta Plus mass spectrometer.

[c]ThermoScientific MAT 253 mass spectrometer. *felsic lithology.

Table S4. Mineral modes (%) and alteration intensities (0-5) of the U1473A rocks

Sample	Rock	Depth (mbsf)	Ol	Pl	Cpx	Opx	Ox	Sf	Amp	Qtz	Total	Alteration intensity
2R-1 37/46	gabbro	9.9	3	52	45	0	0.1	0.1	0	0	100	1
3R-3 120/128	olivine gabbro	16.8	16	42	42	1	0.0	0.4	0	0	100	2
5R-1 121/129	oxide gabbro	33.2	3	62	25	0	9.3	0.7	0	0	100	2
7R-2 33/40	olivine gabbro	53.1	10	46	43	0	1	0	0	0	100	2
7R-2 74/80	olivine gabbro	53.5	10	46	43	0	1	0	0	0	100	1
8R-4 140/147	olivine gabbro	66.7	10	50	40	0	0	0	0	0	100	1
9R-3 116/123	olivine gabbro	74.8	12	48	40	0	0	0	0	0	100	1
12R-4 48/57	olivine gabbro	104.7	5	55	40	0	0	0	0	0	100	1
13R-1 26/33	olivine gabbro/gabbro	109.8	transitional between gabbro and olivine gabbro									1
13R-1 40/50	olivine gabbro	109.9	6	52	40	0	1	0.3	0.0	0.0	100	1
13R-1 67/75	olivine gabbro/gabbro	110.2	transitional between gabbro and olivine gabbro									1
13R-1 75/83	gabbro	110.3	3	56	41	0	0	0	0	0	100	1
18R-1 18/25	olivine gabbro	158.2	8	52	40	0	0	0	0	0	100	1
20R-2 17/23	olivine gabbro	179.0	6	51	42	0	1	0	0	0	100	1
23R-2 130/134	olivine gabbro	199.6	10	55	35	0	0	0	0	0	100	2
24R-2 39/46	olivine gabbro	208.4	12	53	35	0	0	0	0	0	100	2
25R-1 127/133	olivine gabbro	217.5	12	49.5	38	0	0	0	0	0	100	3
26R-1 81/88	olivine gabbro	226.7	12	53	35	0	0	0	0	0	100	3
26R-2 23/28	olivine gabbro	227.6	8	48.8	40	0	3	0.2	0	0	100	3
28R-4 111/121	olivine gabbro	250.8	12	53	35	0	0	0	0	0	100	2
30R-2 25/35	olivine gabbro	266.5	8	48.8	40	0	3	0.2	0	0	100	1
30R-2 44/52	olivine gabbro	266.6	8	48.8	40	0	3	0.2	0	0	100	1
30R-3 26/33	olivine gabbro	267.8	5	60	35	0	0	0	0	0	100	2
32R-6 134/141[a]	olivine gabbro	292.7	12	47	42	0	0	0	0	0	101	2
33R-2 64/72	olivine gabbro	295.7	9	52	39	0	0	0	0	0	100	1
34R-2 12/21	olivine gabbro	304.6	8	60	32	0	0	0	0	0	100	2
36R-3 23/30	olivine gabbro	326.0	7	52	41	0	0	0	0	0	100	2

Sample	Rock	Depth (mbsf)	Ol	Pl	Cpx	Opx	Ox	Sf	Amp	Qtz	Total	Alteration intensity
38R-2 58/66	olivine gabbro	343.9	8	54.8	37	0	0	0.2	0	0	100	1
40R-1 73/78	olivine gabbro	362.4	10	55	35	0	0	0	0	0	100	1
41R-3 30/32	leucodiorite	374.6	0	95	0	0	0	0	5	0	100	5
41R-4 11/20	olivine gabbro	375.7	10	55	35	0	0	0.2	0	0	100	1
41R-4 38/45	olivine gabbro	376.0	10	55	35	0	0	0.2	0	0	100	1
41R-4 84/93	olivine gabbro	376.5	10	55	35	0	0	0.2	0.0	0	100	1
41R-4 97/103	olivine gabbro	376.6	10	55	35	0	0	0.2	0	0	100	1
43R-6 53/59	olivine gabbro	397.6	5	55	40	0	0	0	0	0	100	2
47R-2 108/113	olivine gabbro	423.1	7	50	42	0	1	0	0	0	100	1
49R-1 84/96	olivine gabbro	440.7	8	52	40	0	0	0	0	0	100	1
50R-2 38/47	olivine gabbro	451.5	8	52	40	0	0	0	0	0	100	1
51R-1 32/42	olivine gabbro	459.6	12	53	35	0	0	0	0	0	100	1
51R-5 48/57	olivine gabbro	460.7	12	53	35	0	0	0	0	0	100	4
51R-1 141/146	olivine gabbro	465.3	12	53	35	0	0	0	0	0	100	1
57R-1 4/7	cataclastite	519.2					n/a					4
59R-3 0/10	gabbro	531.9	3	50	47	0	0	0	0	0	100	1
59R-5 79/85 VEIN*	trondhjemite	535.4	0	70	0	0	0	0	5	25	100	4
59R-5 79/85	gabbro	535.4	2	53	45	0	0	0	0	0	100	1
60R-2 61/69	olivine gabbro	540.5	7	55	38	0	0	0	0	0	100	1
60R-2 106/111	olivine gabbro	540.9	7	55	38	0	0	0	0	0	100	4
60R-5 40/48	olivine gabbro	544.2	7	55	38	0	0	0	0	0	100	4
61R-1 21/31	olivine gabbro	548.6	6	55	38	0	1	0	0	0	100	1
62R-4 55/61	gabbro	562.4	3	55	42	0	0	0	0	0	100	1
63R-1 75/84	olivine gabbro	568.6	6	54	40	0	0	0	0	0	100	1
64R-3 66/76	olivine gabbro	579.7	7	53	40	0	0	0	0	0	100	1
64R-5 45/52	olivine gabbro	581.7	7	53	40	0	0	0	0	0	100	1
64R-6 0/9	olivine gabbro	582.1	7	53	40	0	0	0	0	0	100	1
65R-1 99/110	olivine gabbro	588.2	7	53	40	0	0	0	0	0	100	1
65R-7 15/26	olivine gabbro	596.0	8	57	35	0	0	0	0	0	100	0

Sample	Rock	Depth (mbsf)	Ol	Pl	Cpx	Opx	Ox	Sf	Amp	Qtz	Total	Alteration intensity
66R-4 2/10	gabbro	601.4	4	55	41	0	0	0	0	0	100	1
67R-4 8/19	olivine gabbro	610.8	7	53	40	0	0	0	0	0	100	1
68R-1 58/67	olivine gabbro	616.9	5	54	41	0	0	0	0	0	100	1
68R-3 7/17	olivine gabbronorite	619.2	6	60	15	14	2.5	2.5	0	0	100	1
69R-2 116/127	olivine gabbro	628.4	6	54	40	0	0	0	0	0	100	1
69R-3 90/98	gabbro	629.5	3	50	46	0	0.3	0.8	0	0	100	2
70R-4 86/92	olivine gabbro	640.4	6	54	40	0	0	0	0	0	100	4
70R-6 92/101	olivine gabbronorite	642.9	10	45	38	5	0.4	1.6	0	0	100	2
72R-2-W 0/9	olivine gabbro	649.7	7	51	42	0	0	0	0	0	100	2
73R-1 88/97	olivine gabbronorite	652.8	10	44	38	5	0.6	2.4	0	0	100	1
74R-7 72/81[b]	olivine gabbro	662.7	6	54	40	0	0	0	0	0	100	1
74R-8 126/135	olivine gabbro	664.5	7	53	40	0	0	0	0	0	100	1
74R-8 126/135 VEIN	trondhjemite	664.6	0	60	0	0	0	0	0	40	100	5
75R-1 44/52	olivine gabbro	664.7	20	35	40	0	1.0	4.0	0	0.0	100	1
75R-1 83/91	olivine gabbro	665.1	6	54	39	0	1	0.5	0	0.0	100	2
75R-2 70/79	olivine gabbro	666.1	9	53	38	0	0	0	0	0.0	100	2
75R-3 0/9	olivine gabbro	666.2	9	53	38	0	0	0	0	0.0	100	2
75R-8 19/29	oxide gabbronorite	673.5	1	43	43	5	7	1	0	0.0	100	2
76R-1 13/23	olivine gabbro	674.1	7	53	40	0	0	0	0	0.0	100	2
76R-3 86/93	olivine gabbro	677.2	6	53	41	0	0	0	0	0.0	100	2
77R-1 100/110	oxide gabbronorite	681.7	1	49	30	8	7	5	0	0.0	100	3
78R-5 101/110	olivine gabbro	689.9	6	54	40	0	0	0	0	0.0	100	2
79R-2 55/63	olivine gabbro	695.4	7	53	40	0	0	0	0	0.0	100	2
80R-2 125/133	olivine gabbro	705.3	9	51	40	0	0	0	0	0.0	100	2
80R-4 127/137	olivine gabbro	707.8	9	51	40	0	0	0	0	0.0	100	2
80R-7 90/100 VEIN	felsic vein	711.0					n/a					n/a
80R-7 90/100	olivine oxide gabbro	711.0	5	46	41.3	0	7	0.7	0	0	100	2
80R-8 18/24	olivine oxide gabbro	711.7	7	30	27	0	30	5	0	0	100	2
81R-1 35/43	olivine gabbro	713.2	7	54	39	0	0	0	0	0	100	2

Sample	Rock	Depth (mbsf)	Ol	Pl	Cpx	Opx	Ox	Sf	Amp	Qtz	Total	Alteration intensity
81R-3 97/107	olivine oxide gabbro	716.7	5	42	37	0	15.5	0.5	0	0	100	3
81R-4 78/88	olivine gabbro	718.0	7	51	42	0	0	0	0	0	100	2
82R-5 56/66	olivine gabbro	726.8	8	48	42.9	0	1	0.1	0	0	100	2
82R-6 43/53	olivine gabbro	728.0	8	48	42.9	0	1	0.1	0	0	100	1
82R-6 74/84	olivine gabbro	728.3	10	60	24	1	0.3	4.7	0	0	100	1
82R-7 14/24	olivine gabbro	729.1	5	47	30	10	4	4	0	0	100	2
83R-9 88/98	olivine gabbro	740.8	8	52	40	0	0	0	0	0	100	2
85R-2 101/111	olivine gabbro	752.9	8	52	40	0	0	0	0	0	100	2
86R-2 43/53	olivine gabbro	757.9	6	51	40	0	3	0	0	0	100	2
87R-2 0/10	olivine gabbro	761.3	8	52	40	0	0	0	0	0	100	2
87R-5 0/10	olivine gabbro	764.6	7	53	40	0	0	0	0	0	100	1
87R-7 32/42	olivine gabbro	767.1	8	52	40	0	0	0	0	0	100	2
87R-7 115/125	olivine gabbro	768.0	8	52	40	0	0	0	0	0	100	2
88R-6 85/89	olivine gabbro	776.3	6	52	41	0	1	0	0	0	100	2
89R-4 8/19	olivine gabbro	783.6	9	51	40	0	0	0	0	0	100	2
89R-4 88/98	olivine gabbro	784.4	6	52	41	0	0.8	0.2	0	0	100	2

[a]contains also ~10% of fine-grained oxide gabbro, which is not considered in the reported average modes.
[b]composed of two domains (i.e., 75% coarse gabbro, 25% fine gabbro). The reported modes reflected the weight average of the two domains.
Ol - olivine, Pl - plagioclase, Cpx - clinopyroxene, Opx - orthopyroxene, Ox - oxide, Sf - sulfide, Amph - amphibole, Qtz – Quartz
mbsf - meters below seafloor; n/a - data not available
Alteration intensity is defined as follows: 0 = fresh (<3%), 1 = slight (3%–9%), 2 = moderate (10%–29%), 3 = substantial (30%–59%), 4 = extensive (60%–89%), 5 = complete (≥90%).

Table S5. Correlation matrix of $\delta^{34}S$ and selected trace and major elements of the U1473A gabbro and felsic veins

Cu	Cd	Pb	Bi	Ga	Ge	Ag	Zn	As	Sb	Ni	Co	Cr	V	Mo	Sr	Y	TiO_2	Fe_2O_3	MnO	P_2O_5	S	$\delta^{34}S$	
1	-0.29	0.66	-0.15	-0.09	-0.01	0.67	0.27	-0.13	0.28	0.16	0.49	-0.06	0.31	0.09	-0.15	-0.09	0.22	0.28	0.32	0.03	0.56	-0.16	Cu
	1	0.42	0.32	-0.07	-0.36	1.00	-0.05	-0.01	-0.11	0.27	-0.11	0.13	-0.23	-0.02	-0.06	-0.06	-0.03	-0.07	-0.20	-0.01	-0.21	0.43	Cd
		1	0.06	0.10	0.10	0.52	-0.04	-0.54	0.54	-0.27	0.10	-0.22	-0.23	0.40	-0.22	0.16	-0.12	-0.09	-0.13	-0.12	0.10	0.55	Pb
			1	0.17	0.43	0.44	0.04	0.18	-0.33	0.46	-0.30	0.16	-0.18	0.20	-0.27	0.16	-0.14	-0.14	-0.13	-0.23	-0.08	-0.40	Bi
				1	-0.18	-0.61	0.77	0.03	0.01	-0.53	0.15	-0.38	-0.16	0.12	-0.26	0.69	0.48	0.53	0.36	0.49	0.41	-0.03	Ga
					1	0.27	-0.19	-0.34	0.05	-0.02	-0.11	0.06	0.38	0.00	-0.07	-0.06	-0.18	-0.15	-0.05	-0.11	-0.14	0.04	Ge
						1	0.83	n/a	0.18	0.51	0.65	0.05	0.60	-0.22	0.51	-0.63	0.56	0.50	0.48	0.24	0.62	-0.02	Ag
							1	0.00	-0.08	-0.09	0.58	-0.20	0.40	-0.03	-0.23	0.37	0.79	0.92	0.76	0.71	0.65	-0.06	Zn
								1	0.25	-0.14	0.21	-0.29	-0.16	0.59	0.55	-0.07	-0.03	0.01	-0.08	0.10	-0.22	-0.15	As
									1	-0.30	-0.05	-0.12	-0.11	0.10	-0.19	0.17	-0.07	-0.13	-0.14	-0.06	-0.03	0.00	Sb
										1	0.16	0.66	0.15	-0.08	-0.28	-0.39	-0.14	-0.11	-0.14	-0.11	0.05	-0.06	Ni
											1	-0.14	0.47	-0.07	-0.12	-0.11	0.61	0.72	0.75	0.28	0.59	-0.03	Co
												1	-0.05	0.00	-0.36	-0.20	-0.15	-0.22	-0.27	-0.07	-0.13	0.02	Cr
													1	-0.19	0.06	-0.26	0.26	0.41	0.48	0.28	0.27	0.04	V
														1	0.06	0.01	-0.09	-0.07	-0.12	-0.01	-0.09	0.09	Mo
															1	-0.51	-0.35	-0.22	-0.18	-0.09	-0.40	-0.06	Sr
																1	0.33	0.30	0.19	0.36	0.21	-0.12	Y
																	1	0.89	0.82	0.45	0.77	-0.05	TiO_2
																		1	0.93	0.59	0.73	-0.03	Fe_2O_3
																			1	0.44	0.71	-0.05	MnO
																				1	0.27	-0.08	P_2O_5
																					1	-0.08	S
																						1	$\delta^{34}S$

The values are correlation coefficients (R)

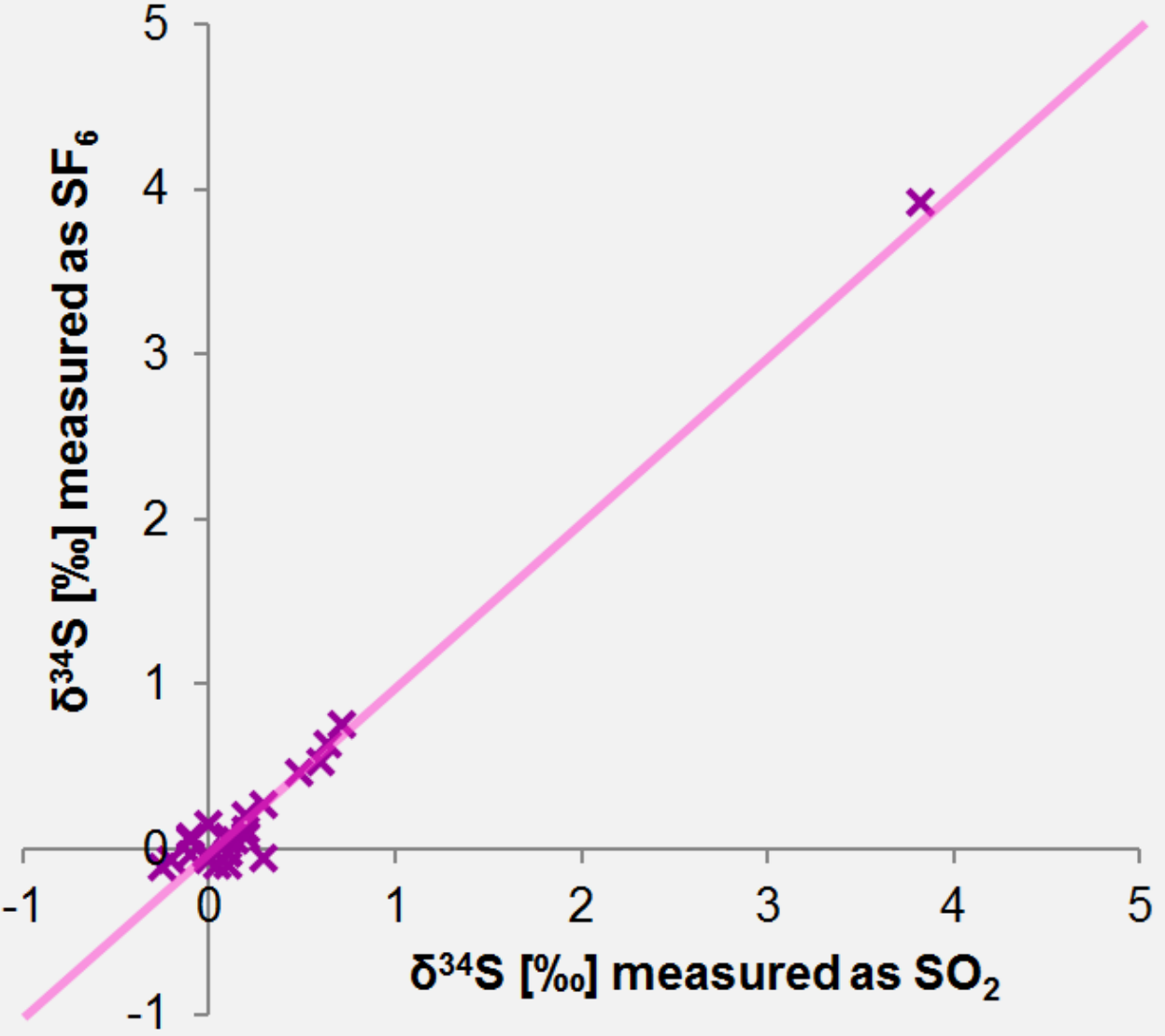

Fig. S1. Results of $\delta^{34}S$ obtained with two different analytical techniques. $\delta^{34}S$ was measure as SO_2 introduced to ThermoFinnigan Delta Plus mass spectrometer or SF_6 introduced to a ThermoFinnigan Delta Plus mass spectrometer. The obtained results are similar as demonstrated by the low scatter of our data (purple crosses) around the 1:1 line (pink).

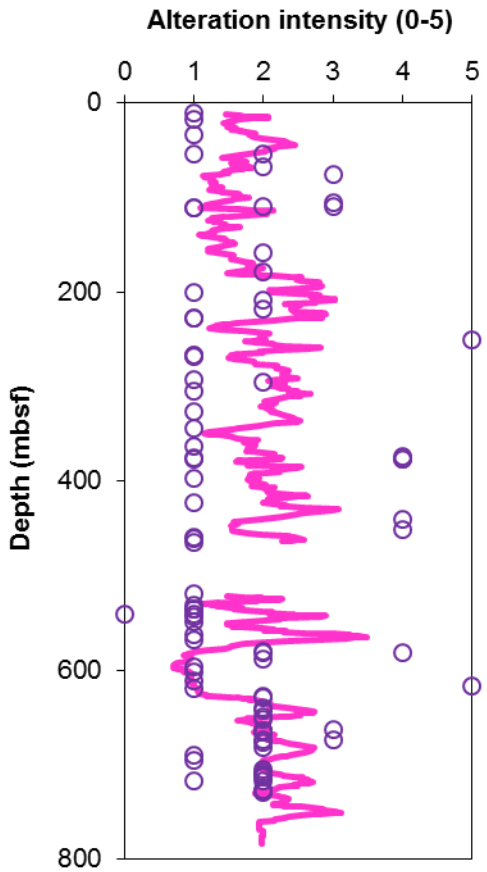

Fig. S2. Alteration intensity of our U1473A samples (purple circles) along with 11-sample running average of the entire U1473A core (pink line). Alteration intensity is defined as follows: 0 = fresh (<3%), 1 = slight (3%–9%), 2 = moderate (10%–29%), 3 = substantial (30%–59%), 4 = extensive (60%–89%), 5 = complete (≥90%). Mbsf – meters below seafloor.

Ciazela, J., Dick, H.J.B., Koepke, J., Pieterek, B., Muszynski, A., Botcharnikov, R., and Kuhn, T., 2017. Thin crust and exposed mantle control sulfide differentiation in slow-spreading ridge magmas. *Geology* 45, 935-938. https://doi.org/10.1130/G39287.1

Ciazela, J., Koepke, J., Dick, H.J.B., Botcharnikov, R., Muszynski, A., Lazarov, M., Schuth, S., Pieterek, B., and Kuhn, T. Sulfide enrichment at an oceanic crust-mantle transition zone: Kane Megamullion (23°N, MAR). *Geochimica et Cosmochimica Acta* 230*,* 155-189 https://doi.org/10.1016/j.gca.2018.03.027

SUMMARY AND CONCLUSIONS

The slow-spread oceanic crust is thinner and more heterogeneous than the fast-spread oceanic crust (**Chapter I**). In this work, we have shown the differences in lithosphere structure affect how sulfides differentiate during magmatic processes in slow-spreading ridge magmas and consequently how metals are transported between the mantle and the ocean floor. In addition, we demonstrated that the style of sulfide differentiation and metal transport depend on spreading rate and magma supply.

Where magma supply is high sulfides differentiate mostly through fractional crystallization (**Chapter II**). As we reveal in our Atlantis Bank study, sulfides typically fractionate early and therefore tend to accumulate at the lower part of gabbroic bodies. The lower parts of gabbroic bodies are by ~50% enriched in Cu with respect to the upper parts. In addition, gabbro bodies located deeper in the crust are enriched in chalcophile elements with respect to shallower gabbro bodies. Both facts are consistent with MORBs having sulfur concentrations above sulfide saturation during their ascent through the slow-spread lower crust with high magma supply.

In contrast, MORBs at slow and ultraslow spreading ridges with low magma supply can become sulfur-undersaturated due to extensive subcrustal sulfide crystallization following melt reaction with the mantle (**Chapter III**). This process may be global, but it becomes increasingly significant at ridge segments with low magma supply and thin crust, where the melt-mantle reaction can proceed to very shallow depths.

We show that the crust-mantle transition zone exposed in the Kane Megamullion OCC is highly enriched in chalcophile elements (**Chapter IV**). This enrichment is related to the crystallization of sulfides during extensive melt-mantle reaction throughout the transition zone. Our results, combined with numerous Cu deposits documented in the mantle-crust

transition zones of various ophiolites may indicate the metal enrichment, increased sulfide modes, and potentially formation of small sulfide deposits could be expected globally along the petrological Moho.

These zones of magmatic enrichment related to melt refertilization might be one of the reasons why massive sulfide deposits form mostly at the slow- and not at the fast- spreading ridges (Chapter I and IV). Lower magma budgets at ultraslow and slow spreading ridges produce more heterogeneous lower crust and thicker lithosphere with enhanced melt-mantle reaction. This usually results in enhanced concentration of metals (up to 300 ppm Cu) at high level in the lithosphere where they can be mined by hydrothermal fluids (Chapters II and IV). In contrast, where magma budget is high and the crust is fully developed, sulfides are mostly controlled by fractional crystallization. This results in zones of enrichment with lower degree of metal concentrations (up to ~130 ppm Cu), and emplaced at the bottom of gabbroic bodies where hydrothermal fluids have only limited access (Chapter II).

CURRICULUM VITAE

JAKUB CIĄŻELA

Institut für Mineralogie
Leibniz Universität Hannover
Callinstr. 3, 30167 Hannover
j.ciazela@mineralogie.uni-hannover.de
Tel.: +49 511 762 2322
Fax: +49 511 762 3045

HIGHER EDUCATION

IV 2015- II 2018 Leibniz Universität Hannover - **Ph.D. program** in Earth science
Thesis: *Sulfide differentiation in slow-spreading ridge magmas.*
advisors: prof. Jürgen Koepke, prof. Andrzej Muszyński, dr Thomas Kuhn

2015 Adam Mickiewicz University, Poznań – **M.Sc.** in Geology (**individual study program** accepted in 25.09.12 by act nr 226-2011/2012 of Council of Faculty of Geographical and Geological Sciences; grade 4.9/5.0, "very good")
Thesis: *Mantle rock exposures at oceanic core complexes along mid-ocean ridges*.
advisors: prof. Andrzej Muszyński

2014 Leibniz Universität Hannover – **M.Sc.** in Mineralogy (grade 1.1, "very good")
Thesis: *Mantle-crust differentiation of chalcophile elements: an insight from an oceanic core complex.*
advisors: prof. Jürgen Koepke, dr Thomas Kuhn

2012 Adam Mickiewicz University, Poznań – **B.Sc.** in Geology (**individual study program**; grade 4.9/5.0, "very good")
Thesis: *Effect of water activity on the eutectic point in natural granitic system*.
advisors: prof. Andrzej Muszyński, prof Francois Holtz

2010 Adam Mickiewicz University, Poznań – **M.Sc.** in Tourism and recreation (grade 4.2/5.0; "good")
Thesis: *Hitchhiking as a social phenomenon – factors of functioning*.
advisors: prof. Waldemar Ratajczak

AWARDS & SCHOLARSHIPS

2017 IP@Leibniz scholarship for a research stay abroad
2016 European Association of Geochemistry (EAG) Early Science Career Ambassador award
2016 Travel grant of Graduierten Akademie to attend AGU Fall Meeting in San Francisco
2016 Travel grant of Graduierten Akademie to attend Goldschmidt Conference in Yokohama
2016 IP@Leibniz scholarship for a research stay abroad
2016 DAAD Research Assistantship at the Leibniz University Hannover
2015 ECORD Scholarship

2015 MagellanPlus travel grant to attend IODP workshop Indian Ocean Crust & Mantle Drilling at Woods Hole Oceanographic Institution, Woods Hole, MA, USA
2015 the EGU Young Scientist's Travel Award
2014 Lower Saxony Scholarship
2014 The Kulczyk Family Fund Scholarship
2014 Studencki Nobel Award for the second-best student in Poland
2014 Dean's graduation award for the best graduating student of the Faculty of Geographical and Geological Sciences, Adam Mickiewicz University
2014 Studencki Nobel Award for the best student of the Wielkopolska region
2014 Award for the best student of the Adam Mickiewicz University
2013 The Marshal's Scholarship of the Wielkopolska Voivodeship
2013 PGNiG Foundation Scholarship
2013 The Diamentowy Grant award of Ministry of Science and Higher Education of Poland
2013 Studencki Nobel Award for the best student of natural science in the Wielkopolska region
2013 Award for the best student of the Adam Mickiewicz University
2012 PGNiG Foundation Scholarship
2012 The Kulczyk Family Fund Scholarship

GRANTS

Principal Investigator

2017-2020 *Migration of chalcophile metals through the lower oceanic crust: Insights from IODP Site 1473*
Funding: National Science Center Poland, program PRELUDIUM 12, grant no. 2016/23/N/ST10/00288

2017-2018 *Sulfide-rich interval discovered deep in the lower crust (U1473A, Atlantis Bank, SWIR)*
Funding: ECORD Research Grant

2017-2018 *A profile of multiple sulfur, oxygen, and strontium isotopes and related chalcophile elements through the lower slow-spreading crust (IODP Expedition 360, Atlantis Bank, Southwest Indian Ridge)**
Funding: Deutsche Forschungsgemeinschaft (DFG), grant no. KO 1723/23-1
*Formal PIs are Juergen Koepke & Harald Strauss

2016-2017 *Sulfur and chalcophile element profile in the slow-spreading lower oceanic crust: Hole 1473A, Atlantis Bank*
Funding: The Graduate Academy of Leibniz Universität Hannover, grant no. 60421784

2013-2017 *Circulation of copper and other chalcophile elements within SubMoho Mantle and oceanic crust*
Funding: Ministry of Science and Higher Education, grant no. DI2012 2057 42

Research assistant

2011 *Granites of a tectonic suture zone from Baga Gazriin Chuluu pluton in Central Mongolia – petrology and geochemistry.*
Funding: Ministry of Science and Higher Education, grant no. N N307 225835

2011 *Concentration of metals according to granulometric fractions in flood sediments from winter 2010/2011 in Warta valley around Poznań*
Funding: Ministry of Science and Higher Education, grant no. N N304 105240

2009-2010 *Social and economic aspects of operations of indoor swimming pool in Poznań*
Status: Co-Investigator
Funding: Poznań City Council

2009-2010 *Transport in Poznań.*
Funding: Poznań City Council

2009-2010 *Diagnosis for Tourism and Recreation sector in Poznań Agglomeration.*
Funding: Centrum Badań Metropolitalnych, AMU

2009 *Modern methods of measuring an impact of infrastructural and fleet investment on transport*
Funding: Ministry of Regional Development, Poland

INVITED TALKS

2017 *Sulfide differentiation in slow-spreading ridge magmas*. Second Institute of Oceanography, State Oceanic Administration, Hangzhou, China, 16.11.2017.

2017 *Sulfide differentiation in slow-spreading ridge magmas*. China University of Geosciences, Wuhan, China, 15.11.2017.

2014 *Three spectacular processes controlling the ocean floor ore deposits*. DAAD Stipendiatentreffen, Braunschweig, Germany, 11-13.07.2014.

2012 *Effect of water activity on the eutectic point in natural granitic system*. Bayerische Geoinstitut, University of Bayreuth, Germany, 25.06.2012.

SEA-GOING EXPERIENCE

Shipboard scientist, D/V JOIDES Resolution, IODP Expedition 360: *Southwest Indian Ridge Lower Crust and Moho*, 30.11.2015 - 30.01.2016.

RESEARCH STAYS ABROAD

2017 1-month research stay at Institute of Geology and Paleontology at the University of Münster

2015 DAAD scholarship for short-term research stays at the Leibniz University Hannover

2014 German Academic Exchange Service (DAAD) Study Scholarship - extension

2014 DAAD scholarship for short-term research stays at the Leibniz University Hannover

2013 1-mont research stay at Woods Hole Oceanographic Institution, Massachusetts, USA

2013 DAAD Scholarship for a MSc program in Germany

2013 DAAD scholarship for short-term research stays at the Leibniz University Hannover

2012 Erasmus Training Scholarship at the Institute of Mineralogy, LUH

2012 DAAD scholarship for short-term research stays at the Leibniz University Hannover (x3)

2011 DAAD scholarship for short-term research stays at the Leibniz University Hannover

2007 Socrates - Erasmus student exchange program, Università degli Studi di Macerata, Italy, field of study: Tourism and Recreation

UNIVERSITY SERVICE

Working group to establish the University Park of History of the Earth at the Adam Mickiewicz University (2011-2012)

Geology Student Scientific Chapter of Adam Mickiewicz University (2009-2011), one year as a chairman of the Chapter (2011)
Geography Student Scientific Chapter of Adam Mickiewicz University (2005-2010), three years as a head of Tourism and Recreation Group (2006/2007, 2008-2010)

LANGUAGES

Polish (native),
English (full professional proficiency),
German (fluent),
Italian (fluent)

LIST OF PUBLICATIONS

JOURNALS

11. **Ciazela, J.,** Koepke, J., Dick, H.J.B., Botcharnikov, R., Muszynski, A., Lazarov, M., Schuth, S., Pieterek, B., and Kuhn, T. Sulfide enrichment at an oceanic crust-mantle transition zone: Kane Megamullion (23°N, MAR). *Geochimica et Cosmochimica Acta* 230, 155-189 https://doi.org/10.1016/j.gca.2018.03.027

10. **Ciazela, J.,** Siepak, M., and Wojtowicz, P., 2018. Tracking heavy metal contamination in a complex river-oxbow lake system: Middle Odra Valley, Germany/Poland. *Science of the Total Environment* 616-617, 996-1006. https://doi.org/10.1016/j.scitotenv.2017.10.219

9. **Ciazela, J**., Dick, H.J.B., Koepke, J., Pieterek, B., Muszynski, A., Botcharnikov, R., and Kuhn, T., 2017. Thin crust and exposed mantle control sulfide differentiation in slow-spreading ridge magmas. *Geology* 45, 935-938. https://doi.org/10.1130/G39287.1

8. MacLeod, C.J., Dick, H.J.B., Blum, P., and the Expedition 360 Scientists (incl. **Ciazela, J.**), 2017. *SW Indian Ridge lower crust and Moho.* Proceedings of the International Ocean Discovery Program, 360: College Station, TX (International Ocean Discovery Program). http://dx.doi.org/10.14379/iodp.360.2017.

7. **Ciążela, J.**, Dick, H.J.B., MacLeod, C.J., Blum, P., and the Expedition 360 Scientists, 2016. IODP Expedition 360: first stage of drilling into Earth's Mantle. *Przegląd Geologiczny* 64(11), 889-895.

6. **Ciazela, J.**, and Siepak, M, 2016. Environmental factors affecting soil metals near outlet roads in Poznań, Poland: Impact of grain size, soil depth and wind dispersal. *Environmental monitoring and assessment* 188(6), 1-12.

5. Dick, H.J.B., MacLeod, C.J., Blum, P., and the Expedition 360 Scientists (incl. **Ciazela, J.**), 2016. *Expedition 360 Preliminary Report*: *Southwest Indian Ridge lower crust and Moho*. International Ocean Discovery Program. http://dx.doi.org/10.14379/iodp.pr.360.2016.

4. **Ciazela, J.,** Koepke, J., Dick, H.J.B., and Muszyński, A., 2015. Mantle rock exposures at oceanic core complexes along mid-ocean ridges. *Geologos* 21(4), 207-231.

3. Dunkel, K.G., **Ciazela, J**., Thompson, J.O., Escario Perez, S., and Seyedali, M., 2015. Ocean crust processes: magma, faults, fluxes and life. 31 August – 11 September 2015, Bremen, Germany. *ECORD Newsletter* 25, 13.

2. Machowiak, K., Holtz, F., Stawikowski, W., and **Ciazela, J.**, 2013. Role of water on fractionation processes and trace element distribution in A-type granites: the example of the Baga Gazriin Chuluu granites (Central Mongolia). *Neues Jahrbuch für Mineralogie - Abhandlungen* 190, 197-219.

1. **Ciazela, J**., Siepak, M., and Wójtowicz, P., 2012. Czynniki wpływające na zawartość metali ciężkich w gruntach przy drogach wylotowych z Poznania. In R. Chęciński (Ed.),

Różnorodność. Zeszyt Kół Naukowych Uniwersytetu im. Adama Mickiewicza (pp. 38-48). Poznań: Rada Kół Naukowych UAM.

CONFERENCE ABSTRACTS

2017

29. **Ciążela, J.**, Koepke, J., Strauss, H, Pieterek, B.*, Muszyński, A., Dick, H.J.B., Kuhn, T., and Bender, M.*, 2017. Sulfur isotopes record chalcophile metal transport through the lower oceanic crust: IODP Hole U1473A, Atlantis Bank, Southwest Indian Ridge. 24th Session of the Petrology Group of the Mineralogical Society of Poland, October 19-22, 2017 **[oral presentation]**
28. Pieterek, B.*, **Ciążela, J.**, Koepke, J., Strauss, H., Dick, H.J.B., Duczmal-Czernikiewicz, A., Bedner, M.*, and Muszyński, A., 2017. Layer boundaries attract sulfides throughout the igneous layering of the lower oceanic crust: IODP Hole U1473A, Atlantis Bank, Southwest Indian Ridge. 24th Session of the Petrology Group of the Mineralogical Society of Poland, October 19-22, 2017 [poster]
27. Pieterek, B.*, **Ciążela, J.**, Szczepanik, M., Duczmal-Czernikiewicz, A., and Muszyński. A., 2017. Sulfides help to understand the formation of igneous layering at the lower oceanic crust: IODP Hole U1473A, Atlantis Bank, Southwest Indian Ridge. 4th Session of Students Geological Chapters 2017, October 12-14, 2017 [oral presentation].
26. **Ciążela. J.**, Koepke, J., Dick, H.J.B., Botcharnikov. R., Pieterek. B.*, Muszyński, A., and Kuhn, T., 2017. Shallow mantle controls sulfide differentiation in slow-spreading ridge magmas. GeoBremen 2017 "The System Earth and its Materials – from Seafloor to Summit", September 24-29, 2017 **[poster]**
25. Pieterek, B.*, **Ciążela, J.**, Koepke, J., Dick, H.J.B., Duczmal-Czernikiewicz, A., Bender, M.*, Muszyński, A., and Szczepanik, M., 2017. Distribution of sulfides across igneous layering at the slow-spread lower oceanic crust: Atlantis Bank, Southwest Indian Ridge. 10th Geosymposium of Young Researchers „Silesia 2017", Zabrze, September 21-23, 2017 [poster]
24. **Ciazela, J.,** Koepke, J., Strauss, H., Bender, M.*, Pieterek, B.*, Kuhn, T., Dick, H.J.B., and , A., 2016. Igneous Sulfides in Gabbros of the Lower Oceanic Crust: IODP Hole U1473A, Atlantis Bank, Southwest Indian Ridge. Goldschmidt conference, Paris, August 13-18, 2017 **[oral presentation**]
23. **Ciazela, J.,** Koepke, J., Strauss, H., Pieterek, B.*, Bender, M.*, Dick, H.J.B., Kuhn, T., and Muszynski, A., 2017. Sulfide-rich interval in gabbros of the IODP drill core from site U1473 (Atlantis Bank, Southwest Indian Ridge, SWIR). Gemeinsames Kolloquium der Schwerpunktprogramme IODP/ICDP, Braunschweig, Germany, March 14-16, 2017. *Conference proceedings*, p. 47. **[poster]**
22. Bender, M.*, **Ciazela, J.,** Koepke, J., Dick, H.J.B., Strauss, H., Pieterek, B.*, Muszynski, A., and Kuhn, T., 2017. Sulfide-rich gabbro within the footwall of an oceanic core complex: looking into the source of seafloor massive sulfides. 2nd GOOD Meeting. Postgraduate conference on the „Geology of Ore Deposits", Hannover, Germany, March 8-11, 2017. *Conference proceedings*, p. 13. [poster]

*student

2016

21. **Ciazela, J.**, Koepke, J., Dick, H., Botcharnikov, R., Kuhn, T., and Muszynski, A., 2016. Anomalous differentiation pattern of chalcophile metals in the Kane Megamullion MORBs. AGU Fall meeting, San Francisco, December 12-16, 2016**. [poster]**
20. **Ciazela, J.**, Koepke, J., Dick, H.J.B., Muszynski, A., Botcharnikov, R., Kuhn, T., and Albrecht, M., 2016. Cu-rich serpentine at a crust-mantle transition zone – remnants of primary sulfide accumulation? Goldschmidt conference, Yokohama, June 26 – July 1, 2016 **[oral presentation]**
19. **Ciazela, J.,** Koepke, J., Dick, H.J.B., MacLeod, C.J., Blum, P., and Expedition 360 Scientists, 2016. Cruise report: IODP expedition 360: Southwest Indian Ridge Lower Crust and Moho. Gemeinsames Kolloquium der Schwerpunktprogramme IODP/ICDP, Heidelberg, Germany, March 14-16, 2016. *Conference proceedings*, p. 24-25. **[oral presentation]**

2015

18. Dick, H.J.B, Koepke, J., and **Ciazela, J.**, 2015. Seafloor Massive Sulfides - looking into the source: the Dike-Gabbro Transition at Slow and Ultraslow Spreading Ridges. SMS Workshop, Hangzhou, China, September 27-28, 2015 [oral presentation]
17. Schuth, S., Horn, I., **Ciazela, J.**, and Weyer, S., 2015. Significant vanadium isotope fractionation revealed in V minerals by femtosecond laser ablation-MS. Goldschmidt conference, Prague, August 16-21, 2015. [oral presentation]
16. **Ciazela, J.,** Koepke, J., Botcharnikov, R., Dick, H., Kuhn, T., and Muszynski, A. (2015). Why Primary Copper Enrichment Could Be Expected at the Moho Transition Zone? IODP workshop Indian ocean crust & mantle drilling, Woods Hole, MA, USA, May 13-16, 2015. *Workshop report*, p. 31-32. **[oral presentation]**
15. **Ciazela, J.,** Dick, H., Koepke, J., Botcharnikov, R., Kuhn, T., and Muszynski, A. (2015). Cu refertilization of harzburgites by melt percolation. EGU General Assembly, Vienna, April 12-17, 2015, *Geophysical Research Abstracts* 17, EGU2015-1044. **[oral presentation]**
14. Kubiak, M., Mege, D., Gurgurewicz, J., and **Ciazela, J.** (2015). Thermal mapping of mountain slopes on Mars by application of a Differential Apparent Thermal Inertia technique. EGU General Assembly, Vienna, April 12-17, 2015, *Geophysical Research Abstracts* 17, 1030. [oral presentation]
13. **Ciazela, J.**, Dick, H., Koepke, J., Kuhn, T., Muszynski, A., and Kubiak., M., 2014. Mantle-crust differentiation of chalcophile elements in the oceanic lithosphere. AGU Fall meeting, San Francisco, December 15-19, 2014, V31B-4756. **[poster]**

2014

12. Kubiak, M., Mege, D., Gurgurewicz, J., and **Ciazela, J.,** 2014. New method for high-resolution apparent thermal inertia mapping of Mars and application to Valles Marineris. AGU Fall meeting, San Francisco, December 15-19, 2014, P33A-4020. [poster]
11. **Ciazela, J.**, Dick, H., Koepke, J., Muszynski, A., and Kuhn, T., 2014. Mantle-crust differentiation of chalcophile elements in the oceanic lithosphere. Annual Meeting DMG. Mineral at the focal point, Jena, September 21-24, 2014, *Abstract book*, p. 160-161.
10. Kubiak, M., Mege, D., Gurgurewicz, J., and **Ciazela, J.**, and Debniak, K., 2014. High-Resolution Apparent Thermal Inertia Mapping of Valles Marineris (Mars). The eighth

international conference on Mars, Pasadena, California, July 14-18, 2014, abstract 1387. [poster]

9. **Ciazela, J.**, Dick, H., Koepke, J., Holtz, F., Kuhn, T., and Muszynski, A., 2014. Three spectacular processes controlling the ocean floor ore deposits. DAAD Stipendiatentreffen, Braunschweig, July 11-13, 2014. **[oral presentation]**
8. **Ciazela, J.,** Dick, H., Kuhn, T., Koepke, J., and Muszynski, A. (2014). The first budget of copper in an oceanic core complex. DMG Sektionstreffen Petrologie, Petrophysik & Geochemie, Hannover, June 27-28, 2014. **[oral presentation]**
7. Kubiak, M., Mege, D., Gurgurewicz, J., **Ciążela, J.,** and Dębniak, K. (2014). Thermal data processing for high-resolution mapping of Valles Marineris, Mars. Mars - connecting planetary scientists in Europe, Warsaw, June 3-5, 2014, p. 50. [poster]

2013

6. **Ciążela, J.,** Muszyński, A., Koepke, J., Dick, H., and Holtz, F. (2013). Cyrkulacja miedzi i innych pierwiastków chalkofilnych w płaszczu sub-Moho i w skorupie oceanicznej. Geologia morza – teraźniejszość kluczem do przeszłości, przeszłość kluczem do przyszłości, Poznań, November 7-9, 2013, *Geologia morza*, p. 23-24. **[oral presentation]**
5. **Ciazela, J.** and Holtz, F. (2013). Empirical equation on minimum water content of a rhyolithic melt as a function of temperature and pressure. Joint Annual Meeting DMG and GV / Sediment. Geofluids: Lubricants of the Dynamic Earth, Tübingen, September 16-20, 2013, *Abstract book*, p. 61. **[oral presentation]**

2012

4. **Ciążela, J.** (2012). Experimental petrology: a new insight into the deep Earth composition. 19th meeting of the Petrology Group of the Mineralogical Society of Poland, Obrzycko, October 19-21, 2012, *Mineralogia special papers* 40, 69. [oral presentation]
3. **Ciążela, J.**, Bolte, T., Holtz, F., Muszyński, A., and Machowiak, K. (2012). Effect of water activity on the eutectic point in the natural granitic system. 2nd International Conference on "Contemporary problems of geochemistry", Kielce, September 24-26, 2012, *Mineralogia special papers* 39, 28-29. **[oral presentation]**
2. Siepak, M., **Ciążela, J.,** Grabowska, E., Kobyłecka, P., Krzyżak, E., Prokopyk, M., Rychły, J., Wójtowicz, P., Zakrzewski, P., and Zimny, D. (2012). Variability in concentrations of metals in soils near outlet roads in Poznań (Poland). 3rd AAPG/SEG/EAGE International Geosciences Student Conference, Belgrade, May 29-31, 2012. *Proceedings*, p. 200-203. [oral presentation]
1. **Ciążela, J**., Siepak, M., Grabowska, E., Kobyłecka, P., Krzyżak, E., Prokopyk, M., Rychły, J., Wójtowicz, P., Zakrzewski, P., and Zimny, D. (2012). Czynniki wpływające na zawartość metali ciężkich w gruntach przy drogach wylotowych z Poznania. III Kongres Kół Naukowych UAM, Poznań, May 7-8, 2012. **[oral presentation]**